



Alma Mater Studiorum – University of Bologna

PhD IN

BIOENGINEERING

XXV Cycle

THESIS TITLE

Lesion detection and classification in breast cancer:
evaluation of approaches based on morphological features,
tracer kinetic modelling and semi-quantitative parameters in
MR functional imaging (DCE-MRI)

Presented by: Roberta Fusco

PhD Coordinator

Ch.mo Prof. Angelo Cappello

Supervisor

Professor Mario Cesarelli

Examiners

Professor Mauro Ursino

Doctor Paola Scifo

Co-Supervisor

Professor Mario Sansone

Doctor Antonella Petrillo

*I dedicate this thesis to
my family, my boyfriend, Antonella, Mario and my friends
for their constant support and unconditional love.
I love you all dearly.*

Contents

1	An Introduction to Dynamic Contrast-Enhanced MRI in Oncology	5
1.1	Pathophysiological Basis of Contrast Enhancement	7
1.2	Breast cancer imaging	10
1.3	Patient Examination	11
1.4	Dynamic MR Acquisition Techniques	13
1.4.1	Breast DCE-MR Acquisition	14
1.5	Analysis of Dynamic Data	14
1.5.1	Visual Inspection	15
1.5.2	Enhancement Curve Analysis: model free and model based	16
1.5.3	Semi-quantitative analysis	17
1.6	Rationale	19
2	Introduction to kinetic modeling	21
2.1	Introduction	21
2.2	General framework for pharmacokinetics modelling	22
2.3	Influence of the arterial input function	25
2.4	Tissue CA Concentration for principal kinetic models and corresponding AIF	26
2.4.1	Tofts model	26
2.4.2	Brix model	27
2.4.3	Tissue homogeneity model	27
2.4.4	Adiabatic approximation to the tissue homogeneity (ATH) model	29
2.5	Estimation of Tracer Concentration	30
3	Distributed versus Compartmental Tracer Kinetic Models	33
3.1	Introduction	33
3.2	A Comparison between ATH models and Compartmental Models	35
3.2.1	Image and data Analysis	36
3.2.2	Methods: Goodness-of-fit metrics used to compare kinetic models	37
3.2.3	Methods: Reliability of Fit kinetic parameters	38
3.2.4	Results	38

3.3	Discussion	44
4	Influence of parametrization on tracer kinetic modelling	47
4.1	Introduction	47
4.2	Parameterisations of Toft' model	50
4.3	Model Curvature	50
4.4	Comparison of the two commonly used parameterisations on the Tofts' model curvature	51
4.4.1	Simulations setup	51
4.4.2	Results	52
4.5	Discussion	56
5	Quantitative Approaches for simultaneous pixel classification and tracer kinetic modelling	59
5.1	Introduction	59
5.2	Expectation Maximisation framework	61
5.3	Cramer-Rao Lower Bounds as errors measurement	64
5.4	Simulation Setup	65
5.4.1	General characteristics of the simulated data	65
5.4.2	Assessment of SNR improvement	65
5.4.3	Sensitivity to initial estimates	66
5.4.4	Tumour heterogeneity and alternative descriptive measures	66
5.5	Real data acquisition	67
5.6	Results	67
5.6.1	Assessment of SNR improvement	67
5.6.2	Sensitivity to initial estimates	68
5.6.3	Tumour heterogeneity and alternative approaches	68
5.6.4	Preliminary results on real data	68
5.7	Discussion	71
6	Segmentation and classification using machine learning approach	77
6.1	Introduction	78
6.2	Methods	79
6.2.1	ROI segmentation	79
6.2.2	Automatic ROI Classification	80
6.2.3	Features	81
6.2.4	Classifier	81
6.3	Results	82
6.3.1	Training Set	82
6.3.2	Test set	82
6.3.3	Best feature subset	83
6.4	Discussion	83

7	Lesion classification using Multiple Classification System	85
7.1	Introduction	85
7.2	Methods	87
7.2.1	Morphological and Dynamic features	87
7.2.2	VOI Classification	87
7.3	Results	89
7.4	Discussion	90
8	General Discussion	92
8.1	Comparison of kinetic models	93
8.2	Influence of parameterisation in kinetic modelling estimation	94
8.3	Motion artifacts	94
8.4	Automatic simultaneous pixel classification and tracer kinetic modelling using EM approach	95
8.5	Automatic Segmentation and Classification using Machine Learning approach	96
8.6	Quantitative morphologic and textural assessment	96
8.7	Assessment of treatment effects	97
8.8	Future endpoints	97
9	List of publications	98
9.1	Books Coauthors	98
9.2	Journal publications	98
9.3	Conference proceedings	99
	Bibliography	103

Acknowledgements

I would like to thank to my PhD advisors, Professor Mario Sansone and Doctor Antonella Petrillo, for supporting me during these past three years.

Mario has been supportive and has given me the freedom to pursue various projects without objection. He has also provided insightful discussions about the research. He is my primary resource for getting my science questions answered and was instrumental in helping me crank out this thesis, all in one month.

I am very grateful to Antonella Petrillo for his scientific advice and knowledge and many insightful discussions and suggestions.

I thank the PhD Coordinator, Professor Angelo Cappello, for the opportunity and the great experience that made me live. I thank my supervisor Mario Cesarelli for the help provided in these years of PhD. I thank the examiners, Professor Mario Ursino and Doctor Paola Scifo, for the excellent suggestions given me. I also have to thank all members of my PhD committee.

I thank all the present members of the National Cancer Institute of Naples where I did my scientific activity.

I also thank my friends (too many to list here but you know who you are!) for providing support and friendship that I needed.

I especially thank my mom, grandmother, my sisters and Enzo. I love them so much, and I would not have made it this far without them. My sisters have been my best friend all my life and I love her dearly and thank her for all her advice and support.

Special thanks to Rosario and his family. The best outcome from these past years is finding my best friend and soul-mate. There are no words to convey how much I love him. Rosario has been a true and great supporter and has unconditionally loved me during my good and bad times. He has been non-judgmental of me and instrumental in instilling confidence. He has faith in me and my intellect.

I feel that what I learned thanks a this PhD is strengthen my commitment and determination and to live life to the fullest.

Summary

Dynamic contrast enhancement techniques using iodinated contrast media have been employed routinely in computed tomography for many years and can help the radiologist considerably in narrowing down the differential diagnosis of tumors by adding functional information to the anatomically detailed morphological images. One of the many advantages of magnetic resonance imaging is the possibility to use not one but several types of contrast media, each with its specific composition and particular properties.

The functional imaging capabilities of dynamic contrast-enhanced MRI (DCE-MRI) are for that reason substantially greater than those of dynamic contrast-enhanced CT. Contrast-enhanced MR is now well established as a high-performance imaging modality for the diagnosis and management of patients with solid tumors.

The diagnosis, grading and classification of tumours has benefited considerably from the development of DCE-MRI which is now essential to the adequate clinical management of many tumour types [19].

The ability of MRI to demonstrate tumour morphology and the relationships of malignant lesions to neighbouring structures provides essential clinical information for both clinical management and surgical planning. Magnetic resonance has innate advantages in these applications enabling clear delineation of normal anatomical structures and organs and, in most cases clearly delineating and identifying pathological change. The ability to acquire multiplanar images or even volume acquisitions is extremely valuable and provides the clinician with a true three dimensional appreciation of tumour and tissue morphology. The development of small molecular weight paramagnetic contrast agents has had a major impact on the application of magnetic resonance in oncology. Many tumours exhibit distinctive enhancement patterns which may increase their conspicuity and provide useful diagnostic or staging information [10] - [11].

Several strategies have been proposed for DCE-MRI evaluation. Visual

inspection of contrast agent concentration curves vs time is a very simple yet operator dependent procedure [64], therefore more objective approaches have been developed in order to facilitate comparison between studies. In so called model free approaches, descriptive or heuristic information extracted from time series raw data have been used for tissue classification [7, 8]. The main issue concerning these schemes is that they have not a direct interpretation in terms of physiological properties of the tissues.

On the other hand, model based investigations typically involve compartmental tracer kinetic modelling 5.1 [21, 23, 24, 25, 26, 30, 40, 39, 41, 42] and pixel-by-pixel estimation of kinetic parameters via non-linear regression [74] applied on region of interests (ROIs) opportunely selected by the physician [75]. This approach has the advantage to provide parameters directly related to the pathophysiological properties of the tissue such as vessel permeability, local regional blood flow, extraction fraction, concentration gradient between plasma and extravascular-extracellular space [21]. Anyway, nonlinear modelling is computational demanding and the accuracy of the estimates can be affected by the signal-to-noise ratio (SNR) and by the initial solutions [74].

The principal aim of this thesis is investigate the use of semi-quantitative and quantitative parameters for segmentation and classification of breast lesion in DCE-MRI. The objectives of works can be subdivided as follow:

1. describe the principal techniques to evaluate the time intensity curve in DCE-MRI with focus on kinetic model proposed in literature;
2. evaluate the influence in the choice of parametrization for a classic bi-compartmental kinetic models
3. evaluate the performance of a method for simultaneous tracer kinetic modelling and pixel classification in suspicious and not suspicious
4. evaluate the performance of machine learning techniques training with morphological, textural and dynamic feature for segmentation and classification of breast lesion

Chapter 1

An Introduction to Dynamic Contrast-Enhanced MRI in Oncology

The diagnosis, grading and classification of tumours has benefited considerably from the development of magnetic resonance imaging (MRI) which is now essential to the adequate clinical management of many tumour types.

The ability of MRI to demonstrate tumour morphology and the relationships of malignant lesions to neighbouring structures provides essential clinical information for both clinical management and surgical planning. Magnetic resonance has innate advantages in these applications enabling clear delineation of normal anatomical structures and organs and, in most cases clearly delineating and identifying pathological change. The ability to acquire multiplanar images or even volume acquisitions is extremely valuable and provides the clinician with a true three dimensional appreciation of tumour and tissue morphology. The development of small molecular weight paramagnetic contrast agents has had a major impact on the application of magnetic resonance in oncology. Many tumours exhibit distinctive enhancement patterns which may increase their conspicuity and provide useful diagnostic or staging information.

Dynamic contrast enhanced MRI (DCE-MRI) is now widely used in the diagnosis of cancer and is becoming a promising tool for monitoring tumour response to treatment [10, 11, 19, 15, 33, 19, 68].

DCE-MRI is a functional modality which involves the administration of an adequate contrast agent (typically Gadolinium DTPA) and, subse-

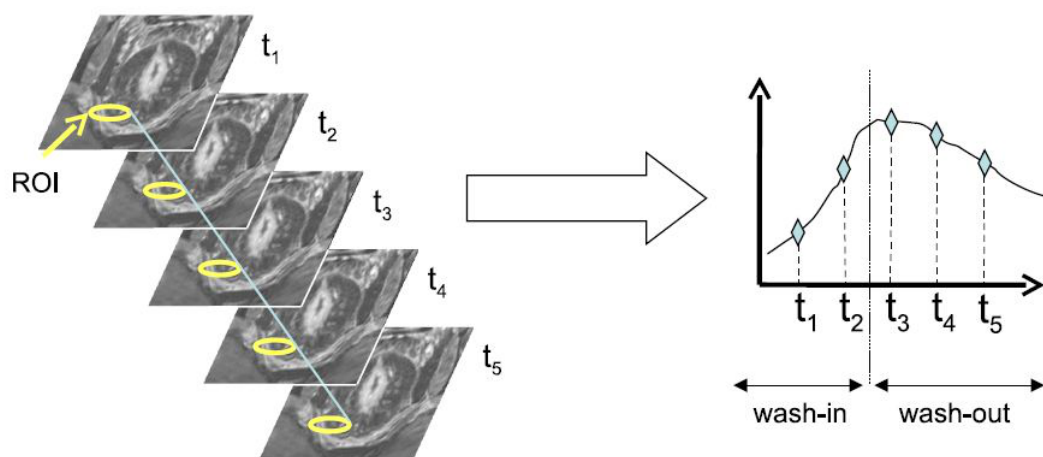


Figure 1.1: After intra venous injection the contrast medium (usually Gadolinium) travels through the vessels walls toward the extravascular extracellular fluid and subsequently it returns back to the main blood flow. MRI signal intensity changes according to contrast medium concentration within voxels. The time course of Gadolinium concentration (tracer kinetics) can be adequately described using opportune models whose parameters are strictly related to the angiogenic activity.

quently, the assessment of signal intensities changes over time. The signal intensity on T1-weighted images can be considered proportional to the concentration of contrast agent (see Fig. 1.1).

Dynamic contrast enhancement patterns can be affected by a wide range of physiological factors which include vessel density, blood flow, endothelial permeability and the size of the extravascular extracellular space in which contrast is distributed [13, 49, 50, 51]

Many different methods for image acquisition and data analysis have been described for use in DCE-MRI. The analysis models are designed to derive the optimal biologically relevant components from the dynamic MR signal changes and to relate these to the underlying pathophysiological processes taking place in the tissue. In particular dynamic contrast enhanced MRI combined with physiological model-based analysis has been widely used in the study of tumour angiogenesis and in the development and trial of anti angiogenic drugs. The derivation of physiological data from dynamic contrast MRI relies on the application of appropriate pharmacokinetics models to describe the distribution of contrast media following its systemic administration. A range of modelling techniques are

available which will be discussed in details in chapter Chap. 2.

However, these techniques are complex and are not widely available outside specialist centers [21, 14]. In response to this many quantitative or semi-quantitative approaches for the classification of enhancement curve shapes have been described and are now in relatively common use in clinical settings [34]. As we shall see even these simplistic approaches for data analysis can provide extremely valuable information for clinical management.

A range of semi-quantitative parameters will be discussed in details in chapters 2 and 5.

1.1 Pathophysiological Basis of Contrast Enhancement

Numerous studies using dynamic contrast enhanced MRI have demonstrated that malignant tumours generally show faster and higher levels of enhancement than is seen in normal tissue [10, 11, 38].

This enhancement characteristic reflects the features of the tumour microvasculature which in general will tend to demonstrate increased proportional vascularity and higher endothelial permeability to the contrast molecules than do normal or less aggressive malignant tissues. Cancer can develop in any tissue of the body that contains cells capable of division.

The earliest detectable malignant lesions, referred to as cancer in situ, are often a few millimeters or less in diameter and at an early stage are commonly avascular. In avascular tumours cellular nutrition depends on diffusion of nutrients and waste materials and places a severe limitation on the size that such a tumour can achieve [1].

The maximum diameter of an avascular solid tumour is approximately $150 - 200\mu m$, and is governed effectively by the maximum diffusion distance of oxygen. Avascular tumours of this nature are not detectable by MRI [1]. Conversion of a dormant tumour in situ to a more rapidly growing invasive neoplasm, may take several years and is associated with vascularization of the tumour.

The development of neovascularization within a tumour results from a process known as angiogenesis [1].

There are positive and negative regulators of angiogenesis. Release of a promoter substance stimulates the endothelial cells of the existing vascu-

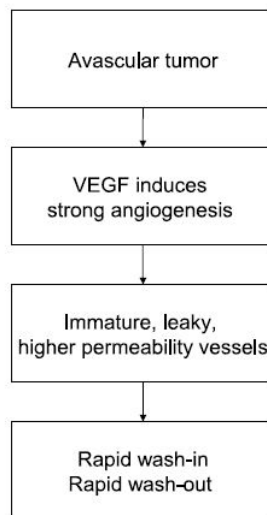


Figure 1.2: A summary of the main phases of tumor vasculature development (angiogenesis) and the effects that are measurable by means of DCE-MRI.

lature close to the neoplasia to initiate the formation of solid endothelial sprouts that grow toward the solid tumour [1].

Vascular endothelial growth factor (VEGF) also known as vascular permeability factor (VPF), induces angiogenesis and strongly increases microvascular permeability to plasma proteins. As vascular growth factors are released, proteases are also induced to degrade perivascular tissue, allowing the endothelial cells to proliferate and form primitive, immature, and, therefore, leaky vessels. Figure 1.2 summarizes the main phases of tumor vasculature development.

Therefore, the morphology of the neovascular network in tumours can differ significantly from that seen in normal tissue. Tumour vasculature is often highly heterogeneous, and the capillaries are extremely coarse, irregularly constricted or dilated, and distorted with twisting and sharp bends [1].

The degree of abnormality seen within the tumour or the vascular bed appears to depend on whether structural maturation can occur at a rate sufficient to keep in step with the angiogenic process.

The angiogenic cascade, regulated by pro-angiogenic factors such as vascular endothelial growth factor, involves proliferation, migration, and differentiation of endothelial cells to form new capillaries.

*CHAPTER 1. AN INTRODUCTION TO DYNAMIC
CONTRAST-ENHANCED MRI IN ONCOLOGY*

In the tumor environment this process is however not well-controlled, resulting in structural and functional abnormalities; an important one being high vessel-wall permeability due to incomplete endothelium lining and an interrupted basement membrane. In addition, the smooth muscle layer that assures vasoreactivity is often underdeveloped or lacking.

The onset of angiogenesis adds to the malignant potential of the tumor because it enables (rapid) tumor growth and provides access to the blood circulation, thereby increasing the risk of metastases. However, the increased vasculature also provides access to the tumor, such that contrast materials and drugs can be delivered, to, respectively, detect and treat it. High-grade tumors tend to present higher vascular disorganization and permeability than low-grade tumors.

Tumor grade is defined as the histological degree of cell abnormality; the less the cells are differentiated into normal cells, the higher the grade and the faster the cells grow and spread. Monitoring tumor vascularization could therefore potentially help to predict tumor aggressiveness and to design a tailored treatment [23] .

On the basis of this histopathological evidence it has been suggested that DCE-MRI may also be able to provide independent indices of angiogenic activity and therefore act as a prognostic indicator in a broad range of tumour types. Clearly, if this is substantiated then the non-invasive technique of magnetic resonance imaging would have significant advantages over other methods which rely on tissue sampling and secondary histopathology.

While avascular tumours are not detectable by MRI [19], DCE-MRI can help to characterize vascularized cancers [68]. After intravenous injection, the contrast agent (CA) pass through the tumor vasculature and immediately leaks through the vessels walls accumulating in the extravascular extracellular space (EES) because of the concentration gradient (wash-in phase). Hereafter, CA concentration within plasma will return lower than EES and backflow will occur (wash-out phase). Using specific T1-weighted pulse sequences the accumulation of CA causes an increase of signal intensity (enhancement) on images, Malignant tumors generally show faster and higher levels of enhancement than is seen in normal tissue. DCE-MRI is currently widely used in the study of tumour angiogenesis and in the development and trial of anti angiogenic drugs.

1.2 Breast cancer imaging

In most industrialized countries breast cancer will affect one out of eight women during her lifetime. Prevalence of male breast cancer is about 90 times lower. In the USA, after continuously increasing for more than two decades, incidence rates are slowly decreasing since 2001. Since 1990, death rates from breast cancer have steadily decreased in women, which is attributed to both earlier detection and improved treatment. Still, it is second only to lung cancer as a cause of cancer death in women. In this work we propose an automatic method for segmentation and classification of breast lesion via quantitative analysis of magnetic resonance images (MRI).

Screening and diagnosis of breast cancer are generally performed using X-ray mammography, possibly in conjunction with ultrasonography. As a screening modality, MRI is only used for women at high risk - among other reasons - because of its superior sensitivity in young women.

In this work, we will focus on MR imaging of the breast. More specifically, the DCE-MRI part of the protocol will be highlighted, as well as radiological assessment of DCE-MRI data. The current standard of care will be reviewed and directions for improvement will be pointed out.

Most breast cancers are diagnosed using (X-ray) mammography, which is the standard screening modality. Although mammography is the only screening test proven to reduce breast cancer mortality, there is increased awareness that mammography alone may not be adequate to screen certain subpopulations. Those subpopulations consist for instance of women with a genetic predisposition to develop breast cancer - such as carrying one of the BRCA mutations - women with a personal history of cancer, or women who have undergone chest radiation.

As they are at high-risk (aggregate lifetime risk of more than 20%), these women should start screening at a relatively young age, when breast tissue is often mammographically dense. A high density arises from a high calcium concentration causing a high background signal on mammography, possibly obscuring microcalcifications that can be a sign of cancer. Moreover, a high density is also a risk factor in itself. For women at high risk, the addition of either MRI or ultrasound to mammography results in a higher detection yield than achieved with mammography alone, as can be seen in Table 1.3.

Therefore, for these women, additional screening beyond annual mammography has been advised by the American Cancer Society since 2007. Preferably MRI is used, because the combination of MRI with standard

Modality	% of cancers found
Mammography	36
Ultrasound	40
Mammography + Ultrasound	52
Magnetic resonance imaging	81
Mammography + magnetic resonance imaging	93

Figure 1.3: High risk screening, percentage of cancers found per modality and per combination of modalities

mammography gives the highest detection rate. For women at normal risk, MRI can be used in case of a suspicious but inconclusive mammogram. However, ultrasound is more commonly used as a second-look modality.

If diagnosis calls for treatment, MRI could be used to assess the extent of disease. However, this use of MRI, as well as the use of MRI for (contralateral) screening, is currently vehemently debated as it may (unnecessarily) increase recall and intervention rates. An increase of the false positive ratio has been reported, although others state that the specificity of MRI is similar to that of mammography [64]. The reported range in specificity is therefore large (37-97%). On the part of sensitivity there is consensus that it is higher for MRI (77-100%) than for mammography (25-59%). Possibly, improvements in standardization can contribute to a higher and more uniform specificity. During the treatment phase, MRI can be used to monitor the response to (neoadjuvant) chemotherapy or other therapies. For agents acting on the tumor vasculature it can be crucial to use MRI for therapy assessment, because it can provide information about the degree of vascularization and the quality of the vessels.

1.3 Patient Examination

DCE-MRI can be satisfactorily performed on the majority of currently available clinical scanners.

Because of the requirements for high temporal resolution there will be restrictions on spatial resolution and spatial coverage dependent on

gradient performance. However, it should be stressed that useful clinical information can be obtained in many applications using even a single slice of dynamic data. The majority of currently available clinical scanners will comfortably allow multislice acquisitions to be performed with adequate temporal resolution for most analysis techniques.

Contrast administration is performed through a peripheral vein. A large antecubital vein is commonly employed and the injections can be given through a small cannula which should be inserted and secured in place prior to the investigation. The injection technique is of considerable importance. Most dynamic imaging methodologies use a bolus injection of contrast and it is important that this be administered in a consistent manner.

Most centers now use an automated pressure injection system to ensure reproducibility.

Protocols for contrast administration vary depending on the technique in use. Typically however, a single dose of contrast (0.1 mmol/Kg) of a standard gadolinium chelate will be administered at a rate in the region of 4 ml/s. Some centers prefer to vary the injection rate so that the overall period of contrast administration is kept constant rather than having a constant injection rate of different volumes in different patients. It is important that the contrast bolus remain coherent in its passage through the body and in order to achieve this a chaser injection of normal saline is given immediately after the contrast.

The chaser injection must be given at the same flow rate as the contrast and must be of adequate volume to empty the draining veins, typically 20-30 ml, so that the contrast passes into the systemic circulation as a coherent bolus.

The venous injection should be placed into the right arm if possible since variations in venous anatomy can lead to significant jugular reflux on the left side which can impair the coherence of the contrast bolus [1].

The imaging of the dynamic sequence is usually performed following initial anatomical and localization scans.

Problems associated with respiratory and other physiological motion and with the presence of inflow artefact distorting the dynamic contrast signal in blood vessels must be considered.

If it is intended to use a simple subjective or semi-quantitative analysis of enhancement curve then the dynamic image series provides adequate data for this approach. If it is intended to use a pharmacokinetics analysis then it is necessary to calculate contrast concentration in each image in the dynamic series.

Unfortunately the relationship between contrast concentration and signal intensity is non linear (see Chap. 3) and will be affected by the underlying native T1 of the tissues. For pharmacokinetics analysis it is therefore necessary to add additional imaging sequences to the investigation before the dynamic run is performed.

These sequences are designed to allow calculation of quantitative T1 maps to enable subsequent calculation of contrast concentration. The approaches taken for T1 mapping and the imaging methods employed are also described in detail in Chap. 3.

The dynamic sequence is performed following preliminary anatomical imaging and T1 mapping. The choice of image acquisition technique, injection rate and temporal resolution will be entirely dependent on the analysis method to be employed.

1.4 Dynamic MR Acquisition Techniques

There are two generic approaches for the acquisition of dynamic contrast enhanced MRI data. Relaxivity based methods use T1-weighted acquisitions whilst susceptibility-based techniques use T2 or more commonly T2*-based sequences. Both methods have specific advantages and disadvantages and historically they have tended to be used in different applications.

Typical modern clinical MR scanners can offer a variety of choices of pulse sequence which are suitable for dynamic contrast enhanced magnetic resonance applications. Despite this the sequence chosen will almost always be a compromise between a number of imaging quality factors including time, spatial resolution, anatomical coverage, sensitivity to artefact, image signal to noise ratio (SNR) and degree of contrast weighting.

T1-weighted DCE-MRI is most commonly acquired using gradient echo-based sequences which can be broadly divided into three groups: the steady state, the transient state and the echo planar-based sequences. Standard, balanced, gradient echo sequences have high sensitivity to T2 effects which is undesirable as the signal decreases once contrast agent arrives at the tissue. Many dynamic studies have therefore used spoiled gradient echo sequences which are more specifically sensitive to T1 effects and therefore show signal increases.

1.4.1 Breast DCE-MR Acquisition

In this study the patients underwent imaging with a 1.5 T scanner (Magnetom Symphony, Siemens Medical System, Erlangen, Germany) equipped with breast coil.

DCE-MRI was obtained with FLASH or TWIST sequences.

The protocols used in two cases was described in the following.

DCE T1-weighted FLASH 3-D coronal images were acquired with TR/TE: 9.8/4.76 ms; flip angle: 25 degrees; field of view 330x247 mmxmm; matrix: 256x128; thickness: 2 mm; gap: 0; acquisition time: 56 s; 80 slices spanning entire breast volume. One series was acquired before and 9 series after intra-venous injection of 0.1 mmol/kg of a positive paramagnetic contrast medium (Gd-DOTA, Dotarem, Guerbet, Roissy CdG Cedex, France). Three pre-contrast volumes were acquired with different flip angles (7, 12 and 25 degrees) in order to obtain T10 map in accordance with the standard methods proposed in literature [25].

DCE T1-weighted TWIST 3-D coronal images were acquired with TR/TE: 3.08/1.18 ms; flip angle: 25 degrees; matrix: 320x290; thickness: 2 mm; gap: 0 mm; acquisition time: 6.2 s; 64 slices spanning entire breast volume; 88 temporal series; pA:0.20, pB:0.20. The choice of pA and pB was based on the results of [54]. Five pre-contrast volumes were acquired with different flip angles (7, 12, 15, 20 and 25 degrees) in order to obtain T10 map in accordance with the standard methods proposed in literature [55].

Automatic injection system was used (Spectris Solaris EP MR, MEDRAD, Inc., Indianola, PA) and injection flow rate was set to 2 ml/s followed by a flush of 10 ml saline solution at the same rate.

1.5 Analysis of Dynamic Data

A large range of techniques have been applied to the analysis of the signal enhancement curves observed in DCE-MRI which range from simple visual inspection to complex quantification using applications of pharmacokinetics models.

Many analysis techniques are based on measurements taken from user-defined regions of interest (ROI). This has the advantage of ease of use but also has the disadvantage in that it produces a wide degree of variability and potential intraobserver errors into the technique. More importantly it is incapable of identifying or quantifying significant het-

erogeneity within the tumour microvascular which may occur within the region of interest.

Inappropriate selection of the ROI so that it includes both enhancing and necrotic or non-enhancing components of tumour would give rise to misleading interpretation. These shortcomings can be addressed by the production of calculated parametric images which allow pixel by pixel analysis of the calculated microvascular components. This pixel by pixel analysis deals specifically with tumour heterogeneity and potentially provides a far wider range of information concerning tumour behavior than is available from region of interest analysis. Unfortunately, the use of parametric images imposes significant further demands on the acquisition and analysis techniques. In particular, the use of pixel by pixel analysis assumes that there is no significant motion at the spatial resolution of the individual voxel. Since a typical voxel may be below 1 mm in size even small physiological motions can have significant impact on the calculated parameters.

For these reason in the chapter 5 was described an approach for simultaneous pixel by pixel classification (enhancing an not enhancing pixel) and tracer kinetic modelling in DCE-MRI.

Whatever approach to analysis is selected careful inspection of the original dynamic contrast series images is important. Visual review of these images will allow identification of significant patient motion or unexpected artefact which may have occurred during the dynamic acquisition and will also allow appreciation of the distribution of enhancement that has occurred in various tissues. This initial visual inspection is greatly aided by the use of simple subtraction techniques which can usually be performed on the scanner console or a standard clinical workstation.

1.5.1 Visual Inspection

A commonly used analysis of dynamic enhancement patterns is based upon a subjective evaluation of the time-signal intensity curve, in which each curve is classified in accordance with an evaluation system Classification of signal intensity curves according to the scheme achieved very good diagnostic performance in differentiating malignant from benign breast lesions as described by Daniel et. al. [34]. The high numbered curves are interpreted as representing more aggressive tumour types.

1.5.2 Enhancement Curve Analysis: model free and model based

A broad range of approaches have been taken to assess the properties of enhancement curves in various tumours [64]. Most of these techniques are designed to deal with baseline variations in signal intensity and with the inherent differences in signal intensity that would be observed due to changes in tuning and scaling factors between scanners or even between sessions on the same scanner.

The analysis models are designed to derive the optimal biologically relevant components from the dynamic MR signal changes and to relate these to the underlying pathophysiological processes taking place in the tissue. In particular dynamic contrast enhanced MRI combined with physiological model-based analysis has been widely used in the study of tumour angiogenesis and in the development and trial of anti angiogenic drugs. The derivation of physiological data from dynamic contrast MRI relies on the application of appropriate pharmacokinetics models to describe the distribution of contrast media following its systemic administration. A range of modelling techniques are available [21, 23, 25] and these will be described in the chapter 2 and 3. However, these techniques are complex and are not widely available outside specialist centers [21].

In response to this many quantitative or semi-quantitative approaches (analysis model free) for the classification of enhancement curve shapes have been described and are now in relatively common use in clinical settings [34]. As we shall see even these simplistic approaches for data analysis can provide extremely valuable information for clinical management. Overimaginative curve shape analysis techniques can be extremely valuable, particularly in clinical applications for the grading or classification of tumours. This reflects the fact that differences in tumour vasculature between benign and malignant tumours are large and maybe demonstrated by relatively crude analysis techniques. Despite their clear clinical utility the shortcomings of these subjective and semi-quantitative techniques have led many workers to develop more robust quantitative approaches to analysis. There are several reasons why more quantitative approaches may be beneficial. Firstly, the ability to produce measurements which reflected the physiological anatomical structure of the tumour microvasculature and which are truly independent of scanner acquisition and tumour type is highly attractive when compared to the use of a range of tissue or scanner specific semi-quantitative methods. Secondly, the development of precise and reproducible quantitative mea-

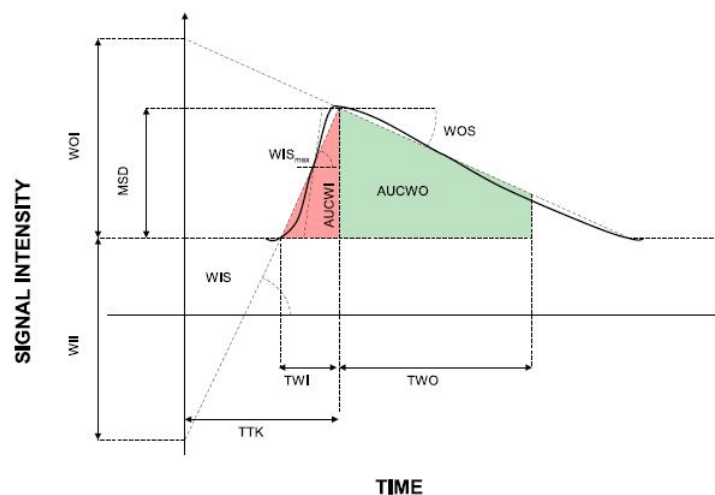


Figure 1.4: Semi-quantitative analysis: illustration of the parameters calculated from the TIC. See table 1.5 for definition of terms.

asures is highly desirable for use in longitudinal or multi-center studies. This is of particular importance in clinical trials of new therapeutic agents where the ability to test the hypothesis that an agent affects tumour microvasculature will depend entirely on the accuracy and reproducibility of the measure used. Thirdly, it must be appreciated that signal enhancement curves are a crude indicator of the contrast distribution mechanisms that are occurring within the voxel. Fourthly, simple analysis of contrast enhancement curves are unable to compensate for variations in the contrast delivery to the tumour, which might occur due to poor injection technique, anatomical variations or abnormal physiological features in the individual patients such as poor cardiovascular function. Since these techniques are widely used in cancer patients where venous access can be difficult and cardiovascular and renal functions are commonly compromised this can introduce significant variation into the results of quantitative analysis techniques.

We used semi-quantitative approach to obtain dynamic feature for segmentation and clarification of breast lesion (see chapter 6 and 7).

1.5.3 Semi-quantitative analysis

Semi-quantitative analysis can help the radiologist in classifying the TIC shape as normal, benign, malignant (see fig. 1.4).

CHAPTER 1. AN INTRODUCTION TO DYNAMIC
CONTRAST-ENHANCED MRI IN ONCOLOGY

Parameter	Definition
TTK	Time To Knee
TWI	Time of Wash-In
TWO	Time of Wash-Out
WII	Wash-In Intercept
WOI	Wash-Out Intercept
WIS	Wash-In slope
WOS	Wash-Out slope
MSD	Maximum Signal Difference
AUCWI	Area Under Wash-In
AUCWO	Area Under Wash-Out

Figure 1.5: Semi-quantitative analysis: definition of terms in fig. 1.4

Many papers explored the possibility to apply a semi-quantitative approach to lesion classification. Different TIC features have been used by the different authors, the aim being to extract as much physiological information as possible.

The approaches can be roughly subdivided in two classes. In a first type of approach, the classification of the TIC is performed by means of several features having, on an intuitive basis, a link with physiological characteristics 1.4. As an example, Tuncbilek et al. [9] used the maximal relative enhancement within the first minute (MSD_{1min}), the maximal relative enhancement of the entire study (MSD), the steepest slope (WIS_{max}). Similarly, Lavini et al. [7] and Varini et al. [8] used MSD and WISmax.

Another approach is to extract TIC features that are associated to tracer kinetics theory (see chapter 3). Within this framework de Lus-sanet et al. [17]; de Vries et al. [32] used, as a first step in quantitative assessment of tumor perfusion, the steepest slope of the TIC during contrast medium uptake (WIS_{max}), and they evaluated the Perfusion Index (PI) as:

$$PI = \frac{1}{\sigma_{tumor}} \left[\frac{dC_{tumor}/dt|_{max}}{\quad} \right] \quad (1.1)$$

$$= \frac{1}{\sigma_{tumor}} \left[\frac{WIS_{max}}{C_p(t)|_{max}} \right] \quad (1.2)$$

where σ_{tumor} is tissue density. Although PI is an approximated parameter, it combines two important quantities: tissue perfusion and extraction fraction [43]. When calculated on a pixel-by-pixel basis the above parameters can be displayed graphically as pseudo-colored maps superimposed on the corresponding morphological MR images.

Figure 1.4 shows the most important parameters that have been used in several studies. The definitions of the several quantities are not always in accordance. Therefore we have tried to use a unifying terminology for semi-quantitative parameters (see tab. 1.5):

TTK time between the beginning of dynamic acquisition and the maximum enhancement;

TWI time between the onset of enhancement and the maximum enhancement;

TWO time between the maximum enhancement and the end of the acquisition;

MSD the maximum signal level with respect to the baseline;

WIS slope of the wash-in phase (increase in signal intensity between enhancement onset and maximum enhancement divided by time to peak);

WOS slope of the wash-out phase (decrease in signal intensity between maximum enhancement and the signal intensity at the end of acquisition divided by time TWO);

WII intercept of the wash-in straight-line with the y-axis;

WOI intercept of the wash-out straight-line with the y-axis;

AUCWI area under gadolinium curve in the was-in phase;

AUCWO are under gadolinium curve in the wash-out phase.

1.6 Rationale

The aim of this work is to provide an automatic approach to analyze DCE-MRI data of the breast for segmentation and classification of breast lesion in DCE-MRI.

In Chapter 2 we will discuss and explain kinetic modeling starting from the physiological basis. The focus lies on Distributed and Compartmental Tracer Kinetic Models. In fact in the Chapter 3 we reported the results of

*CHAPTER 1. AN INTRODUCTION TO DYNAMIC
CONTRAST-ENHANCED MRI IN ONCOLOGY*

a comparison between distributed and compartmental kinetic modeling proposed in literature.

In Chapter 4 we evaluate the influence of parameterizations of a common compartmental kinetic model.

In Chapter 5 we propose a method to simultaneous segmentation simultaneous tracer kinetic modelling and pixel classification of DCE-MRI studies.

In Chapter 6 and 7 we will discuss and explain the use of machine learning for automatic segmentation and classification of breast lesion using semi-quantitative dynamic, textural and morphological features.

In Chapter 8 we report general discussion.

Chapter 2

Introduction to kinetic modeling

In the present chapter we provide an overview of kinetic models covering the most applied in the field of oncology. The application of the discussed models and methods is not limited to the context of dynamic contrast enhanced magnetic resonance imaging.

2.1 Introduction

Evidence has shown that microcirculatory parameters (eg, perfusion, blood volume, mean transit time, and vessel permeability) derived from dynamic contrast-enhanced imaging may be linked to the aggressiveness or angiogenic potential of the tumor and may be useful for diagnosis and monitoring of cancer therapy outcome [10, 11, 19, 6].

Pharmacokinetics describes what happens to a substance, e.g. drug or contrast agent, after it has been administered to a living organism.

This includes the mechanisms of absorption and distribution. The terms in which these mechanisms are described are physiological and therefore provide parameters describing the functioning of the organism's tissue.

In the field of DCE-MRI, pharmacokinetics is mainly studied by means of compartment modeling. Compartment is a modeling concept and does not necessarily describe a singular physical location. A compartment can be defined as an amount or volume of material. The interconnected compartments that are involved in the distribution of the substance define the system. A compartment by itself is assumed to be kinetically homogeneous, the kinetic behavior is the same across the compartment. It is also assumed to be well-mixed: a single concentration is expected

within the compartment. A physiological process can be modeled at different levels of detail, depending on the necessity to capture the complexity of the specific process. Different model systems, differing in the number of simplifying model assumptions, can therefore describe the same physiological process. For T1-weighted DCE-MRI, a variety of tracer kinetic models have been developed during the last two decades [21, 23, 24, 25, 26, 30, 40, 39, 41, 42]. In this section we introduce the general framework for kinetic models and principal compartmental and distributed models proposed in literature and the associated contrast agent input functions which we have considered.

2.2 General framework for pharmacokinetics modelling

All the models considered here make some basic assumptions related to concepts in tracer kinetics. These include the following:

- Compartments exist that contain the well-mixed tracer in a uniform concentration that cannot cross the cell membrane and enter the cells. It is customary to represent the tissue as comprising three or four compartments (see figure 2.1). Major compartments are: the vascular plasma space, the extra-cellular extra-vascular space (EES), and the intracellular space. A fourth tissue component forms a catch-all for all the other microscopic tissue components, such as membranes, fibrous tissues, etc. All clinically utilized MRI contrast agents, and most experimental agents, do not pass into the intracellular space of the tissue, due to their size, inertness, and non-lipophilicity, making the intra-cellular space un-probable using DCE-MRI; for this reason, the intra-cellular and other volumes are usually lumped together as a loosely defined intra-cellular space.
- Linear inter-compartment flux. The flux between compartments is proportional to the difference of concentrations in two compartments.
- Time invariance. The parameters describing the compartments are constant during the time that data are acquired.

We will indicate the quantities associated to the EES, plasma and intra-cellular compartments with the subscripts e, p and i respectively.

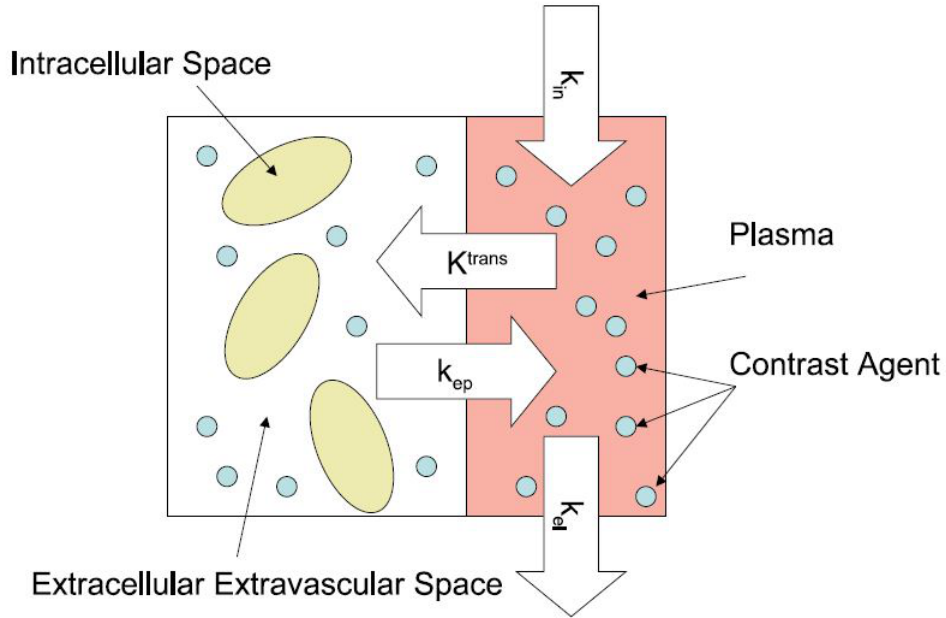


Figure 2.1: Major compartments and functional variables involved in the distribution of the contrast agent in the tissue.

The quantities associated to the whole tissue will be marked by a subscript T. The volume occupied by the different compartments may be expressed either as an absolute value (V_e, V_i, V_p, V_T) or as fractions (v_e, v_i, v_p) of V_T . They must satisfy the constraint:

$$v_e + v_p + v_i = 1. \quad (2.1)$$

Under these assumptions the rate of wash-in and wash-out of the CA in the EES can be described by a modified general rate equation [1]:

$$v_e \frac{dC_e(t)}{dt} = K_{trans}(C_p(t) - C_e(t)). \quad (2.2)$$

where C_e and C_p are the CA concentrations [mmol/L] in V_e and V_p respectively; K_{trans} [min^{-1}] is the volume transfer constant between V_e and V_p (see fig. 2.1) [21]. K_{trans} is associated to both the vessel permeability and blood flow.

There exist a fundamental relationship between K_{trans} and v_e [14]:

$$v_e = \frac{K_{trans}}{k_{ep}} \quad (2.3)$$

where k_{ep} is the rate constant and it is linked to the duration of the wash-out phase. The other two parameters in fig. 2.1 represent the input function from the injection of gadolinium based contrast (k_{in}) and the clearance rate (k_{el}) [19].

Both blood plasma flow and blood perfusion (capillary permeability) contribute to the value of K_{trans} . If the flow of CA to the tissue is large, K_{trans} is dominated by the capillary wall permeability (permeability surface area, PS); if the delivery of CA to the tissue is insufficient, blood perfusion will be the dominant factor, and K_{trans} will be proportional to the blood flow F (volume of blood per unit time):

$$K_{trans} = F \cdot E \quad (2.4)$$

where F is the flux, E is the extraction fraction of the tracer $E = 1 - \exp(-PS \cdot F)$ (PS is the permeability surface area product). The relationships described above form the basis of the models used to describe contrast agent kinetics by a number of researchers, and the conventions for the names and symbols used are now generally accepted ([14]).

In normal tissues, the vascular volume is a small fraction $v_p \approx 0$ of the total tissue volume V_T (approximately 5%, although it can be considerably higher in some tissues), and it is sometimes assumed (largely as a matter of convenience) that the tracer concentration in the tissue as a whole, C_T , is not influenced to a large degree by the concentration in the vessels (i.e. $C_T = v_p C_p + v_e C_e \simeq v_e C_e$).

While this assumption is acceptable in abnormalities with small increase in blood volume, that are located in tissues with a relatively low normal blood volume, it is not valid in many contexts, especially because blood volume can largely increase in tumours. Perhaps the most straightforward approach is to extend eq. 9 to include the concentration of contrast agent in the blood plasma, giving $C_T = v_p C_p$.

Using this relationship and eq. 2.2 we have the extended Tofts' model

$$C_T(t) = v_p C_p(t) + K_{trans} \int_0^t C_p(\tau) \exp(-k_{ep}(t - \tau)) d\tau \quad (2.5)$$

More comprehensive models, such as the one proposed by St Lawrence and Lee can allow direct quantification of flow (F), extraction fraction (E), v_e and mean capillary transit time (MTT). Here, rather than defining a composite parameter K_{trans} , it is possible to separately estimate F and PS (permeability surface area product). As this model has many parameters,

successful application requires a high temporal resolution and an accurate measurement of CT, which limits its application in clinical trials. The tissue concentration is given by the following equation [25]:

$$C_T(t) = F \int_0^{MTT} C_p(t-u)du + E \cdot F \int_{MTT}^t C_p(u) \exp\left(-\frac{E \cdot F}{v_e}(t-u-MTT)\right) du \quad (2.6)$$

In general, the aim of the compartmental analysis is to estimate the parameters K_{trans}, v_p and v_e from DCE-MRI data. This problem can be seen either as a system identification problem or as a non linear regression problem that will be described in chapter 4.

2.3 Influence of the arterial input function

From eq. 2.5 it is clear that the C_T can be seen as the output of a linear system whose impulse response is determined by the tracer kinetics parameters K_{trans} and v_e and whose input is the AIF. Therefore, errors in estimation of AIF can seriously affect the parameters estimates.

AIF can be obtained by direct measurement of blood flux [73]. For example, Larsson et al. [24] utilized an AIF measured from blood samples drawn from the brachial artery at intervals of 15 s during the DCE-MRI data acquisition. This method is not suitable for clinical practice and other approaches have been proposed.

One of the simplest methods was proposed by Brix et al. [23]: they assumed that AIF followed a mono-exponential model and included it as a third parameter directly into the TIC model.

Another approach for modelling of arterial flux was based on population parameters: the early application proposed by Tofts [21] assumed a bi-exponential form of the AIF as previously found in normal population [48]. Also multi-exponential modelling by means of nonlinear fitting of arterial flux measured directly on the images on a patient by patient basis has been investigated [24].

Exponential modelling has shown to be only applicable when the sampling rate is relatively slow and there is a negligible plasma fraction. When the plasma fraction is non-negligible, this approach tends to overestimate the volume transfer constant K_{trans} . To overcome this problem, Parker et al. ([57] measured a high temporal resolution population AIF on a large number of individuals and estimated the parameters of a sophisticated model. Later, Orton et al. [57] proposed a computationally efficient

version of this model decomposing the input function into a bolus model and a body transfer function:

$$C_p(t) = A_B \cdot t \cdot \exp(-m_B t) + A_G(\exp(-m_G t) - \exp(-m_B t)) \quad (2.7)$$

with $A_B = a_B - a_B a_G / (m_b - m_g)$ and $A_G = a_B a_G (m_b - m_g)^2$; m_B , a_B and m_G , a_G are the transfer rate and the amplitude of two terms respectively.

A similar model for AIF has been previously proposed by Simpson et al. [30]:

$$C_p(t) = A \cdot t \cdot \exp(-B \cdot t) + C[1 - \exp(-D \cdot t)](\exp(-E \cdot t)) \quad (2.8)$$

where A, B, C, D, E were estimated on an individual basis. Also, other approaches based on reference tissues have been proposed [18]. The development of many analysis methods has proceeded in tandem with specific data acquisition programmes, and the modelling assumptions frequently reflected limitations imposed by the data. Care must therefore be taken in applying these methods in settings other than those originally intended and in comparing apparently compatible results from different studies using different models and/or data acquisitions.

2.4 Tissue CA Concentration for principal kinetic models and corresponding AIF

In this section we described the principal kinetic models used in literature with correspondent AIF.

2.4.1 Tofts model

In the Tofts model [21] the concentration of CA within plasma ($C_p(t)$) after the injection of a bolus of Gd (also called Arterial Input Function, AIF) was assumed to be the one measured in normal control subjects by Weinmann [48]. This was fitted to a bi-exponential decay, which is expected from the compartmental theory:

$$C_p(t) = D(a_1 \exp(-m_1 t) + a_2 \exp(-m_2 t)) \quad (2.9)$$

where D is the dose (mmol/kg). The fitted values were $a_1 = 3.99$ kg/L, $a_2 = 4.78$ kg/L, $m_1 = 0.144 \text{ min}^{-1}$, $m_2 = 0.0111 \text{ min}^{-1}$. Therefore, the time course of tissue concentration was modeled as follows:

$$C_T(t) = K_{trans}C_p(t) \otimes \exp(-k_{ep}t) + v_p C_p(t). \quad (2.10)$$

2.4.2 Brix model

In the Brix et al. model [23] the signal enhancement was assumed to be proportional to the concentration of CA in the tissue, the plasma concentration is fitted with single exponential decay characterized by a rate constant $k_{el}[\text{min}^{-1}]$. During the infusion of contrast material the CA concentration C_t is equal to:

$$C_T(t, A, k_{el}, k_{ep}) = \frac{A}{k_{el} - k_{ep}} \left(\frac{1 - \exp(-k_{ep}t)}{k_{ep}} - \frac{1 - \exp(-k_{el}t)}{k_{el}} \right) \quad (2.11)$$

where $A[\text{mmolmin}^{-1}L^{-1}]$ is the initial slope of the curve.

2.4.3 Tissue homogeneity model

Unlike the Tofts model, the Tissue homogeneity (TH) model defines the tracer concentration within the intravascular space (IVS) as a function of both time and distance along the length of the capillary. Owing to the small radial dimension of a capillary, radial concentration gradients can be neglected. Within the EES, the tracer concentration is assumed to be homogeneous (i.e., well mixed) in its spatial distribution, and therefore, within this space the TH model is compartmental.

The capillary-tissue unit as defined by the TH model is illustrated in Fig. 2.2. From conservation of the mass of tracer in both the IVS and the EVS, the following equations can be derived

$$A_i \frac{\delta C_i(x, t)}{\delta t} = -F \frac{\delta C_i(x, t)}{\delta x} - \frac{PS}{L} \left[C_i(x, t) - \frac{C_e(t)}{F/k_{ep}} \right] \quad (2.12)$$

$$A_e L \frac{\delta C_e(t)}{\delta t} = \frac{PS}{L} \int_0^L \left[C_i(x, t) - \frac{C_e(t)}{F/k_{ep}} \right] dx \quad (2.13)$$

where A_i is the cross-sectional area of IVS, A_e is the cross-sectional area of EES and L is the length of capillary along the x-axis.

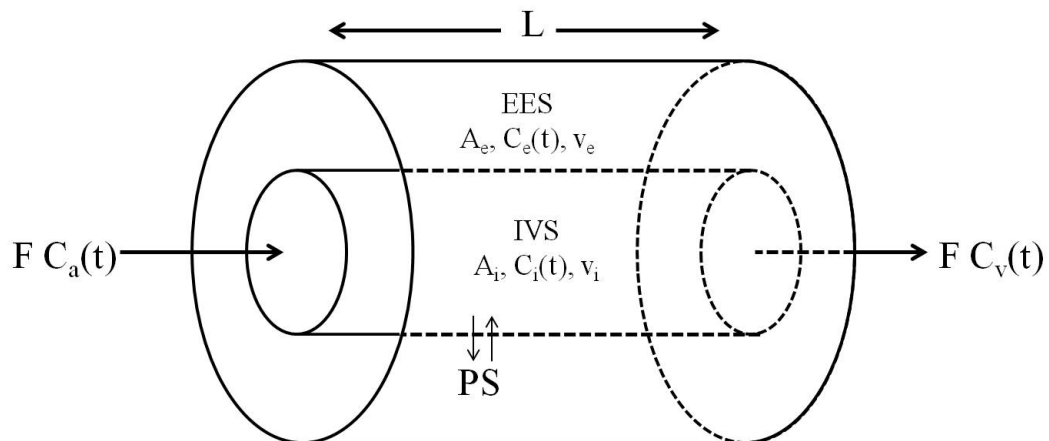


Figure 2.2: The capillary-tissue unit as assumed by the tissue homogeneity model. The model is comprised of an intravascular space (IVS) surrounded by an extravascular space (EES). Both spaces are of equal length, L , measured along the x axis, which is the direction of flow. The two spaces are separated by the blood-brain barrier, which has a permeability-surface area product denoted by PS . Both spaces have an associated cross-sectional area, A_k , volume V_k , and tracer concentration $C_k(t)$, where $k = i$ or e . The model assumes that only the IVS tracer concentration is a function of position. Blood flows into the capillary-tissue unit by means of the arterial blood at a flow rate F and concentration $C_a(t)$ and exits by means of the venous blood at the same flow rate and a concentration $C_v(t)$.

2.4.4 Adiabatic approximation to the tissue homogeneity (ATH) model

The closed-form solution of the TH model exists only in Laplace space. In this section it is shown that an approximate closed-form solution in the time domain can be derived using the adiabatic approximation [25]. This approximation is motivated by the fact that the concentration of labeled water in the EES ($C_e(t)$) changes slowly relative to that in the IVS ($C_i(t)$). Because of the difference in the time scale of these two events, for a small time interval, the slow event (i.e., the rate of change of ($C_e(t)$)) can be considered to be at a steady state while the fast event (i.e., the rate of change of ($C_i(t)$)) is taking place. The mathematical expression of the adiabatic approximation is to assume that within a small time increment (Δt), $C_e(t)$ is constant. Using the adiabatic assumption, $C_e(t)$ becomes discrete and is given formally as

$$C_e(t) = \sum_{j=0}^{n-1} \Delta C_e(j\Delta t) u(t - j\Delta) \quad (2.14)$$

where $\Delta C_e(j\Delta t)$ is the discrete jump in the value of $C_e(t)$ at time $j\Delta t$, and $u(t)$ is the unit step function.

The adiabatic solution to the TH model is derived by substituting Equation 2.14 for $C_e(t)$ in the differential Equations governing mass conservation (Equations 2.12, 2.13).

According to the adiabatic approximation to the tissue homogeneity (ATH) model proposed by [25], the concentration of CA in tissue, $C_i(t)$, can be considered equal to the convolution of the arterial input function, $C_p(t)$, and the tissue impulse response function $H(t)$:

$$H(t) = F t \leq T_c \quad (2.15)$$

$$H(t) = E \cdot F \exp\left(-\frac{E \cdot F}{v_e}(t - T_c)\right) t > T_c \quad (2.16)$$

The ATH is more complex than the Tofts and Brix model. It accounts for different contributions from the plasma flow rate F [$mL100g^{-1}min^{-1}$], extraction fraction through first-passage E , mean capillary transit time T_c [min]= v_i/F , and interstitial volume fraction v_e . The relationship with the above quantities K_{trans} and v_p can be obtained with following equations:

$$K_{trans} = E \cdot F v_p = T_c \cdot F \quad (2.17)$$

$C_p(t)$ can be estimated by means of non-linear fitting of the arterial flux measured directly on the images using the computationally efficient model recently proposed by [57].

With the adiabatic solution, $H(t)$ is divided into two phases in the time domain. For the vascular phase ($t < T_c$), $H(t)$ is equal to one owing to the finite time required for the labeled water to traverse the vascular space. During this phase, a fraction of the labeled water, denoted by E , is extracted into the EES. At $t = T_c$, the remaining fraction ($1 - E$) exits by means of the outflowing blood, and hence there is a discrete drop in $H(t)$. For $t > T_c$, which is the parenchymal tissue phase of $H(t)$, the fraction of labeled water extracted into the EES diffuses back into the IVS and is removed by blood flow, leading to clearance from the parenchymal tissue compartment (EES). As a corollary to the adiabatic approximation, because the time rate of change of the concentration of labeled water in the IVS owing to blood flow is much faster than that owing to diffusion, the capillary acts as a sink for the labeled water leaving the EES (by diffusion) during the parenchymal tissue phase. The rate of change of the tracer concentration in the EES, which for the TH model is considered a well-stirred compartment, can be expressed as

$$v_e \frac{dC_e(t)}{dt} = -EFC_e(t) \quad (2.18)$$

2.5 Estimation of Tracer Concentration

In DCE-MRI data analysis it is necessary to transform the signal intensity in tissue contrast agent concentration. Using a spoiled gradient echo acquisition, the signal intensity (S_t) from a tissue having longitudinal relaxation time T_1 and transversal relaxation time T_2^* can be described by eq. 2.19:

$$S_t = M_0 \sin(\alpha) \frac{1 - \exp\left(\frac{-TR}{T_1(t)}\right)}{1 - \cos(\alpha) \exp\left(\frac{-TR}{T_1(t)}\right)} \exp\left(\frac{-TE}{T_2^*}\right) \quad (2.19)$$

where α is the flip angle; TE is the echo time; TR is the repetition time; M_0 describes the scanner gain and proton density. To perform quantitative DCE-MRI data analysis, the time varying longitudinal relaxation time, $T_1(t)$, must be related to the concentration of contrast agent (CA) in the tissue, $C_t(t)$. Usually, a linear relationship between the two quantities is assumed [56] eq. 2.20:

$$R_1(T) = \frac{1}{T_1(T)} = r_1 C_t(t) + R_{10} \quad (2.20)$$

where R_{10} is the R_1 value of the tissue before CA administration and r_1 is the relaxivity of the CA. $R_{10} = 1/T_{10}$ may be estimated using several gradient echo images with different flip angles taken before contrast injection [55].

However, most studies assume that r_1 is constant at a given temperature and magnetic field and that it is independent on the tissue environment. The typical value used for r_1 , estimated in pure saline water, is 4.5 L/mmol/s per kg of water.

If it is assumed that Gd ions have no effect on ρ and that the TE is so short to neglect the influence of T_2 (or, more importantly, changes in T_2^* during the series), then the Gd ions can influence the signal intensity only by means of their effect on T_1 (decrease of T_1). Under these assumptions, and as α approaches 90° . and $TR \ll T_1$ the relationship between signal intensity and $1/T_1$ becomes approximately linear:

$$S = \rho g \frac{TR}{T_1} \quad (2.21)$$

this relationship remains approximately valid across a range of values for TR/T_1 and α . Therefore, an estimate of CA concentration can be obtained using eq. 2.20 and eq. 2.21:

$$Gd = 1/r_1 \cdot \left(\frac{1}{T_1} - \frac{1}{T_{1,0}} \right) \simeq \frac{S - S_0}{r_1 \rho g \cdot TR} \quad (2.22)$$

where S_0 , S , $T_{1,0}$ and T_1 are the signal intensities and spin-lattice relaxation times before and after administration of contrast agent respectively. The difference $S - S_0$ is called signal enhancement. The difficulty in comparing different studies comes from the nature of g : in fact, the loading of the coil, the receiver settings at the MR console and image reconstruction parameters can be different among several studies. Therefore, it could be more advantageous to normalize with respect to the pre-contrast signal intensity:

$$Gd \simeq \frac{S - S_0}{S_0} \frac{1}{r_1 \cdot T_{1,0}} \quad (2.23)$$

The quantity $\frac{S - S_0}{S_0}$ is called relative signal enhancement. Consequently, the concentration of CA is related to both r_1 and $T_{1,0}$ of tissue. As observed before, the relaxivity r_1 can be considered fixed for soft tissues. As

far as the longitudinal relaxation time prior to contrast injection ($T_{1,0}$) it can be easily measured before CA administration using opportune pulse sequences. One common method for $T_{1,0}$ estimation is to use several gradient-echo (GRE) images with variable flip angles. In fact, rearranging equation 2.19 yields:

$$Y = X \exp\left(\frac{-TR}{T_1}\right) - M_0(1 - \exp\left(\frac{-TR}{T_1}\right)) \exp\left(\frac{-TE}{T_2^*}\right) \quad (2.24)$$

where $Y = S_t \sin(\alpha)$ and $X = S_t \tan(\alpha)$. Hence a plot of Y against X for a range of flip angles will result in a straight line, and T_{10} maybe estimated from the slope.

Chapter 3

Distributed versus Compartmental Tracer Kinetic Models

In this Chapter 3 we reported the principal difference between distributed versus compartmental kinetic modeling and we reported the result of a comparison study.

This chapter contains work adapted from:

Sansone M, Fusco R, Aprile F, Petrillo A, Petrillo M, Siani A, Bracale U. Evaluation of different Tracer Kinetic Models in DCE-MRI of Rectal Cancer. Proceedings of 11th World Congress on Medical Physics and Biomedical Engineering, September 7-12, 2009 in Munich, German

Fusco R, Sansone M, Maffei S, Petrillo.A. Dynamic Contrast-Enhanced MRI in Breast Cancer: A Comparison between Distributed and Compartmental Tracer Kinetic Models. *Journal of Biomedical Graphics and Computing*, *Journal of Biomedical Graphics and Computing*, vol. 2, no. 2, p. p23, Aug. 2012.

3.1 Introduction

Tracer kinetic models used for estimating microcirculatory parameters can be broadly categorized as conventional compartmental (CC) or distributed- parameter (DP) models [21, 23, 25, 39]. While DP models

CHAPTER 3. DISTRIBUTED VERSUS COMPARTMENTAL TRACER KINETIC MODELS

seem to be more realistic, CC models (in particular the Tofts and the Brix models) have been widely used in clinical investigations over the past two decades.

Many investigations, especially clinical studies, have been published using CC models: in particular the Tofts [43, 44, 45, 39, 40] and the Brix models [39, 46, 47]. The former, proposed by Tofts and Kermode [21], used a population-based AIF with two exponentials, that was drawn from the literature concerning excretion of Gd-DTPA in the normal population (Weinmann et al. [48]). On the contrary, the model originally proposed by Brix et al. [23] used a single exponentially AIF by including one more parameter in the model. The Tofts and the Brix models (which have been shown to be both descending from a complete CC model [43]) have been widely used due to their simplicity [40, 49]. However, these methods are only applicable when permeability-limited conditions are met [43]. Moreover, although some results in separating benign from malignant lesions have been obtained [49], their acceptance in the clinical environment is not yet fully achieved, probably because of the not completely clear interpretation of some parameters (such as K_{trans}) which does not allow to separately consider flow (F) and permeability surface area product (PS).

On the other side, several authors [25, 50, 51] have reported that DP models could allow a more complete analysis of kinetic parameters: Larson et al [52] stated that CC models do not possess sufficient realism, because tracer concentration gradients within compartments are assumed to be zero at all times and consequently the tracer is assumed to distribute instantaneously on arrival in each compartment.

On the contrary, in DP models the concentration gradients in the vascular compartment are considered as a function of both time and space. The first DP model for two compartments was proposed by Johnson and Wilson [41] under the name of tissue homogeneity (TH) model; later, St Lawrence and Lee [12] proposed a simplified version with an adiabatic approximation of the tissue homogeneity model (ATH). The ATH model allows direct quantification of flow (F), extraction fraction (E), the clearance constant (k_{ep}) and the mean capillary transit time (Tc). Here, rather than defining the composite parameter K_{trans} , it is possible to separate the flow from permeability.

To date, studies reporting comparison between CC and DP models in the DCE-MRI context have been few. Donaldson et al. [50] provided a comparison among four different models: Tofts model, extended Tofts model with plasma fraction volume contribution, an uptake model and a general two-compartment exchange model (2CXM) in the carcinoma of

cervix. Their results suggested that the assumption of negligible plasma mean transit time is not appropriate in this context and the 2CXM is better suited for its analysis than the Tofts models. This demonstrated the importance of selecting an appropriate tracer kinetic model in DCE-MRI. Li et al. [51] compared four different models by applying four statistical measures (chi-square test, Durbin-Watson statistic, Akaike Information Criterion (AIC) and Bayesian Information Criterion (BIC)) to assess their capability to describe DCE-MRI data obtained in breast cancer. They examined the fast exchange limit model with (FXL- v_p) and without (FXL) a plasma component, and the fast and slow exchange regime models (FXR and SXR, respectively). They reported that the FXL- v_p and the FXR models provided the most complete statistical description of dynamic contrast-enhanced MRI time courses for the patients selected in their study.

Therefore, apart from the study by Zwick et al. [39], there is no direct comparison between Tofts and Brix models on real data; moreover, there is no direct comparison of CC models and DP models on real data in breast DCE-MRI.

A first study that has reported this comparison was performed by Fusco et al. [114].

3.2 A Comparison between ATH models and Compartmental Models

Three models were compared: two CC models (the Tofts and the Brix models) and one DP model (the ATH model). The objective of this study was two-fold:

- to compare DP (ATH) with CC models (Tofts and Brix) in breast DCE-MRI,
- to compare the Tofts with the Brix model on real data.

It should be pointed out that in this study were considered a few CC models that have been previously widely used in breast DCE-MRI (Tofts and Brix). Therefore, many other CC models have not been considered here (such as for example, the Patlak model [53], which was developed originally for blood-brain-barrier exchange, or the general two-compartment exchange model as analyzed by Donaldson [50]). In this

study were analyzed breast DCE-MRI data from 4 subjects with histologically proven invasive ductal carcinoma; they underwent DCE-MRI examinations in two different protocols: DCE-MRI with high temporal resolution obtained by means of a k-space under-sampling and data sharing method known as Time-resolved angiography With Stochastic Trajectories (TWIST) and DCE-MRI with low temporal resolution obtained by means of the common Spoiled Gradient-Echo k-space scheme (Spoiled Gradient Echo known as Fast Low Angle SHot (FLASH) [54]. This was done because the ATH model requires a sampling interval lower than the mean capillary transit time (T_c). FLASH data were used to perform the comparison between Brix and Tofts models in a typical clinical setting. Models have been compared using different goodness-of-fit metrics (residual sum of square (RSS), Bayesian Information Criterion (BIC), Akaike Information Criterion (AIC)). Moreover, a study of reliability of fit parameters estimation was performed.

For two women DCE T1-weighted FLASH 3-D coronal images were acquired Three pre-contrast volumes were acquired with different flip angles (7, 12 and 25 degrees) in order to obtain T10 map in accordance with the standard methods proposed in literature [25]. For the other two women DCE T1-weighted TWIST 3-D coronal images were acquired Five pre-contrast volumes were acquired with different flip angles (7, 12, 15, 20 and 25 degrees) in order to obtain T10 map in accordance with the standard methods proposed in literature [55].

3.2.1 Image and data Analysis

T10 maps were calculated using eq. 2.24. However, for all the voxels within a segmented ROI the T10 median value was used for CA quantification. This approach was inspired by Schabel et al. 2010 [49].

For $C_p(t)$ fitting using eq. 2.7 breast arteries have been manually selected. The starting estimates for A_B , A_G , m_B , m_G were chosen on basis of results of [57].

The starting estimates (see Table 3.1) for non linear regression of the tracer kinetic models were chosen using the kinetic parameters values found in literature [23, 59, 60].

For the parameters to fall in physiologically meaningful ranges, upper bounds were imposed on K_{trans} , v_p , v_e , A , k_{el} , F_p , E , and T_c to 1 min^{-1} , 1, 1, $10 \text{ mmol min}^{-1} L^{-1}$, 10 min^{-1} , $100 \text{ mL } 100g^{-1} \text{ min}^{-1}$, 1, and 100 s, respectively.

The data acquired with TWIST protocol were used to compare Tofts, Brix and ATH models while the data acquired with FLASH protocol were used to compare Tofts and Brix models.

Data fitting was performed using constrained nonlinear curve fitting in Matlab (v. 7.0; MathWorks, Natick, MA).

Table 3.1: Starting estimates for nonlinear regression.

	K_{trans}]	k_{ep}]	v_p	A	k_{el}	F_p	E	T_c
Tofts	0.5	0.5	0.05					
Brix		0.5		0.001	0.144			
ATH		0.5				21	0.7	6

3.2.2 Methods: Goodness-of-fit metrics used to compare kinetic models

In this study we used three different goodness of fit metrics: Residual Sum of Squares, Akaike Information Criterion and Bayesian Information Criterion.

A cost function commonly used for quantifying the goodness-of-fit between models and data is given by the residual sum of squares (RSS):

$$R^2 = \sum_{i=1}^N (y_i - C_t(i))^2 \quad (3.1)$$

where N denotes the number of observations, y_i is the observation at time i the $C_t(i)$ is the associated fitted value. The higher the R_2 value the higher the discrepancy between the data and the model. However, this metric is not well suited to compare models with different number of parameters (as is the case for Brix vs ATH or Tofts vs ATH). To this aim we used the Bayesian Information Criterion [61] and corrected Akaike Information Criterion (AICc) [62]. Both AICc and BIC make a balance between the goodness-of-fit and the model complexity in a similar manner (they have a common statistical basis in the Kullback-Leibler divergence [41]); however, the BIC applies a heavier penalty on the model complexity:

$$BIC = N \log(R^2/N) + p \log(N) \quad (3.2)$$

The AIC is computed via eq. 3.3:

$$BIC = N \log(R^2/N) + \frac{2p(p+1)}{N-p-1} \quad (3.3)$$

3.2.3 Methods: Reliability of Fit kinetic parameters

In order to evaluate the reliability of fit parameters a Monte Carlo simulation was performed. Per each model and per each voxel, the estimated parameters were used to compute the corresponding tissue concentration curve by means of eq. 2.10, 2.11, 2.16. After, 100 repetitions of Gaussian noise were added to each curve (standard deviation calculated as square of RSS). Per each repetition a new parameter estimate was obtained. Using the 100 estimates we obtained the standard deviation per each parameter of a specific model, corresponding to a specific voxel. Subsequently, the median value of all the standard deviations for a specific parameter was calculated. This value should represent the confidence interval for the estimate of that specific parameter.

3.2.4 Results

Figure 3.1 shows an example of FLASH data: in particular the T1-w image, the fat-suppressed image obtained subtracting the basal signal from 5th post contrast image and the ROI segmented by an expert radiologist.

Similarly, figure 3.2 shows an example of TWIST data.

The selected ROIs included 1276 and 322 voxels for the TWIST and the FLASH data respectively. Figure 3.3 shows the $C_p(t)$ fitting obtained using eq. 10 in TWIST data.

Figure 3.4 reports some examples of the fitting obtained for Tofts, Brix and ATH for TWIST data (a) and the fitting for Tofts and Brix for FLASH data (b). For the curve in (a) the ATH model resulted in a better fitting in comparison to both Tofts and Brix (for both BIC and AIC); for the curve in (b) the Brix model showed a better fitting in comparison to the Tofts one.

The main results of this study are summarized in figures 3.5, 3.6 and in table 3.2.

Figure 3.5 reports the results of the goodness-of-fit analysis for TWIST data. With reference to the part (a) the graphs must be interpreted as follows. Each point represents a whole $C_t(t)$: the value of the x- and y-coordinates are the values of the AIC for Tofts and ATH model respectively. The red line indicate equal goodness-of-fit (identity). The points

CHAPTER 3. DISTRIBUTED VERSUS COMPARTMENTAL TRACER KINETIC MODELS

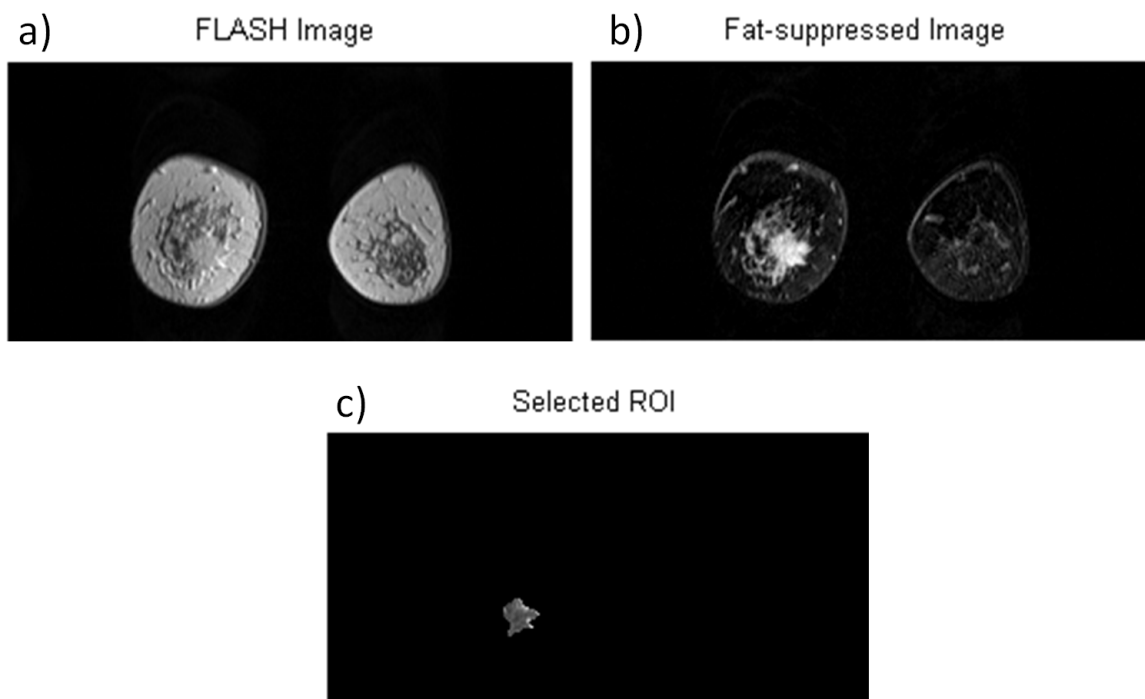


Figure 3.1: FLASH data: a) T1-w example image; b) Fat-suppressed image obtained subtracting the basal image from the 5th post contrast image, c) ROI selected by an expert radiologist.

CHAPTER 3. DISTRIBUTED VERSUS COMPARTMENTAL TRACER KINETIC MODELS

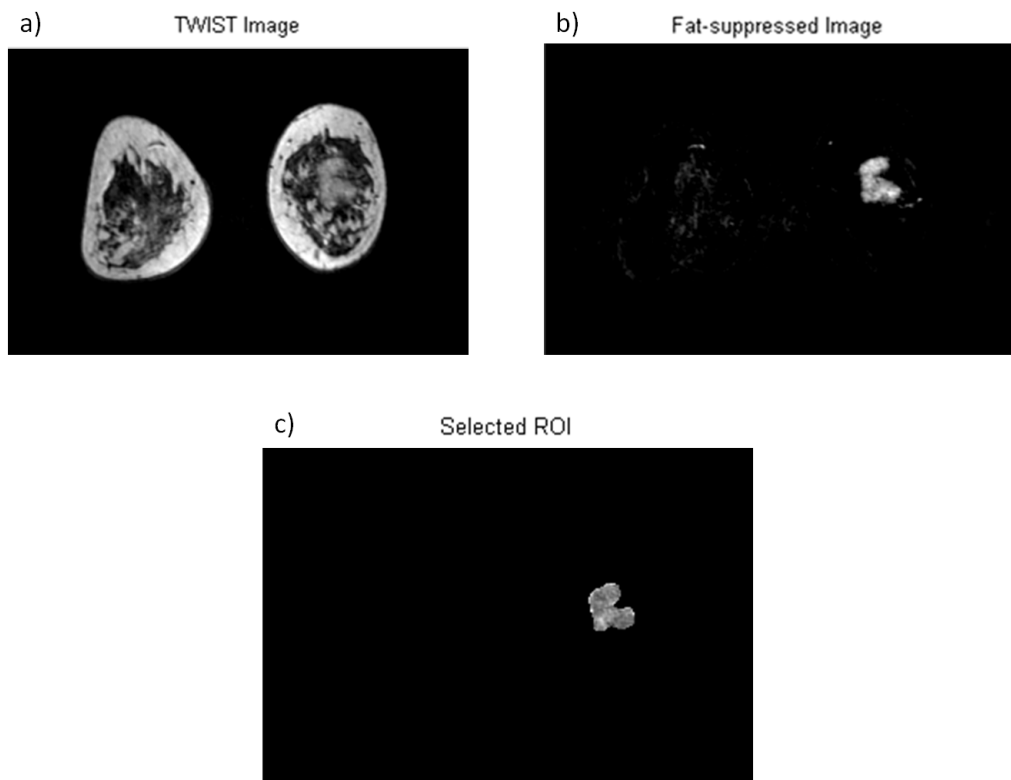


Figure 3.2: TWIST data: a) T1-w example image, b) Fat-suppressed image obtained subtracting the basal image from the 44th post contrast image, c) ROI selected by an expert radiologist

CHAPTER 3. DISTRIBUTED VERSUS COMPARTMENTAL TRACER KINETIC MODELS

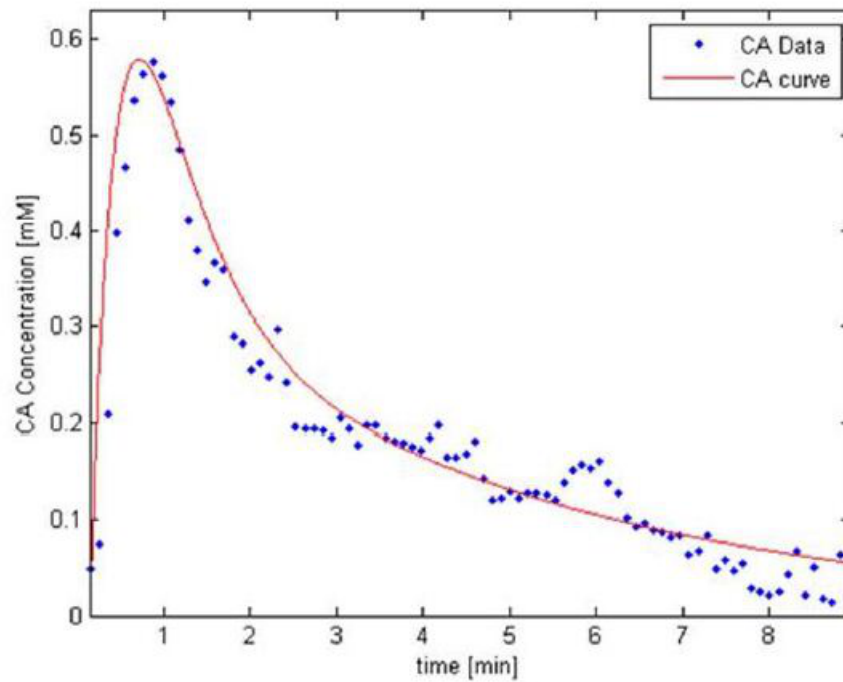


Figure 3.3: Manually selected AIF on TWIST data (blue dots) have been fitted by means of eq. 10 (red line).

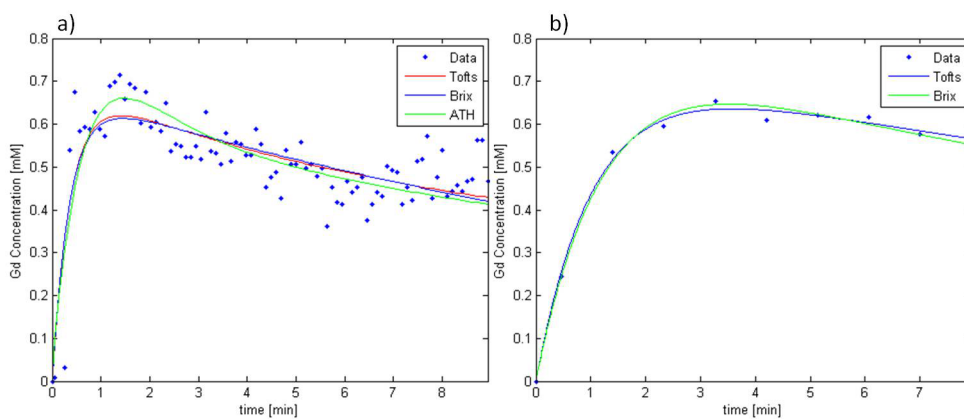


Figure 3.4: Example of data fitting. a) TWIST data (blue dots); Tofts model (red line); Brix model (blue line); ATH model (green line). b) FLASH data (blue dots); Tofts model (blue line); Brix model (green line).

CHAPTER 3. DISTRIBUTED VERSUS COMPARTMENTAL TRACER KINETIC MODELS

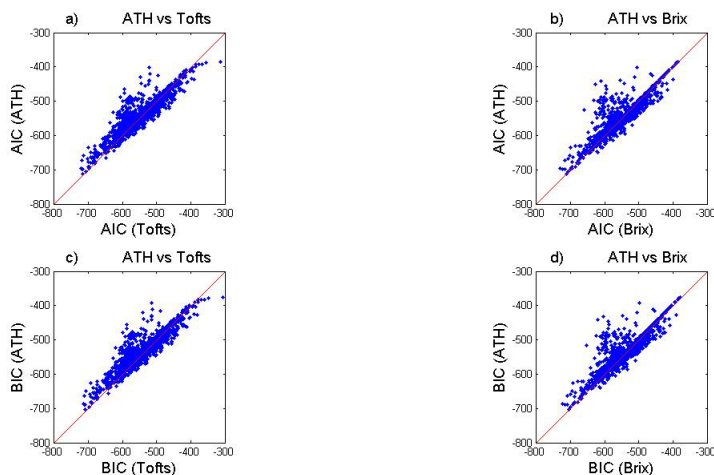


Figure 3.5: Goodness-of-fit for TWIST data. First row involves AIC: a) ATH versus Tofts; b) ATH versus Brix. Second row involves BIC: c) ATH versus Tofts; d) ATH versus Brix. Red lines indicate equal goodness of fit.

above the identity line denote cases in which the Tofts model gave better fit than ATH; points below lines denote cases in which ATH model gave better fit than Tofts. Similarly, figure 3.6 reports the results of RSS goodness-of-fit analysis for FLASH data. The interpretation of the figure is the same as figure 3.5.

Table 3.2 reports, in the case of TWIST data, per each couple of models and per each metric (RSS, BIC, AIC), the percentage of voxels for which the metric computed for one model is lower than the same metric computed for the other model. Note that, as regards the comparisons among ATH, Tofts and Brix models we considered only the metrics BIC and AIC because the number of model parameters is different; on the contrary, in the case of Brix vs Tofts comparison we considered only the RSS. In the case of FLASH data, the comparison between Brix and Tofts models showed that 77% of voxels had lower RSS for Brix than for Tofts.

In order to evaluate consistency among the parameters estimated with the different models in table 3.3 and 3.4 we reported the median of each parameter on TWIST data and on FLASH data respectively. Moreover, with the aim to evaluate the reliability of the estimates, we reported also the median value of the standard deviations that have been calculated on the repetitions of Monte Carlo simulation.

CHAPTER 3. DISTRIBUTED VERSUS COMPARTMENTAL TRACER KINETIC MODELS

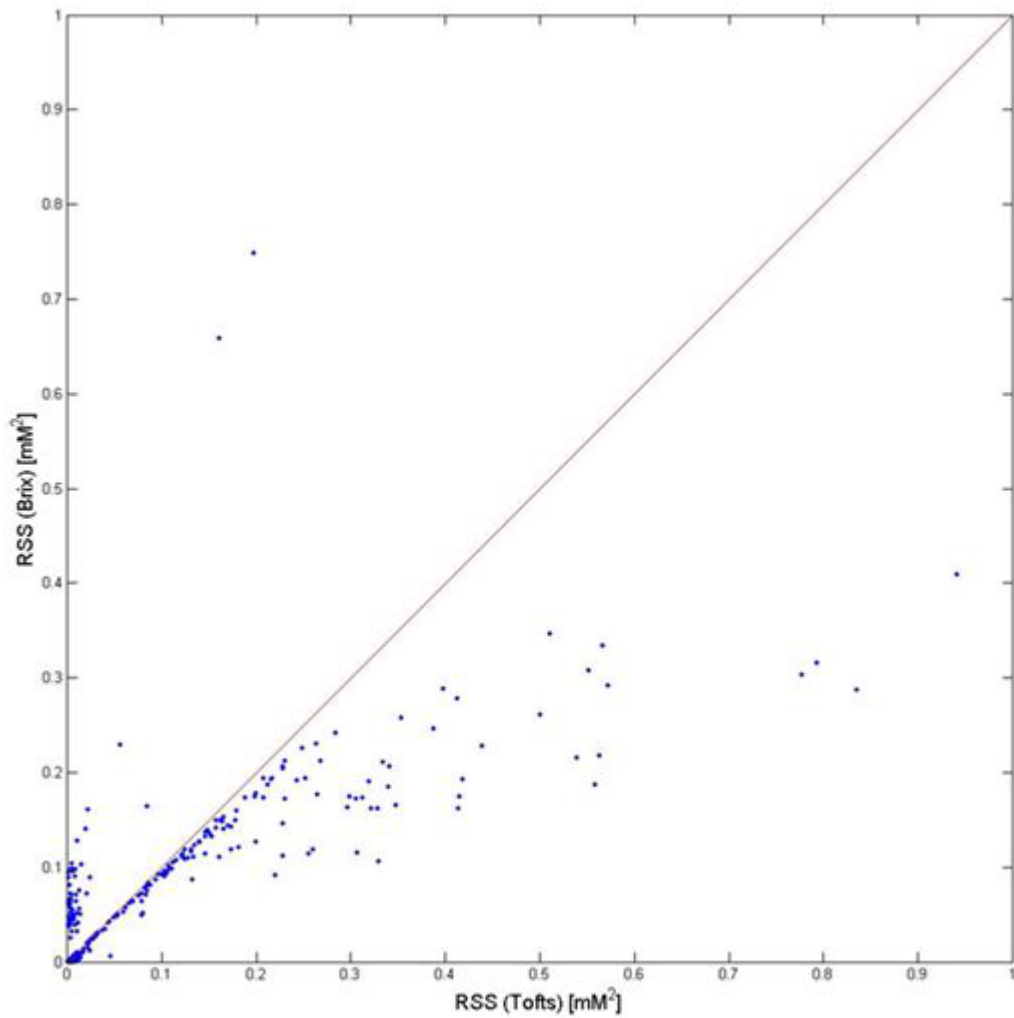


Figure 3.6: Goodness-of-fit for FLASH data. RSS values of Brix versus Tofts.

CHAPTER 3. DISTRIBUTED VERSUS COMPARTMENTAL TRACER KINETIC MODELS

Table 3.2: Goodness-of-fit measurements on TWIST and FLASH data. Per each metric the table reports the percentage of voxels showing better fit of one model versus the other.

	ATH vs Tofts [%]	ATH vs Brix [%]	Brix vs Tofts [%]
$R_1^2 < R_2^2$ (TWIST)			60
$BIC_1 < BIC_2$ (TWIST)	65	64	
$AIC_1 < AIC_2$ (TWIST)	59	56	
$R_1^2 < R_2^2$ (FLASH)			77

Table 3.3: Reliability of fit parameters on TWIST data. Per each model the table reports the median value of each parameter \pm the standard deviation median calculated on 100 repetitions of the Monte Carlo simulation.

	K_{trans}	k_{ep}	v_p	A	k_{el}
Tofts	0.005 \pm 0.000	0.013 \pm 0.000	0.097 \pm 0.023		
Brix		0.031 \pm 0.003		0.435 \pm 0.015	0.0002 \pm 0.000
ATH	0.004 \pm 0.000	0.070 \pm 0.004	0.591 \pm 0.155		

3.3 Discussion

In this study we found that on TWIST data ATH obtained better fits than Tofts (59% of voxels according to AIC and 65% according to BIC) and Brix (56 % of voxels according to AIC and 64% according to BIC) although the percentages were not huge. The estimated parameters obtained with the different models were comparable and fell within a physiological range.

As regards the reliability of the estimates it turned out that no model was capable of estimating all the parameters with reliability lower than about 10% and in some cases the reliability was very low. In the analysis of FLASH data we found that Brix obtained better fit than Tofts in 77% of voxels. Also in this case the estimated parameters were comparable, however the reliability of the estimates obtained using Brix was higher than Tofts.

The better performances of ATH were in part expected considering that this model is in principle more realistic and that $C_p(t)$ has been derived from real data. However, the improvement in terms of goodness-of-fit was not decisive, probably because of several reasons: first, the temporal resolution achievable in current clinical settings could be not yet sufficient to satisfy the requirements on the capillary mean transit time; second, the

CHAPTER 3. DISTRIBUTED VERSUS COMPARTMENTAL TRACER KINETIC MODELS

Table 3.4: Reliability of fit parameters on FLASH data. Per each model the table reports the median value of each parameter \pm the standard deviation median calculated on 100 repetitions of the Monte Carlo simulation.

	\bar{K}_{trans}	k_{ep}	v_p	A	k_{el}
Tofts	0.007 \pm 0.001	0.010 \pm 0.000	0.002 \pm 0.027		
Brix		0.016 \pm 0.004		0.678 \pm 0.074	0.001 \pm 0.000

typical signal-to-noise ratio achievable in current clinical setting could be not adequate to discriminate finer features of the CA time-course; finally, a major limitation of this study was the small number of subjects involved: this fact implies that the range of physiological parameters explored was limited, although they should be representative of important types of carcinomas, however it is worth to note that also in previous studies reporting comparison between models the number of subjects was small [51].

As regards the comparison between Brix and Tofts it should be noted that, even if they have the same number of parameters, Brix includes a mono-exponential $C_p(t)$ within the model itself while Tofts uses a bi-exponential AIF. This could explain the better performance of Brix with respect to Tofts on FLASH data: at low temporal resolution the mono-exponential AIF is sufficient to capture essential features of the data. On the contrary, on TWIST data Tofts seems to behave better than Brix although the difference is not huge: at high temporal resolution the mono-exponential model becomes not adequate and the bi-exponential approach is required.

As regards the comparison between Tofts and Brix models our results are in line with recent literature. Zwick et al. [39] reported the only comparison, to the best of our knowledge, on simulated DCE-MRI data and they concluded that Brix could be more robust than Tofts because it seems less affected by AIF variations.

As regards the comparison between DP and CC models conflicting results can be found in the literature. A theoretical study has been conducted by Muzic and Saidel [45] on PET receptors: they concluded that CC models outputs yielded good fits to all the DP model outputs and the values of the corresponding parameters were in close agreement, but given the temporal resolution typically available with PET, the use of a DP model had no advantage over a CC model for PET receptor quantification. Another study by Cheong et al. [51] reported a comparison of DP and

CHAPTER 3. DISTRIBUTED VERSUS COMPARTMENTAL TRACER KINETIC MODELS

CC models in DCE-Computerized Tomography (DCE-CT) of Intracranial Meningioma and concluded that DP models (including ATH) not only possess more realism theoretically but they were found to consistently give better fit than the CC models, although linear correlations were found between the kinetic parameters of the two models. Our results do not allow to propend towards one model or the other: although DP models have been argued on physical and physiological grounds, the question whether they can actually give better fit than CC models in breast DCE-MRI performed with current clinical settings, has not found yet a conclusive answer.

One important issue in comparing models is the use of an appropriate criterion. In this study we adopted three commonly used indices having a common basis (Kullback-Leibler divergence [62]) and are largely accepted in the statistical community. We found that the results obtained with different indices were in agreement with each other.

Chapter 4

Influence of parametrization on tracer kinetic modelling

Tracer kinetic modelling is commonly performed using Least-Squares algorithms. The convergence of such algorithms and the repeatability of the estimates is affected by the curvature of the model. An adequate choice of the parameterisation can reduce curvature thus improving parameter estimation. In this chapter we describe the curvature of the model as measures of non linearity we analyzed the influence of two parameterisations on the curvature of the widespread Tofts model.

This chapter contains work adapted from:

Fusco R, Sansone M, Petrillo M, Antonella Petrillo. Influence of parametrization on tracer kinetic modeling in DCE-MRI. *Journal of Medical and Biological Engineering*, Uncorrected Proof Available online 7 Sep 2012, doi: 10.5405/jmbe.1097.

4.1 Introduction

Estimation of tracer kinetic parameters of the widespread Tofts model [21] has been commonly performed using Least Squares (LS) algorithms [74, 59, 40, 70, 106, 107].

It turns out that the concept of expectation surface of the model is useful in order to describe some properties of the nonlinear least square estimate of the parameter. Given the observations $y_1 \dots y_N$ from the model $y_k = f(t_k, \theta_1 \dots \theta_p) + \epsilon_k$ it is possible to define the expectation surface or

the model manifold as the p -dimensional surface $\mathbf{y} = \eta(\theta)$ (parametrised with $\theta_1 \dots \theta_p$) embedded in the N -dimensional space of the data. If there was no noise on the data, the observed measures \mathbf{y} should lie on this surface. However, the presence of noise causes the measures \mathbf{y} to stay outside of this surface.

Bates and Watts have introduced the concept of curvature of the model manifold in 1980 [105, 5]. It is based on geometrical properties of the expectation surface of the model. The main idea is that if the expectation surface is locally planar then its curvature is zero; vice-versa the curvature is different from zero whereas the expectation surface is not planar. Local planarity is an essential condition for local approximation via Taylor expansion, that is typically used in the development of the nonlinear algorithms.

Ordinary nonlinear least-squares techniques are typically iterative, involving the update of parameter estimates until convergence criteria are reached. Nonlinearities (non-zero curvature) of the model in the neighborhood of the final estimate can affect the validity of statistical inferences (confidence intervals). Such inferences are typically based on linear approximations of the expectation surface close to the final estimate.

The degree of curvature in proximity of the final estimate is influenced by the specified expectation function, its parametrization, and the data to be fitted. Depending on the severity of the curvature of the model, this may result in inference intervals and regions that are asymmetric and distorted when compared to the corresponding linear estimation. It is of interest therefore, to determine the degree of this distortion as part of the model assessment and validation process. Bates and Watts have suggested some graphical approaches to address this problem.

The curvature of the model (see Fig. 4.1) manifold is made of two components: the intrinsic curvature, explained by the mathematical form of the model and the parameters-effect curvature, which is due to the specific parameters used. While the intrinsic curvature is not modifiable, parameters-effect curvature could be reduced if parameters could be properly chosen (see Fig. 4.1) [105, 5].

In Toft's model, two different parameterisations have been commonly used: either (K_{trans}, K_{ep}) [106, 107] or (K_{trans}, v_e) [74, 108]. To date, little guidance exist for optimal choice of parameterisation [5] and no guidelines have been proposed in the DCE-MRI scenario [33].

In this we analyzed the influence of this two parameterisations on the curvature.

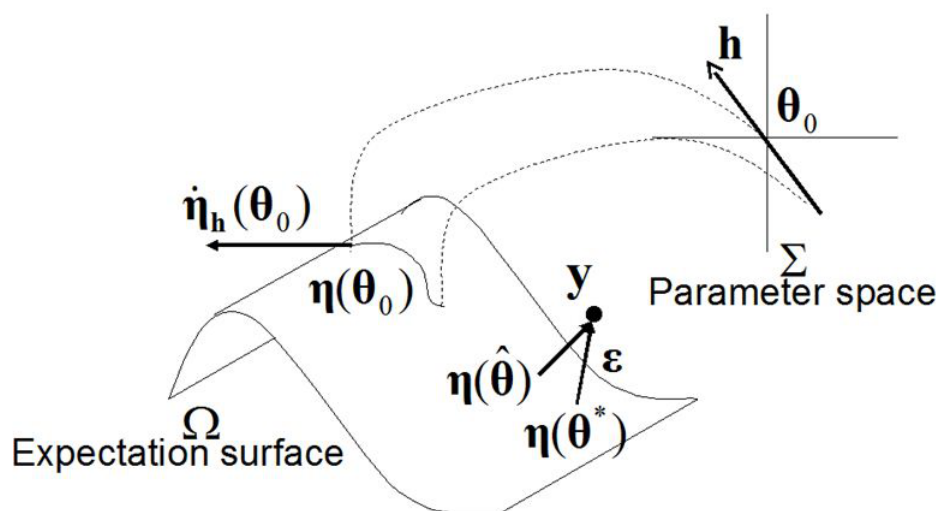


Figure 4.1: Concept of curvature. h is a direction in the parameter space Ω ; θ_0 is a reference point; $\eta(\theta_0)$ is the corresponding point on the expectation surface; $\dot{\eta}_h(\theta_0)$ is the vector tangent to the expectation surface; y are the measured data; ε is the measurement noise; θ^* is the true value of the parameters; $\hat{\theta}$ is the least squares estimate. In θ_0 there is high intrinsic curvature of the model manifold; in θ^* the intrinsic curvature is lower and here predominates parameters effect curvature.

4.2 Parameterisations of Toft' model

Combining equation (2.10) and equation (2.7) we obtain a parameterisation with (K_{trans}, K_{ep}, v_p) :

$$C_T(t, K_{trans}, k_{ep}, v_p) = v_p(A_B t e^{-\mu_B t} + A_G(e^{-\mu_G t} - e^{-\mu_B t})) + \frac{A_B K_{trans}}{k_{ep} - \mu_B} \left(t e^{-\mu_B t} - \frac{e^{-\mu_B t} - e^{-k_{ep} t}}{k_{ep} - \mu_B} \right) + A_G K_{trans} \left(\frac{e^{-\mu_G t} - e^{-k_{ep} t}}{k_{ep} - \mu_G} - \frac{e^{-\mu_B t} - e^{-k_{ep} t}}{k_{ep} - \mu_B} \right); \quad (4.1)$$

a parameterisation with (K_{trans}, v_e, v_p) can be obtained combining equation (??) and equation (4.1).

4.3 Model Curvature

We briefly recapitulate the main issues of the theory which is extensively dealt with by [5, 105].

Let us consider a model function $C_t(t, \Theta)$ with $\Theta = [\theta_1, \dots, \theta_p]$ model parameters; consider also a set of noisy measures $y_i = C_t(t_i, \Theta) + \epsilon_i$, with $i = 1, \dots, N$ ($T = t_{k+1} - t_k$ is the sampling period), where ϵ_i is random zero-mean noise. Let $\mu(\Theta) = [C_t(t_1, \Theta), \dots, C_t(t_N, \Theta)]$, then the measured data $\mathbf{y} = \mu(\Theta) + \epsilon$ (with $\mathbf{y} = [y_1, \dots, y_N]$ and $\epsilon = [\epsilon_1, \dots, \epsilon_N]$) belong to an N -dimensional space.

The p -dimensional surface $\Omega = \{\mu : \mu = \mu(\Theta), \Theta \in \Sigma\}$ contains all possible values of $E(\mathbf{y})$ and is called the *expectation surface* (Σ is the space of parameters).

Nonlinearity of the expectation surface in a specific point $\bar{\Theta}$ is commonly quantified by means of the maximum *intrinsic curvature* K_{max}^N and the maximum *parameters-effect curvature* K_{max}^T [105]:

$$K_{max}^N = \max_{\mathbf{h} \in \Sigma} \frac{\|\mathbf{h} \ddot{F}^N \mathbf{h}\|}{\|\mathbf{h} \dot{F}\|^2} \quad (4.2)$$

$$K_{max}^T = \max_{\mathbf{h} \in \Sigma} \frac{\|\mathbf{h} \ddot{F}^T \mathbf{h}\|}{\|\mathbf{h} \dot{F}\|^2} \quad (4.3)$$

where \dot{F} is the first derivative matrix, \ddot{F}^N and \ddot{F}^T are the projections of the second derivatives matrix \ddot{F} onto the planes tangent and orthogonal to Ω respectively; all the derivatives are evaluated at $\bar{\Theta}$.

Typically, the expectation surface can be considered approximately linear in a neighborhood of $\bar{\Theta}$ if [105]:

$$\max(K_{max}^T, K_{max}^N) < \frac{1}{2\sigma\sqrt{p \cdot F_{p, N-p}^\alpha}} = th(\sigma) \quad (4.4)$$

where σ is the noise standard deviation, $F_{p, N-p}^\alpha$ is the $(100-\alpha)$ -th percentile of the Fisher distribution with p and $N-p$ degrees of freedom, th stays for *threshold*.

4.4 Comparison of the two commonly used parameterisations on the Tofts' model curvature

The aim of this study was to analyze the influence of the two commonly used parameterisations on the curvature of the Tofts' model. The influence of the total acquisition time and of the sampling period has been also evaluated.

4.4.1 Simulations setup

We calculated both the intrinsic curvature and the parameters-effect curvature for several points in the parameters space and for several values of sampling period and total acquisition time. The calculation have been performed for both the parameterisations examined.

The parameter space was sampled as follows: K_{trans} ranged from 0.05 to 2 min^{-1} (step 0.1 min^{-1}); v_e ranged from 0.05 to 1 (step 0.05). These ranges should encompass the variety of physiological conditions found in both normal and diseased tissues [107, 59]. k_{ep} has been obtained from equation 2.3.

As regards v_p it is worth to notice that the first and second derivatives matrices in equations (4.2) and (4.3) *do not* depend on v_p . Accordingly, in our simulations we considered only K_{trans} , k_{ep} and v_e .

The sampling period T has been made vary from 5 to 20 s with steps of 5 s; The total acquisition time varied from 3 to 12 min, with steps of 3 min. Noise level σ varies from 0.01 to 0.1 mL^{-1} with step 0.01 mL^{-1} . The noise level on CA concentration actually present on DCE-MRI data depends on the specific pulse sequence utilized. Nonetheless it is desirable

to have an idea of the noise level on MR images corresponding to the noise used in these simulations. To convert the noise level in units related to the image noise we will refer to the formula for the signal intensity of the commonly used Spoiled Gradient Echo (eq. 2.19).

Using the standard error propagation theory we have that the error on signal, S , is proportional to the error in CA concentration, C ,: $\sigma_S = \frac{\partial S}{\partial C} \sigma_C$. As an example, using the following values: $r_1 = 4.5 \text{ mM}^{-1} \text{ s}^{-1}$; $T_{10} = 1000$ ms (typical range is from 500 to 1500 ms); $\alpha = 25^\circ$; $TE = 5$ ms; $TR = 10$ ms; $MO = 6000$ (from measurements at our institution), we have that $\sigma_s \approx 50$ intensity levels for $\sigma_C = 0.1$, while $\sigma_s \approx 5$ intensity levels for $\sigma_C = 0.01$.

For the AIF described by equation (2.7) the values reported by [109] were used: $A_B = 323 \text{ mL}^{-1} \text{ min}^{-1}$, $A_G = 1.07 \text{ mL}^{-1}$, $\mu_B = 20.2 \text{ min}^{-1}$, $\mu_G = 0.172 \text{ min}^{-1}$.

All numerical computations were performed in Matlab 2007a (The MathWorks, Massachusetts, USA) and curvature formulas were obtained using Mathematica 7.0 (Wolfram Research, Inc., Mathematica, Champaign, IL 2008).

4.4.2 Results

For ease of presentation all the results have been reported on the (K_{trans}, v_e) parameter space. Moreover, in order to simplify comparisons between figures 4.2, 4.3, 4.4 and 4.5, the colors used to represent the curvature under threshold (equation 4.4) are the same. For example, the curvatures below the threshold $th(0.1)$ ($\sigma = 0.1 \text{ mL}^{-1}$) have been represented using the color at the bottom of the color-bar. Of course, lower levels of noise correspond to higher thresholds: therefore, if K_{max}^N lays below $th(0.1)$ it will lay under $th(0.09)$ too, and so on.

Figure 4.2 shows the maximum intrinsic curvature K_{max}^N , in the case of total acquisition time of 6 min and sampling period of 5, 10, 15, 20 s. It is worth to notice that K_{max}^N increases up to $60 \text{ mL}^{-1} \text{ L}$ for small values of both K_{trans} and v_e . For total acquisition time of 3, 9 and 12 min a similar behavior has been observed.

Figure 4.3 shows that the maximum parameters-effect curvature for (K_{trans}, v_e) is lower than the curvature for (K_{trans}, k_{ep}) in a large area of the parameter space (total acquisition time: 6min; sampling period: 5, 10, 15, 20 s). However, the size of this area becomes smaller as the sampling time increases. The curvature for (K_{trans}, k_{ep}) ($K_{max}^{T, k_{ep}}$) is up to 30 times higher than the curvature for (K_{trans}, v_e) (K_{max}^{T, v_e}). Similar behavior has been observed for 3, 9 and 12 min total acquisition time.

CHAPTER 4. INFLUENCE OF PARAMETRIZATION ON TRACER KINETIC MODELLING

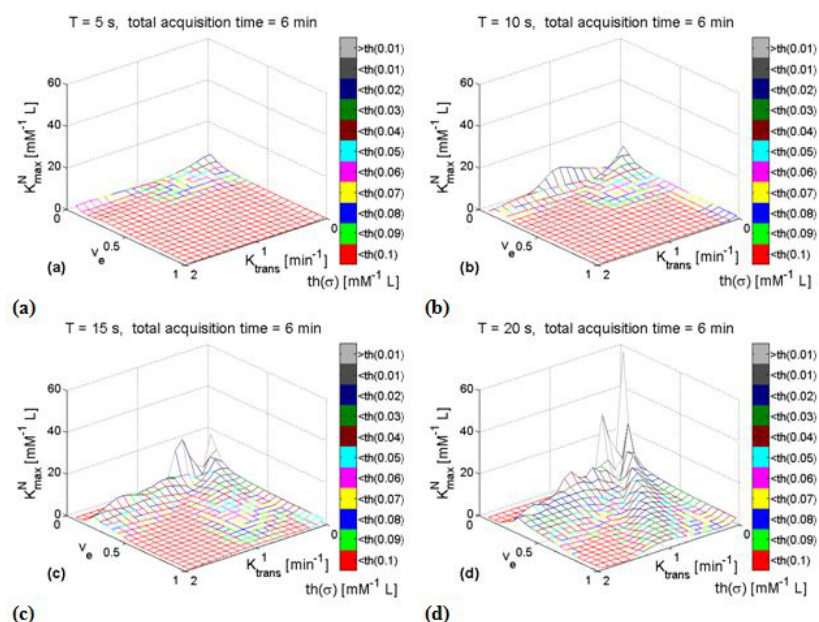


Figure 4.2: Maximum intrinsic curvature (K_{max}^N). Total acquisition time: 6 min. Sampling period T : (a) 5 s, (b) 10 s, (c) 15 s, (d) 20 s. The curvature less than $th(\sigma)$ is colored according to the colorbar.

Figure 4.4 shows the $max(K_{max}^N, K_{max}^T)$ for the parameterisation (K_{trans}, v_e) , in the case of total time 3, 6, 9 and 12 min respectively, $T = 5$ s. It is worth to notice that, while a great improvement is obtained from 3 to 6 min, little improvements can be seen for total time longer than 6 min. From this figure it can be inferred that the curvature is always above the threshold when $v_e < 0.4$: this is because v_e mainly affects Ct peak amplitude and therefore the signal to noise ratio. Similar behavior has been observed for (K_{trans}, k_{ep}) .

Figure 4.5 shows the $max(K_{max}^N, K_{max}^T)$ for the parameterisation (K_{trans}, v_e) , in the case of total time 6 min and $T = 10, 20$ s. As the sampling period increases the curvature becomes very large particularly for small values of v_e or K_{trans} . Similar behavior has been observed for (K_{trans}, k_{ep}) .

CHAPTER 4. INFLUENCE OF PARAMETRIZATION ON TRACER KINETIC MODELLING

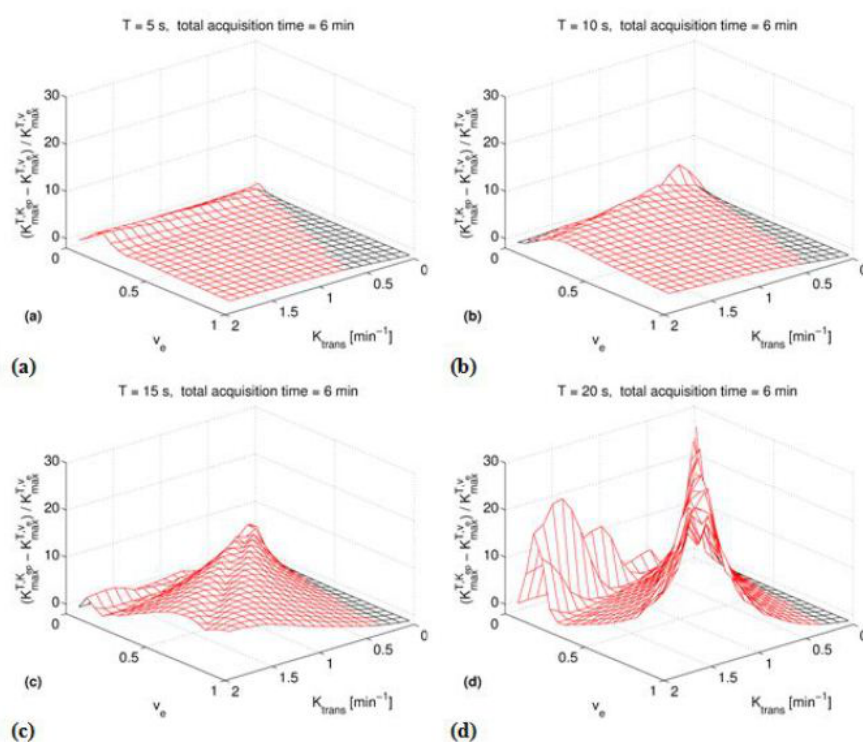


Figure 4.3: Comparison between the curvature of (K_{trans}, v_e) and (K_{trans}, k_{ep}) . On the Z axis $(K_{max}^{T,k_{ep}} - K_{max}^{T,v_e}) / K_{max}^{T,v_e}$ is reported. In the red area the curvature of the parameterisation (K_{trans}, v_e) is less than the curvature for (K_{trans}, k_{ep}) . Total acquisition time: 6 min. Sampling period T : (a) 5 s, (b) 10 s, (c) 15 s, (d) 20 s.

CHAPTER 4. INFLUENCE OF PARAMETRIZATION ON TRACER KINETIC MODELLING

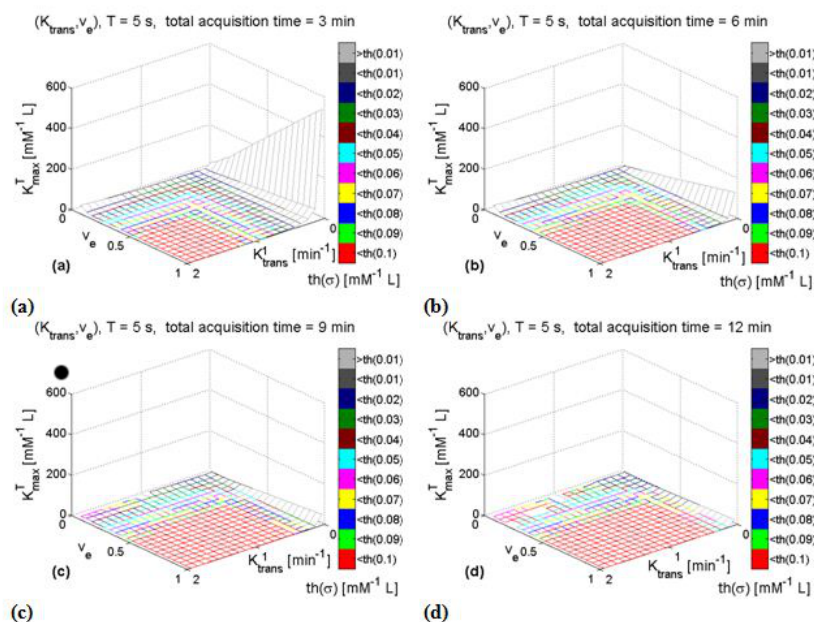


Figure 4.4: Parameters-effect curvature for the parameterisation (K_{trans}, v_e) . Analysis of the effect of the total acquisition time. Total acquisition time: (a) 3 min, (b) 6 min, (c) 9 min, (d) 12 min. Sampling period T : 5 s. Curvature values less than $th(\sigma)$ are colored according to the colorbar.

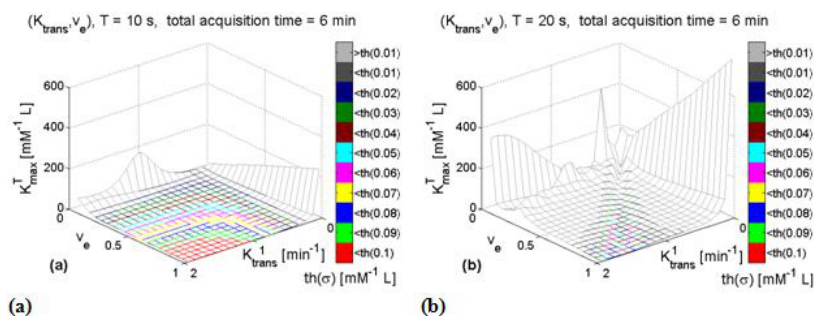


Figure 4.5: Parameters-effect curvature for the parameterisation (K_{trans}, v_e) . Analysis of the effect of the sampling period. Total acquisition time: 9 min. Sampling period T : (a) 10 s and 20 s (b). Curvature values less than $th(\sigma)$ are colored according to the colorbar.

4.5 Discussion

The results of this study can be summarized in two points. First, for both parameterisations the parameters-effect curvature is predominant over the intrinsic curvature and the curvature of the parameterisation (K_{trans}, v_e) is lower than that of (K_{trans}, K_{ep}) for a large range of parameters (the extension of this range is little affected by the sampling period).

Second, when considering (K_{trans}, v_e) only, the range of parameters having below-threshold curvature becomes wider as the total acquisition time increases (although little difference is observed for total acquisition time longer than 6 min). However, the opposite occurs when the sampling period increases.

Our analysis is in line with previous studies on the subject. A number of papers have tackled the issue of repeatability of parameter estimates for the Tofts' model in DCE-MRI scenario: [112] used a frequency analysis approach in order to establish optimal experimental conditions: however, in their analysis they used a bi-exponential AIF which is a too simplified model and their results could not be completely adequate for shorter sampling period; [110] used an error-propagation approach in order to analyze the influence of several factors comprising the T_{10} (T_1 of the tissue before contrast injection) and the flip angle: however, their analysis identifies only the 'instrumental' source of errors, and does not take into account modelling issues; [111] studied the influence of the sampling period for breast DCE-MRI, concluding that fast sampling is a strict requirement for accurate parameter estimation: they used the first derivative matrix \dot{F} as a tool of analysis, but they have not extended the analysis to the curvature of the model; [74] investigated the fitting failures due to the Levenberg-Marquardt fitting algorithm implemented in IDL (RSI Inc, Boulder, CO) and proposed a multiple starting points procedure in order to improve results: however, they used the parameterisation (K_{trans}, v_e) and did not investigate the other parameterisation (K_{trans}, K_{ep}).

It is worth to notice that our approach is complementary to the previous ones. In each of mentioned studies one single parameterisation has been chosen. The curvature properties of both parametrization have not been considered before. However, the analysis of curvature can shed light on the intrinsic properties of the Tofts' model and can suggest an optimal choice of the parameters.

As known, DCE-MRI guidelines [68] have proposed K_{trans} as primary endpoint because it seems directly related to perfusion of the tissues and

to permeability of the vessels; v_e has been proposed as a secondary end-point because it may reflect the cellular density. However, the parameterisation to be used has not been suggested. On the basis of our analysis, both the parameterisation used and the values of all the parameters should be reported, because the curvature, and consequently the accuracy of the estimates, depends on both parameters.

The importance of considering both parameters simultaneously has been evidenced also from a clinical point of view in a recent study [107] showing that for an effective separation between benign and malignant tumours in breast, K_{trans} only is not sufficient and that another parameter should be used. In fact, as noticed also by [113] tumor aggressiveness and response to therapy are influenced also by the EES fraction (v_e) of the malignant tissue.

In this regard, it is worth to mention that, often, clinical studies do not report neither the parameterisation they used, nor the values for all parameters.

Although the results of the present study apply mainly to LS fitting, our findings can shed light also on other methods for non-linear regression, because of the similarities among different approaches: in fact, Least Squares coincides with Maximum Likelihood method when gaussian noise is hypothesized; further, Bayesian methods coincide with Maximum Likelihood estimation when a uniform prior probability is assumed. Bayesian methods in DCE-MRI have been reported for example by [57]. Moreover, *ad hoc* reformulations of the Tofts' model are possible and were used by [110]. However, it should be noticed that the LS approach is the most widespread one, also because it is already implemented in most computational packages.

As the (K_{trans}, v_e) parameterisation has the lowest curvature in a larger area of the parameter space in comparison of (K_{trans}, k_{ep}) , it is suggested that the former parameterisation should be used in order to obtain an more reliable estimate of kinetic parameters. Moreover, when using (K_{trans}, v_e) , the range of parameters with under-threshold curvature becomes wider as the total acquisition time increases and as the sampling period decreases. Our study suggests that a total acquisition time greater than 6 min and a sampling period less than 10 seconds should be used.

However, our study indicates that none of the examined parameterisation can work well in the whole parameter space. This fact could suggest a new searching strategy to be included in Gauss-Newton based algorithms for nonlinear regression of the Tofts model in the DCE-MRI scenario: the evaluation of the local curvature can indicate which parameterisation to

*CHAPTER 4. INFLUENCE OF PARAMETRIZATION ON TRACER
KINETIC MODELLING*

use in order to obtain best results in terms of repeatability.

Chapter 5

Quantitative Approaches for simultaneous pixel classification and tracer kinetic modelling

In this chapter we propose a method to simultaneous segmentation simultaneous tracer kinetic modelling and pixel classification (enhancing and not enhancing pixel) of DCE-MRI studies.

This chapter contains work adapted from:

Sansone M, Fusco R, Petrillo A, Petrillo M, Bracale M. (2011). An expectation-maximisation approach for simultaneous pixel classification and tracer kinetic modelling in dynamic contrast enhanced-magnetic resonance imaging, *Med Biol Eng Comput* 49(4): 485-495.

5.1 Introduction

Automatic and objective analysis of DCE-MRI studies can greatly support the physician to obtain an accurate evaluation of tumour size, malignancy and perfusion in the surrounding tissues, which is essential in diagnosis, staging and clinical management of several kind of tumours and can support the assessment of new drugs.

Nonlinear modelling is computational demanding and the accuracy of the estimates can be affected by the signal-to noise ratio (SNR) and by the initial solutions, for this reason simultaneous tracer kinetic modelling

CHAPTER 5. QUANTITATIVE APPROACHES FOR SIMULTANEOUS PIXEL CLASSIFICATION AND TRACER KINETIC MODELLING

and pixel classification of DCE-MRI studies can improve the estimation accuracy by grouping together pixels having similar characteristics.

In the following we briefly discuss a few studies that, as far as the authors' knowledge, attempted to use spatial information for improving parameters estimation.

Schmid et al. [69] proposed a Bayesian approach combined with adaptive Gaussian Markov Random Fields (GMRF). The use of GMRF reduces the observed variability in local tumor regions while preserving sharp transitions between heterogeneous tissue boundaries. The use of Bayesian analysis combined with adaptive GMRF can provide improved convergence behavior and more consistent morphological and functional statistics but has two limitations: assumption must be made on the underlying distribution of kinetic parameters and computation time can be very long (about 8 h).

Kelm et al. [70] proposed a block version of the Iterated Conditional Modes (ICM) in order to reduce the long computational time of GMRF. Moreover in their approach, fewer assumptions on the underlying distribution are needed and the accuracy of the estimates is improved by using neighborhood information. Anyway their algorithm involves a few 'hyperparameters' such as the noise variance, the parameter weighting matrix and a spatial coupling factor whose estimation should be further investigated.

Xiaohua et al. [71] proposed a scheme for simultaneous segmentation and registration of breast DCE-MRI based on a Bayesian framework and MRF spatial priors. In this scheme only descriptive information from concentration-curves (such as slopes) have been used and tracer kinetic modeling is not considered.

Gong et al. [65] attempted the simultaneous segmentation and registration using texture information and spatial priors; anyway, they neglected tracer kinetic modelling.

In this study we propose an Expectation Maximisation (EM) [66] scheme for simultaneous pixel classification and tracer kinetic modelling of DCE-MRI studies.

The approach proposed is different from the previous ones. Our proposal is based on the consideration that pixels having similar characteristics can be identified within a ROI and can be used to calculate average tracer kinetic parameters, thus increasing the effective signal-to-noise ratio. To address the problem of non-linear estimation of kinetic parameters, we exploited the iterative nature of the EM algorithm and used the

Taylor expansion of the modelling equation. We developed the theoretical framework for the particular case of two classes and evaluated the performances of the algorithm by means of simulations. Moreover the results were compared to the theoretical Cramer-Rao (CR) [5] lower bounds and to the performances of the Levenberg-Marquardt (LM) algorithm [74], which is one of the most diffused non-linear-least-squares algorithms. Preliminary results on real data have been also reported.

5.2 Expectation Maximisation framework

Let us consider a DCE-MRI examination consisting of a single slice imaged at the time instants $t = 1 \dots T$. Let us denote by $y_n(t)$ the concentration of contrast medium in the voxel n at the time t , $n = 1 \dots N$. Moreover, let $\mathbf{y}_n = [y_n(1) \dots y_n(T)]^T$.

We assume that each pixel can belong to one of two classes: the class of pixels whose contrast medium concentration is constant (M_1) and the class of pixels whose concentration is varying according to the tracer kinetic model described by eq. (2.2) (M_2).

We propose to simultaneously identify the class of each pixel and to estimate the corresponding parameters K_{trans}, K_{ep} using an Expectation-Maximisation approach [66].

This approach is based on the concept of ‘missing data’ and ‘observable data’. For each pixel we observe \mathbf{y}_n . The missing data can be defined as a new variable $\mathbf{z}_n = [z_n^1, z_n^2]$ with $\mathbf{z}_n = [1, 0]$ if pixel $n \in M_1$ and $\mathbf{z}_n = [0, 1]$ if pixel $n \in M_2$. In this context the ‘complete data’ are $(\mathbf{y}_n, \mathbf{z}_n)$ with $n = 1 \dots N$. Moreover we assume that the two classes have unknown *a priori* probabilities π_1 and π_2 . Therefore we can define a vector $\Theta = [\pi_1, \pi_2, K_{trans}, K_{ep}]$ of parameters to be estimated.

We suppose there is a random gaussian noise superimposed on the \mathbf{y}_n with variance σ^2 and zero mean. The probability to observe \mathbf{y}_n given \mathbf{z}_n and a particular set of parameters Θ can be expressed as:

$$p(\mathbf{y}_n | \mathbf{z}_n, \Theta) = \begin{cases} \frac{1}{(2\pi\sigma^2)^{T/2}} \exp\left(-\frac{\|\mathbf{y}_n\|^2}{2\sigma^2}\right), n \in M_1 \\ \frac{1}{(2\pi\sigma^2)^{T/2}} \exp\left(-\frac{\|\mathbf{y}_n - \mathbf{C}(\Theta)\|^2}{2\sigma^2}\right), n \in M_2 \end{cases} \quad (5.1)$$

where we have defined $\mathbf{C}(\Theta) = [C_t(1) \dots C_t(T)]^T$ and $\|\cdot\|^2$ is the Euclidean norm.

Assuming that pixels are independent from each other the complete data log-likelihood is given by [66]:

CHAPTER 5. QUANTITATIVE APPROACHES FOR SIMULTANEOUS
PIXEL CLASSIFICATION AND TRACER KINETIC MODELLING

$$\begin{aligned}
 L(\Theta) &= \log \prod_{n=1}^N p(\mathbf{y}_n, \mathbf{z}_n | \Theta) = \\
 &= \log \prod_{n=1}^N \prod_{k=1}^2 (\pi_k \cdot p(\mathbf{y}_n | z_n^k = 1, \Theta))^{z_n^k}
 \end{aligned} \tag{5.2}$$

which can be expressed as:

$$L(\Theta) = \sum_{n=1}^N \sum_{k=1}^2 z_n^k \cdot [\log \pi_k + \log p(\mathbf{y}_n | z_n^k = 1, \Theta)] \tag{5.3}$$

The EM algorithm is subdivided in two steps [66] : E-step and M-step. In the E-step the log-likelihood must be averaged on the missing data, given the observed data:

$$\begin{aligned}
 E_{\Theta^m} [L(\Theta) | \mathbf{y}] &= \\
 &= \sum_{n,k} \tau_n^{m,k} [\log \pi_k + \log p(\mathbf{y}_n | z_n^k = 1, \Theta)]
 \end{aligned} \tag{5.4}$$

where $\Theta^m = [\pi_1^m, \pi_2^m, K_{trans}^m, K_{ep}^m]$ are the values of the parameters estimated at the m iteration and $\tau_n^{m,k} = p(z_n^k = 1 | \mathbf{y}_n, \Theta^m)$ (using Bayes theorem) :

$$\tau_n^{m,k} = \frac{\pi_k^m \cdot p(\mathbf{y}_n | z_n^k = 1, \Theta^m)}{\sum_{j=1}^2 \pi_j^m \cdot p(\mathbf{y}_n | z_n^j = 1, \Theta^m)} \tag{5.5}$$

In the M-step the ‘average’ likelihood must be maximized with respect to the parameters. Performing derivation with respect to the π_k parameters, and taking into account the condition $\pi_1 + \pi_2 = 1$, we have (using Lagrange multipliers) [66]:

$$\pi_k^{m+1} = \frac{\sum_{n=1}^N \tau_n^{m,k}}{N} \tag{5.6}$$

The estimation of K_{trans}^{m+1} and K_{ep}^{m+1} is more difficult because they appear in the expression of $C_t(t)$ in a non-linear manner. Typically, this problem is addressed via non-linear least-squares optimization. We, instead, use the iterative nature of EM algorithm and expand the tracer kinetic equation (2.2) in Taylor series with respect to the parameters obtaining:

CHAPTER 5. QUANTITATIVE APPROACHES FOR SIMULTANEOUS
PIXEL CLASSIFICATION AND TRACER KINETIC MODELLING

$$C_t(t, \Theta) = C^m(t) + A^m(t) \cdot \Delta K_{trans} + B^m(t) \cdot \Delta K_{ep} \quad (5.7)$$

where

$$\begin{aligned} A^m(t) &= \left. \frac{\partial C_t}{\partial K_{trans}} \right|_{\hat{K}_{trans}^m, \hat{K}_{ep}^m} \\ B^m(t) &= \left. \frac{\partial C_t}{\partial K_{ep}} \right|_{\hat{K}_{trans}^m, \hat{K}_{ep}^m} \\ C^m(t) &= C_t(t, \hat{K}_{trans}^m, \hat{K}_{ep}^m) \end{aligned} \quad (5.8)$$

Further, let:

$$\begin{aligned} \mathbf{A} &= [A^m(1) \dots A^m(T)]^T \\ \mathbf{B} &= [B^m(1) \dots B^m(T)]^T \\ \mathbf{C}_0 &= [C^m(1) \dots C^m(T)]^T \end{aligned} \quad (5.9)$$

so that we can write equation (5.7) as:

$$\mathbf{C}(\Theta) = \mathbf{C}_0 + \mathbf{A} \cdot \Delta K_{trans} + \mathbf{B} \cdot \Delta K_{ep} \quad (5.10)$$

Substituting equation (5.10) in the equation (5.1) and taking partial derivatives of (5.4) with respect to ΔK_{trans} and ΔK_{ep} and equating to zero we have:

$$\begin{aligned} \Delta K_{trans} &= \frac{1}{EC-D^2} \sum_n \tau_n^{m,2} (\mathbf{A}E - \mathbf{B}D)^T (\mathbf{y}_n - \mathbf{C}_0) \\ \Delta K_{ep} &= \frac{1}{EC-D^2} \sum_n \tau_n^{m,2} (\mathbf{B}C - \mathbf{A}D)^T (\mathbf{y}_n - \mathbf{C}_0) \end{aligned} \quad (5.11)$$

where we have denoted

$$\begin{aligned} C &= \sum_{n=1}^N \tau_n^{m,2} \cdot \mathbf{A}^T \cdot \mathbf{A} \\ D &= \sum_{n=1}^N \tau_n^{m,2} \cdot \mathbf{A}^T \cdot \mathbf{B} \\ E &= \sum_{n=1}^N \tau_n^{m,2} \cdot \mathbf{B}^T \cdot \mathbf{B} \end{aligned} \quad (5.12)$$

Therefore the estimation of parameters at the $m + 1$ iteration is:

$$\begin{aligned} \hat{K}_{trans}^{m+1} &= \hat{K}_{trans}^m + \Delta K_{trans} \\ \hat{K}_{ep}^{m+1} &= \hat{K}_{ep}^m + \Delta K_{ep} \end{aligned} \quad (5.13)$$

The condition for convergence can be specified as $\|\Theta^{m+1} - \Theta^m\|^2 < \delta$ where δ is a sufficiently small quantity arbitrarily chosen, or when the number of iteration exceeds a predefined threshold.

The equation (5.1) represents the probability that a specific pixel belongs to a certain class. Therefore we can substitute it by a more robust measure which enhances the difference between the two classes:

$$p(\mathbf{y}_n | \mathbf{z}_n, \Theta) = \begin{cases} \frac{1}{(2\pi\sigma^2)^{T/2}} \exp\left(-\frac{\|\mathbf{y}_n\|^2}{\|\mathbf{y}_n - \mathbf{C}(\Theta)\|^2}\right), n \in M_1 \\ \frac{1}{(2\pi\sigma^2)^{T/2}} \exp\left(-\frac{\|\mathbf{y}_n - \mathbf{C}(\Theta)\|^2}{\|\mathbf{y}_n\|^2}\right), n \in M_2 \end{cases} \quad (5.14)$$

It is possible to show that this expression does not modify equation (5.11) and all subsequent results.

5.3 Cramer-Rao Lower Bounds as errors measurement

Data are subjected to measurement errors and consequently the estimated parameters are affected by error $\tilde{\Theta} = \Theta^* - \hat{\Theta}$ where Θ^* is the true vector of parameters and $\hat{\Theta}$ is the estimated one.

It can be shown that any unbiased estimator $\hat{\Theta}$ of Θ^* has a covariance matrix which satisfies the following equation (Cramer-Rao lower bound) [5]:

$$Cov(\hat{\Theta}) > \mathbf{F}^{-1} \quad (5.15)$$

where the Fisher Information Matrix \mathbf{F}^{-1} is given by [5]:

$$\mathbf{F}^{-1} = \sigma^2 \cdot [\mathbf{S}^T \cdot \mathbf{S}]^{-1} \quad (5.16)$$

where σ^2 denotes the variance of the measurement noise and \mathbf{S} is the $T \times p$ sensitivity matrix (where p is the number of parameters to be estimated) evaluated at Θ^* :

$$\mathbf{S} = \left. \frac{\partial C_t}{\partial \Theta} \right|_{\Theta^*} \quad (5.17)$$

The diagonal elements of \mathbf{F}^{-1} , represent the minimum variance of the estimated parameters.

5.4 Simulation Setup

5.4.1 General characteristics of the simulated data

We examined the behavior of the proposed algorithm by means of several simulations. Firstly we assessed the SNR improvement due to pixel averaging, then we considered the effect of tumour heterogeneity and finally we analyzed a few alternative approaches.

All our simulations were referred to the characteristics of typical protocols in use for DCE-MRI examination. The time interval between two successive slice acquisitions has been set to 35 seconds and a total number of 11 acquisitions has been considered (the total time is about 6 min),

The bi-exponential AIF 2.9 was used [23, 59].

Moreover, we used K_{trans} and K_{ep} ranging in the intervals $[0.01, 1] \text{ min}^{-1}$ and $[0.025, 10] \text{ min}^{-1}$ respectively. These ranges encompass the variety of physiological conditions found in both normal and diseased tissues [59]. For each given couple (K_{trans}, K_{ep}) we simulated the tracer concentration curve using eq. (2.10) and lower bounds were calculated using eq. (5.15). For all simulations SNR ranged from $5dB$ to $20dB$. All calculations were conducted in Matlab (Mathworks inc.)

5.4.2 Assessment of SNR improvement

In order to have a point of reference for comparison, we evaluated the accuracy of the LM algorithm on a single-pixel basis. For each fixed value of (K_{trans}, K_{ep}) and SNR, 100 different realizations of random gaussian noise were added to the same simulated concentration-curves. For each noisy curve tracer kinetic parameters were estimated using the 'lsqcurvefit' function in the 'Matlab Optimisation Toolbox'. For each specific couple (K_{trans}, K_{ep}) the accuracy of LM was evaluated by means of the variance of the 100 estimates.

Secondly, we evaluated the performances of the EM algorithm. To this aim we constructed a 50×50 pixel image. Twenty-five pixels in the middle of the image were assigned to class M_2 (enhancement) while all the others to M_1 (no enhancement). For a given couple (K_{trans}, K_{ep}) a single concentration-curve was generated and was assigned to all the pixels of the 'enhancing' class, while the pixels of the 'not enhancing' class were assigned a zero-concentration curve. Moreover, 100 different realizations of random gaussian noise were added to the simulated data. The EM algorithm was applied to the noisy images and estimates of the kinetic

parameters of the M_2 class were computed. The variance of the 100 repetitions provided the accuracy of EM for a specific couple (K_{trans} , K_{ep}). Due to pixel averaging we expected an improved SNR and consequently an EM accuracy higher than the LM one. Moreover, the number of pixels correctly classified by EM has been evaluated.

In order to avoid the influence of the initial solutions, starting estimates for LM and EM were fixed at 10 % of the true value.

Lastly, we compared the performances of both algorithms to the CR lower bounds. Because of the specific number of pixels belonging to class M_2 , we expected the EM accuracy to be in agreement with CR lower bounds computed as if the noise variance was 25 times lower. Therefore, in this simulation, we used an SNR 5 times higher.

5.4.3 Sensitivity to initial estimates

Typically, an iterative algorithm is guaranteed to converge to a good solution if the initial estimate is close enough to the true value [5]. Therefore, we evaluated the variability of the final estimate of EM as a function of the starting estimate. As in the previous simulations we considered images corresponding to all the couples (K_{trans} , K_{ep}). The EM algorithm was applied to the image of each couple, varying the starting estimate k^0 of both K_{trans} , K_{ep} between -100 % to 200 % of the true value ($(k^0 - k^{true})/k^{true}$). The median percentage error of all the couples for a fixed percentage was calculated. The same procedure has been applied on a single-pixel basis to LM in order to have a point of reference for comparison.

5.4.4 Tumour heterogeneity and alternative descriptive measures

Tumors are characterized by an heterogeneous distribution of kinetic parameters [67]. Therefore, in order to have an idea of the behavior of EM on clinical data, we simulated heterogeneity-resembling data.

We generated a 50x50 pixels DCE-MR image having a tumor ROI of 10x10 pixels in the center. Random kinetic parameters were assigned to the pixels of the tumor ROI. A Fisher distribution $F(a, b)$ having $a = 70$ and $b = 700$ degrees of freedom was used. The degrees of freedom were chosen empirically just to resemble published distributions [67].

An interesting question is whether pixel classification and tracer kinetic modelling could be achieved using LM alone or by means of alter-

native approaches such as heuristic descriptors of tracer concentration curves.

A possible algorithm using LM alone could be the following: a) estimate tracer kinetic parameters on a pixel-by-pixel basis via nonlinear regression (starting estimates can be fixed to the center of the parameters space), b) set a threshold on the parameter histogram (by visual inspection) in order to subdivide the pixels in two classes, c) calculate the average parameters of the ‘enhancing’ class.

As an example of other descriptors we considered Initial Area Under Gadolinium Curve (IAUGC) which is a commonly used descriptor which was demonstrated to be strongly related to K_{trans} [18] In this case a possible algorithm for performing the classification could be the following: a) calculate IAUGC on a pixel-by-pixel basis, b) set a threshold on the IAUGC histogram to subdivide the pixels in two classes (by visual inspection) , c) perform averaging of pixels of the same class and then estimate parameters of the averaged curve (by means of LM, starting estimates fixed to the center of the parameters space).

Both alternatives were applied on heterogeneity-resembling data.

5.5 Real data acquisition

In order to give further insight into the behavior of EM on clinical data, we performed preliminary evaluation on one breast DCE-MRI study. DCE T1-weighted FLASH 3-D coronal images were acquired.

Two pre-contrast volumes were acquired with different flip angles (12 and 70 *degrees*) in order to obtain Gd quantification in accordance with the standard methods proposed in literature [68].

AIF was estimated by bi-exponential modelling of arterial flux with fixed parameters value from literature [21].

5.6 Results

5.6.1 Assessment of SNR improvement

Fig. 5.1 presents the results obtained with 5db SNR. In the case of 20 dB the results show similar trends with smaller errors. Standard deviations of kinetic parameters obtained with EM (Fig. 5.1e and 5.1f) were about 3 times the theoretical ones (CR) (Fig. 5.1a and 5.1b), while

the ones obtained with LM (Fig. 5.1c and 5.1d) were about 15 times the CR limit. The ratio between LM and EM accuracy was 5 as expected. All pixels were always correctly classified by the EM procedure. On average EM requires 8 iterations to converge.

5.6.2 Sensitivity to initial estimates

Fig. 5.2 reports results on sensitivity analysis. For LM the median percentage error of both K_{trans} and K_{ep} is confined between -2 and 2 %. When initial solution is below the true value LM has a tendency to underestimate it; the opposite occurs when initial solution is above the true value. This is in line with the above considerations concerning the initial solutions of iterative algorithms.

The figures 5.2 c) and d) report the same quantities in the case of EM. The median percentage error has very little variation around 0 %. Anyway, when the initial guess is in the range 100-200 % a few peaks appear. The peaks arise because the first-order approximation can be slightly inadequate for specific values of the parameters where the intrinsic curvature is high [5].

5.6.3 Tumour heterogeneity and alternative approaches

Fig. 5.3a shows the contrast agent concentration curve vs time for pixels of simulated image and the concentration curve corresponding to median kinetic parameters superimposed with red circles. Fig. 5.3b show the concentration curve corresponding to the EM estimated parameters, and the median curves obtained with LM and IAUGC. The true median curve (already drawn in fig 5.3) is also reported. The difference between true median parameters and the estimates of (K_{trans}, K_{ep}) were (2.9777, 6.5621) % for EM, (-3.4403, 4.7876) % for LM, (2.9013, 1.9709) % for IAUGC.

5.6.4 Preliminary results on real data

Fig. 5.4 shows the dynamic sequence of scans of a breast slice which was examined by two expert radiologists. They selected the region of interest (delimited by a yellow border) on the 6th dynamic scan. Fig. 5.3c shows the contrast agent concentration curves vs time for the pixels within the selected ROI. Fig. 5.5a shows the selected ROI on the original

CHAPTER 5. QUANTITATIVE APPROACHES FOR SIMULTANEOUS
PIXEL CLASSIFICATION AND TRACER KINETIC MODELLING

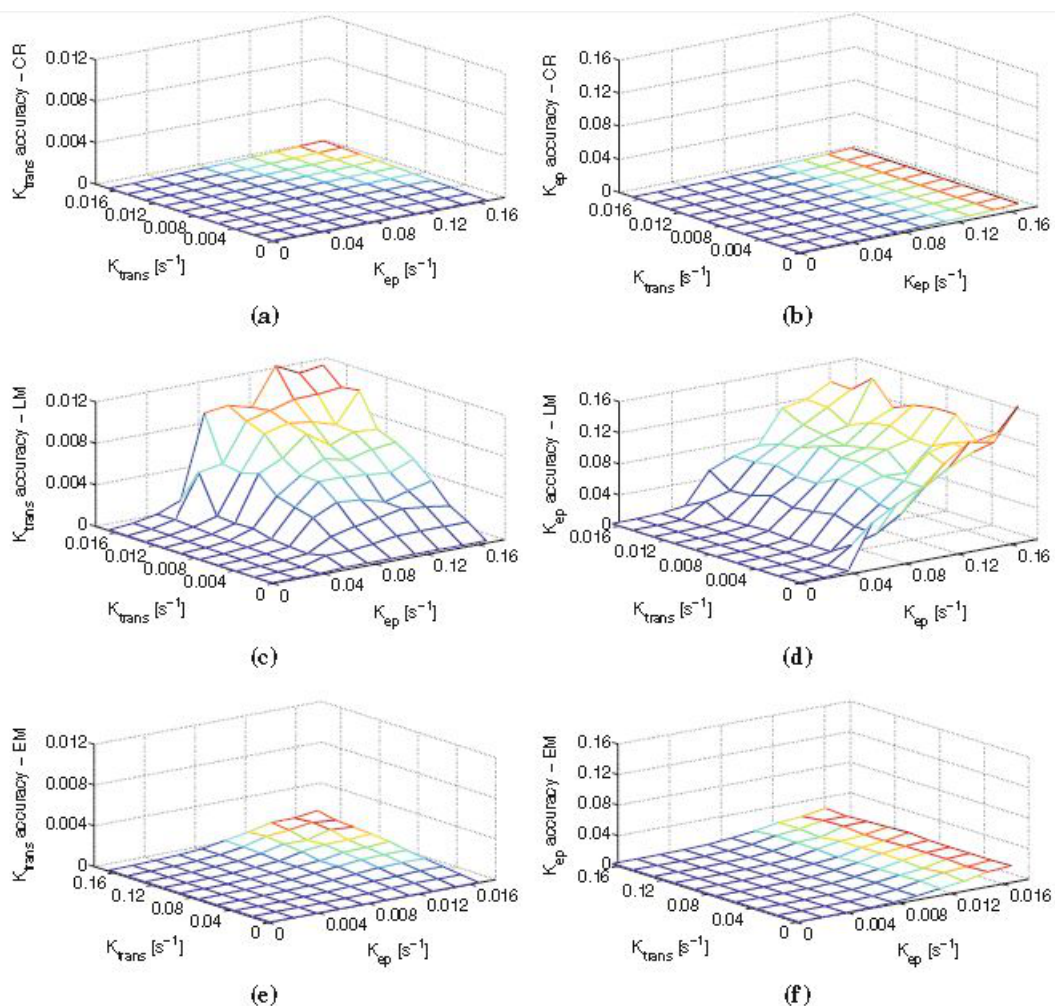


Figure 5.1: Accuracy of the estimation of kinetic parameters on simulated data: comparison among the theoretical Cramer-Rao (CR) lower bounds and the performances of Levenberg-Marquardt (LM) and Expectation-Maximisation (EM) algorithms. The figure reports the square root of variance [s^{-1}] for K_{trans} and K_{ep} in the case of CR (a) and (b), LM (c) and (d), EM (e) and (f). The ratio between LM and EM is about 5 as expected.

CHAPTER 5. QUANTITATIVE APPROACHES FOR SIMULTANEOUS
PIXEL CLASSIFICATION AND TRACER KINETIC MODELLING

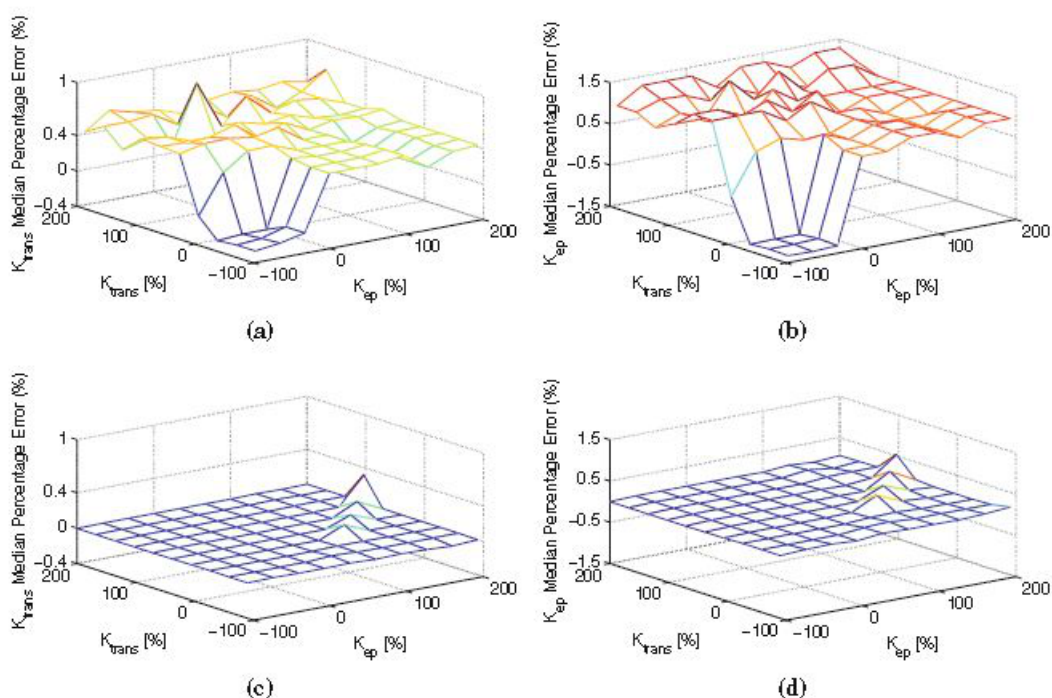


Figure 5.2: Sensitivity of the estimates to starting values. The median percentage error of K_{trans} and K_{ep} is reported as a function of the percentage distance between the initial estimate and the true value $(\frac{k^0 - k^{true}}{k^{true}} \cdot 100)$. Figures a) and b) report the results for LM. The median percentage error remains confined between about -1 and 1 %. When initial solution is below the true value LM has a tendency to underestimate it; the opposite occurs when initial solution is above the true value. The figures c) and d) report the same quantities in the case of EM. The median percentage error has very little variation around 0 %. When the initial guess is almost double than the true value, a few peaks appear.

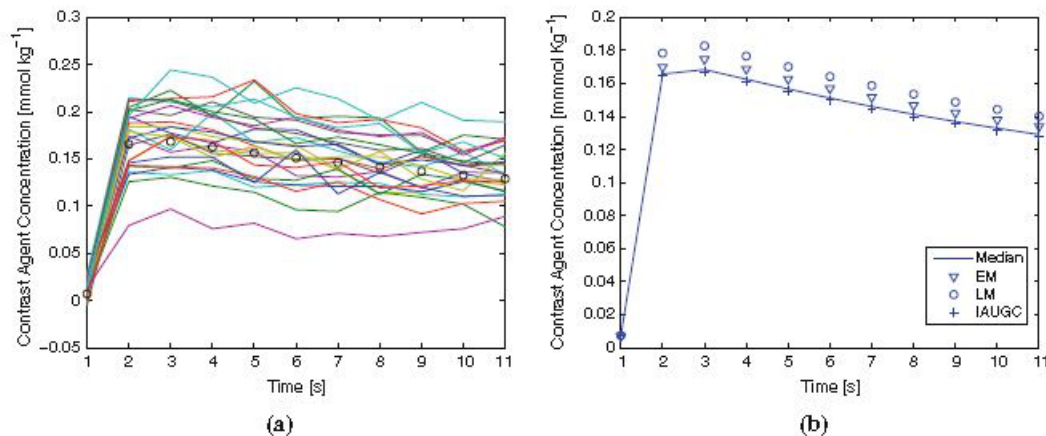


Figure 5.3: a) Effect of tumor heterogeneity: contrast medium concentration curves for pixels of simulated image. The curve corresponding to median kinetic parameters is reported using circles. b) Alternative approaches: comparison among the median concentration curve (already reported in fig. 5.3a) and LM, EM, IAUGC curves.

image; Fig. 5.5b shows EM pixel classification; Fig. 5.5c and 5.5d shows the map of probability to belong to the ‘not enhancing’ and ‘enhancing’ class respectively. Fig. 5.5e and 5.5f shows the maps of K_{trans} and K_{ep} respectively, calculated using LM.

5.7 Discussion

Aim of this work was to assess, by means of simulations, the performances of an Expectation-Maximisation scheme for simultaneous pixel classification and tracer kinetic modelling of DCE-MRI studies. The proposed EM scheme was expected to provide average kinetic parameters because pixels having high probability to belong to the same class are used to estimate the parameters of that class, thus increasing the effective signal-to-noise ratio with respect to the standard pixel-by-pixel approach in which pixels are examined separately. This approach is supported, from a clinical point of view, by recent literature (see for example [75]) reporting that although detailed evaluation of tumour heterogeneity is of help in tumour management, average measures performed on ROI opportunely selected are strongly correlated to measurements of heterogeneity,

*CHAPTER 5. QUANTITATIVE APPROACHES FOR SIMULTANEOUS
PIXEL CLASSIFICATION AND TRACER KINETIC MODELLING*

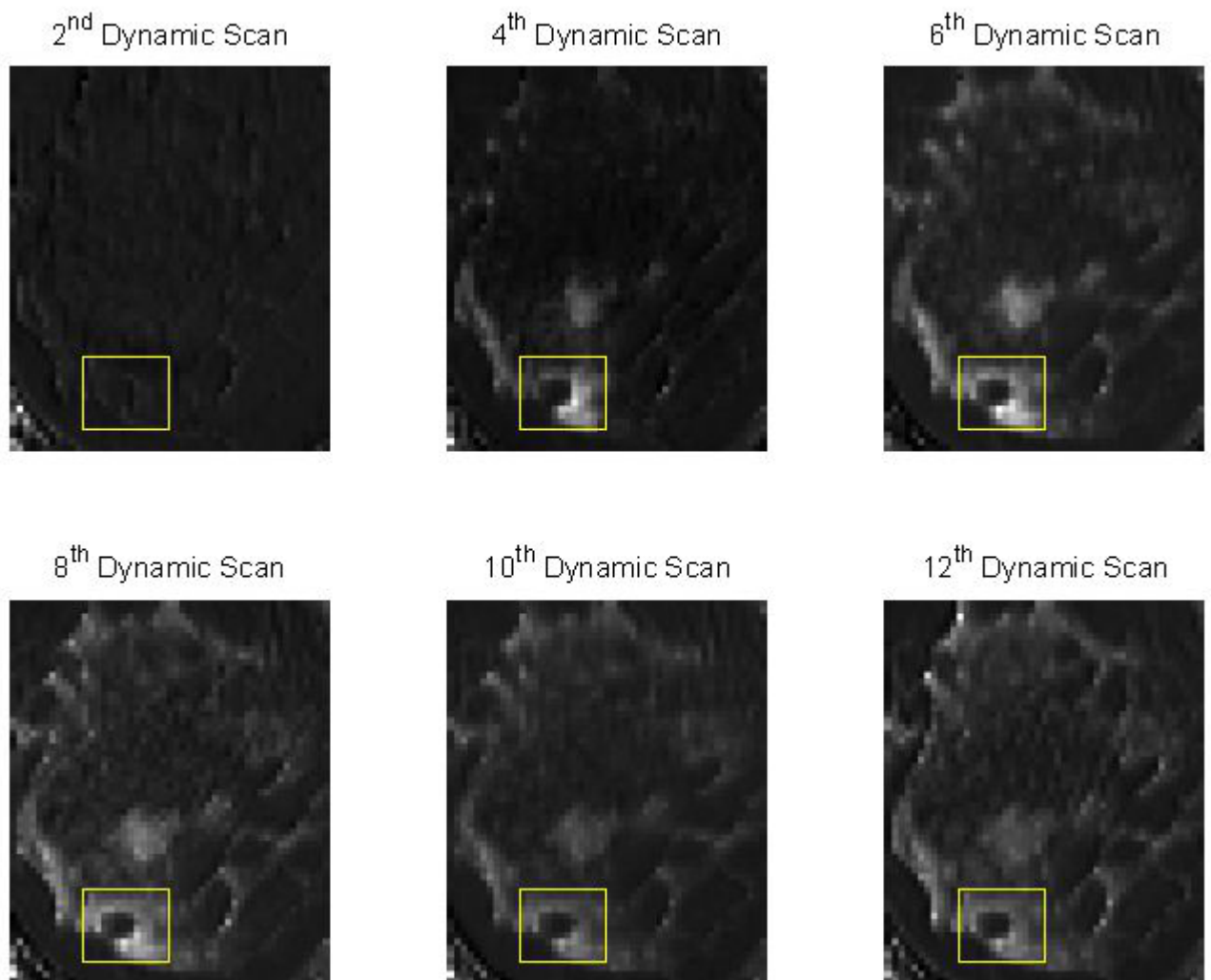


Figure 5.4: Real data DCE-MRI: see text for sequence parameters. The time interval between two successive scan is about 35 s. The yellow border delimitates the investigated ROI.

CHAPTER 5. QUANTITATIVE APPROACHES FOR SIMULTANEOUS
PIXEL CLASSIFICATION AND TRACER KINETIC MODELLING

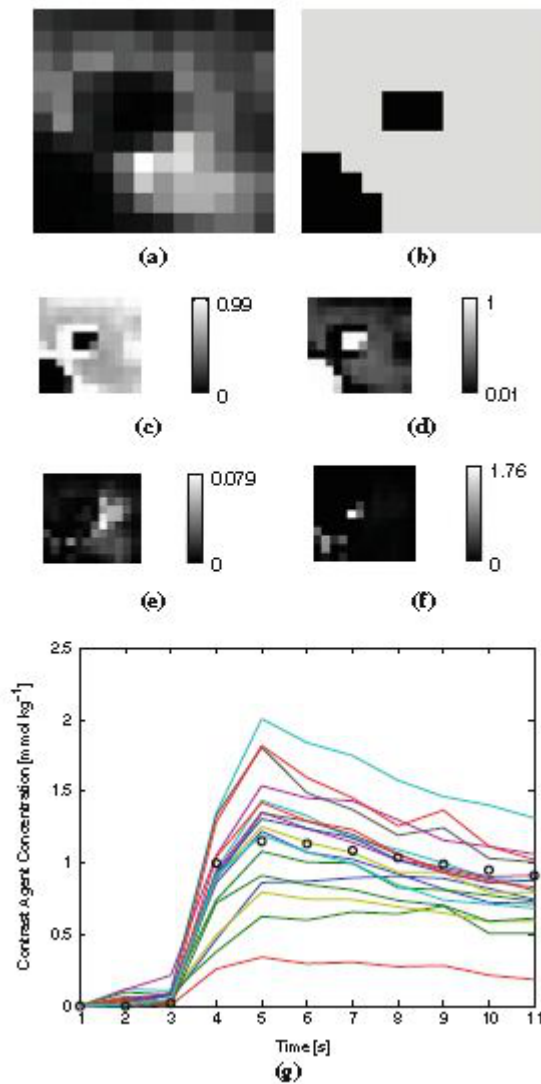


Figure 5.5: Analysis of the ROI shown in Fig. 5.4. a) Original image acquired at the 6th dynamic scan. b) EM classification: white pixels belong to the ‘enhancing’ class. c) Probability to belong to the ‘enhancing’ class. White pixels have higher probability. d) Probability to belong to the ‘not enhancing’ class. White pixels have higher probability. e) K_{trans} map. f) K_{ep} map. g) Concentration curves for the ROI in Fig. 5.4.

CHAPTER 5. QUANTITATIVE APPROACHES FOR SIMULTANEOUS PIXEL CLASSIFICATION AND TRACER KINETIC MODELLING

and can be used as an indicator for characterizing a whole tumour.

Simulation results were compared to the theoretical limits imposed by Cramer-Rao theorem and to the performances of the Levenberg-Marquardt algorithm applied on a pixel-by-pixel basis. The comparison indicates that the EM algorithm can approach the theoretical lower bounds and that the effective signal-to-noise ratio is increased as expected. Anyway, we should clarify that our objective was not an exhaustive evaluation of the Levenberg-Marquardt algorithm which has been widely dealt with in other studies [74, 5].

From these results it can be deduced that our approach can effectively increase SNR if it can be assumed that pixels belonging to the ‘enhancing’ region have similar tracer kinetic parameters. When this hypothesis is satisfied, our approach can provide a good estimate of ‘average’ kinetic parameters.

Anyway, when this hypothesis is not fully satisfied because of the intrinsic heterogeneity of tumors [67, 75] our method can still provide an overall characterization of the angiogenic activity of the whole tumour, as was suggested by our simulations.

As far as alternative approaches are concerned, our simulations suggest that comparable results can be obtained using EM, LM alone or IAUGC. Anyway, pixel-by-pixel LM requires as many nonlinear curve fitting as the size of the ROI and in order to yield a reliable estimate at least 5 estimations for each pixel should be repeated with different initial guesses [74], thus increasing the computation time without improvement in the SNR. The IAUGC approach seems to be more appealing than LM alone because IAUGC is fast to compute and only one final nonlinear regression is required. Anyway, histogram based classification renews the problem of model-free clustering.

Preliminary results on real data show that EM provides a reasonable estimate of the ‘average’ parameters. While the EM method is mainly directed to give overall information, the capability to provide a probability map (i.e. the distance of a specific concentration curve from the estimated ‘average’ curve) indicates that information about heterogeneity is not lost and can be further evaluated. Our future studies will be directed to assess this issue from a clinical point of view.

A few considerations about our hypothesis are in order.

First-order expansion of the model function (expectation surface) is a common practice in the literature concerning non-linear regression, where it is referred to as the Gauss-Newton approach [5]. In our case

CHAPTER 5. QUANTITATIVE APPROACHES FOR SIMULTANEOUS PIXEL CLASSIFICATION AND TRACER KINETIC MODELLING

this approximation can be further justified by the following two considerations. Firstly, the averaged log-likelihood has the effect to increase the SNR, thus the actual region of validity of the first-order expansion is enlarged. Moreover, two successive parameters estimates are expected to be not very far from each other: in fact, in the E-step of the (m+1) iteration, pixels closer to the curve obtained with parameters from the (m) iteration will obtain greater weights. Therefore, in the M-step of (m+1) iteration the average likelihood will be dominated by pixels that were already close to the (m) iteration. Anyway, the peaks in Fig. 5.2 are due to the combined effect of the intrinsic curvature of the non-linear model (see [5]) in specific regions of the parameter space and the consequently limited validity of the first-order expansion in those regions: in view of this consideration our future efforts will be directed to include some form of Hessian analysis.

Pixel independence is not only a convenient assumption for mathematical tractability. Of course, in real studies pixels are not completely independent from each other, and it is intuitively expected that adjacent pixels have similar parameters. Anyway, as above mentioned, numerous studies demonstrate tumour heterogeneity (see for example [67, 75]), suggesting that the hypothesis of independence is not completely unjustified. Moreover, it should be underlined that even studies using some form of spatial constraints [69, 70], explicitly observe that spatial priors should preserve sharp transition just because of tumour heterogeneity.

In this study we developed the EM framework assuming only two classes. This is a simplifying assumption which is equivalent to subdivide the tissues in low-enhancing and high-enhancing. The first class can be associated to regions without a vascular bed and to regions with low angiogenic activity. The second class can be associated to the anatomical regions in which the angiogenic activity is high and to regions with high vasculature. In the scenario we have in mind, the algorithm should be used by an expert radiologist for evaluation of suspicious lesions: therefore, we expect the radiologist to select an opportune ROI which will be evaluated by EM in order to supply an overall estimate of kinetic parameters. Strongly vascularized structures are expected to be excluded from the selected ROI, and regions without a vascular bed (not-enhancing at all), which are not amenable to a tracer kinetic modelling, are considered as having zero K_{trans} .

As far as computational issues are concerned, it should be noted that more sophisticated approaches require very large computation times while our scheme is able to converge in few iterations: therefore we think

*CHAPTER 5. QUANTITATIVE APPROACHES FOR SIMULTANEOUS
PIXEL CLASSIFICATION AND TRACER KINETIC MODELLING*

it could be used in combination with other methodologies for a quick detection and evaluation of suspicious regions, followed by a more accurate analysis.

Chapter 6

Segmentation and classification using machine learning approach

In this and in the next chapter we will discuss and explain the use of machine learning for automatic segmentation and classification of breast lesion. In this study we used pattern recognition techniques in order to assess the accuracy of automated methods for the segmentation and the classification of breast lesions using several features. As a first step, we evaluated the discriminative power of morphological, textural and dynamic semi-quantitative features computed from the time intensity curve. Subsequently, we evaluated dynamic features extracted from more sophisticated models (quantitative analysis), as well as the ability of multi-classification systems that combine the results of classifiers trained separately with different features.

This chapter contains work adapted from:

Sansone M, Aprile F, Fusco R, Petrillo A, Petrillo M, Siani A, Bracale U. Reference based time intensity curves quantification in DCE-MRI monitoring of rectal cancer. Proceedings of 11th World Congress on Medical Physics and Biomedical Engineering, September 7-12, 2009 in Munich, Germany

R. Fusco et al. Selection of suspicious ROIs in breast dce-mri. Lecture Notes in Computer Science, 6978:48-57, 2011.

R. Fusco, M. Sansone, C. Sansone, A. Rotondo, A. Petrillo. Segmentation and classification of breast lesions using dynamic and textural features in Dynamic Contrast Enhanced-Magnetic Resonance Imaging. Computer-Based Medical Systems (CBMS), 2012 25th International Symposium on, June 20-22 Rome-Italy, 2012.

6.1 Introduction

Lesion segmentation is the first critical step in breast diagnosis. As a matter of fact, manual segmentation is tedious, time consuming and suffers from inter- and intra-operator variability and there exists the possibility that suspicious regions of enhancement may be overlooked [84].

A number of automatic lesion segmentation approaches [40, 89] have recently been proposed to address the above mentioned limitations. Very simple approaches [91] used only pixel intensities for region of interest (ROI) selection considering only static features without taking advantage of the whole dynamic information. The combined use of region growing and some shape-based features have also been investigated [84] together with lesion segmentation by means of fuzzy c-means using dynamic features [77].

As regards the classification of breast lesions, the characterization as benign or malignant on the basis of MR imaging remains a challenge. There is still a debate in the literature regarding the interpretation strategies and the relative importance of textural and dynamic features in the discrimination of benign from malignant lesions. Malignant and benign lesions behave differently in terms of temporal enhancement: malignant lesions usually show early strong enhancement with rapid excretion of contrast medium, whereas benign lesions typically show a slow increase followed by persistent enhancement [89]. Heterogeneity of the ROI can be another useful indicator: heterogenous and peripheral enhancements are important evidence of malignancy, whereas homogenous enhancements are often associated with benignancy.

Recently, attempts have been made to automatically classify breast lesions in terms of dynamic contrast enhancement. Chen et al. [76] searched for the hot spot and analyzed its dynamical features. Meinel et al.[86] performed a systematic statistical analysis to select an optimal set of dynamic features to achieve the highest diagnostic accuracy.

Fewer investigators have attempted to integrate spatial and temporal features [88] and fewer researcher have proposed a completely automatic

method for segmentation and classification breast lesions.

We propose an approach, based on Multi Layer Perceptron classification of dynamic and textural features, for segmentation of suspicious ROIs within the breast and subsequent classification as malignant or benign lesions.

The considered features were dynamic, spatial-temporal and textural derived from DCE-MRI data. In particular, 98 dynamic features, 60 textural features and 72 spatio-temporal features were considered. Feature selection was performed in order to individuate the best set of features per each classifier. Complex feature extraction algorithms (e.g. PCA) have not been considered in order to preserve the physiological meaning of the features.

20 women (average age 46 years) with benign or malignant lesions, histopathologically proven, were enrolled: 10 cases were malignant and 10 benign. The lesions were subdivided in two sets: the training-set was composed by 5 benign lesions and 5 malignant lesions while the test-set was composed by 5 benign lesions and 5 malignant lesions.

The performance of lesion segmentation have been evaluated with respect to manual segmentation provided by an expert radiologist. Results of lesion classification were compared to histological findings.

6.2 Methods

6.2.1 ROI segmentation

Manual ROI selection slice by slice was performed by an expert radiologist comparing morphological (Turbo spin echo T2- and T1 weighted images) and functional imaging (DCE T1 weighted images) based on the fat-suppressed image obtained subtracting the basal pre-contrast image from the 5-th post-contrast image. Per each patient all the slices including the lesion have been used. The segmentation was performed with OsiriX v.3.8.1 (fig. 6.1).

In **automatic** selection the first step was the overall breast mask segmentation by means of Otsu thresholding of the parametric map obtained considering the pixel-by-pixel SOD followed by hole-filling and leakage removal by means of morphological operators [79].

Successively, **automatic** VOI segmentation has been obtained with pixel by pixel classification of dynamic features (MLP).

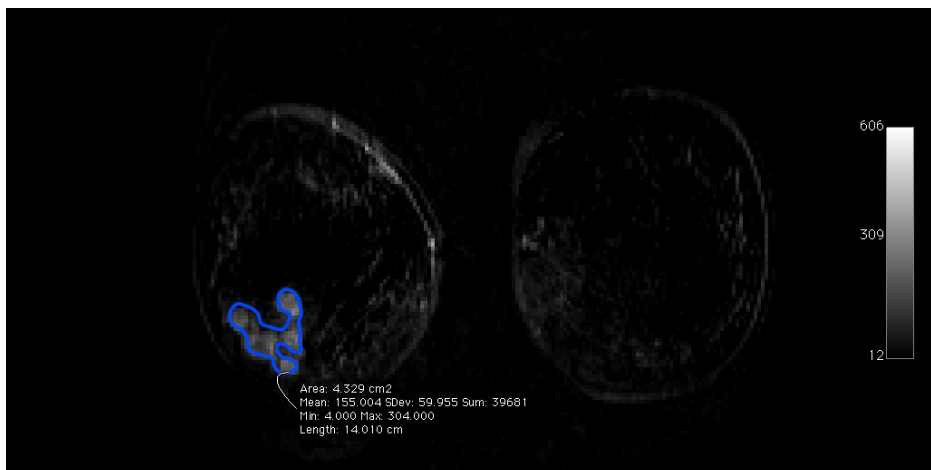


Figure 6.1: Manual Segmentation

The dynamic features: sum of intensities difference (SOD), basal signal and relative enhancement slope calculated pixel by pixel of breast mask were used as input of a Multilayer Perceptron classifier (learning rate = 0.3, momentum = 0.2, and a training time of 100 epochs). The output of the classifier identified the pixels as *suspicious* or *not suspicious*. The union of suspicious pixels formed the automatic region of interest. The evaluation of the performance has been obtained in comparison to manual segmentation.

6.2.2 Automatic ROI Classification

Each pixel within the ROI has been further classified as *benign* or *malignant*. The input ROI of classification is the manual segmentation ROI by the expert radiologist. A new feature selection and classifier training, different from the previous step has been performed. The classifier was trained considering dynamic, spatial-temporal and textural features separately and considering them as unique subset of feature. The ROI was classified as malignant when a number of pixels superior to 50% was classified as malignant. The evaluation of performance was obtained in comparison to histological classification.

6.2.3 Features

A survey of the literature has evidenced a number of features which have been grouped in a few main categories: for dynamic features were considered area, maximum intensity ratio, relative enhancement, relative enhancement slope, basal signal, perfusion index, sum of intensities difference (SOD), wash-in, wash-out, time to peak [80, 82]; for spatial-temporal features were considered Discrete Fourier Transform coefficient map, margin gradient, radial gradient, relative enhancement, time to peak of relative enhancement variance, wash-in, wash-out [90, 92], and for textural feature were considered average, variance, kurtosis, skewness, angular moment, contrast, correlation, entropy [94], dissimilarity [82].

6.2.4 Classifier

We trained one classifier that represent typical implementations of machine learning algorithms: a Multi Layer Perceptron (MLP) neural network classifier.

The choice of this classifier was based on a survey of the literature that has evidenced this classifier as the most frequently used in breast DCE-MRI data analysis and by a preliminary analysis among different classifiers (Decision Tree, Bayesian Classifier and Support Vector Machine)[91, 89, 93] that shown that MLP has the best results.

The number of features were reduced by a feature selection procedure to remove the unimportant and uninformative features.

A leave one out cross-validation procedure was chosen to train the classifiers.

Feature selection, training and validation of classifiers was performed using the Weka Package of Machine Learning Group at the University of Waikato (downloadable from <http://www.cs.waikato.ac.nz/ml/weka/>). Weka is a collection of machine learning algorithms for data mining tasks. The algorithms can either be applied directly to a dataset or called from your own Java code. Weka contains tools for data pre-processing, classification, regression, clustering, association rules, and visualization. It is also well-suited for developing new machine learning schemes.

6.3 Results

6.3.1 Training Set

Results of Automatic ROI Segmentation

The number of input pixels of training set were 25932: 4322 suspicious and 21610 not suspicious. In order to consider balance problem several random partitions were considered: one pixel suspicious and five pixel not suspicious (1:5), one pixel suspicious and 2 pixel not suspicious (1:2) and one pixel suspicious and one pixel not suspicious(1:1).

The table 6.1 reports the sensibility, specificity, accuracy for MLP on the training set with the better classifier parameters for segmentation analysis when the partitions 1:1 were considered.

Table 6.1: Performance on the training-set for Automatic ROI Segmentation

Feature	SENS	SPEC	ACC
Dynamic	0.774	0.825	0.800
Spatial-Temporal	0.501	0.790	0.645
Textural	0.555	0.784	0.669

Results of Automatic ROI Classification

The number of input pixels of training set were 4322: 665 benign and 3657 malignant. In order to consider balance problem several random partitions were considered: one pixel benign and five pixel malignant (1:5), one pixel benign and 2 pixel malignant (1:2) and one pixel benign and one pixel malignant (1:1).

The table 6.2 reports sensibility, specificity, accuracy for MLP on the training set with the better classifier parameters for classification analysis when the partitions 1:1 were considered.

6.3.2 Test set

The table 6.3 reports sensitivity, specificity and accuracy for MLP whit the best feature subset on the test set. The performances in segmentation analysis were better than in classification phase. The best feature subset were chosen on the basis of the highest accuracy on the training set.

Table 6.2: Performance on the training-set for Automatic ROI classification

Feature	SENS	SPEC	ACC
Dynamic	0.861	0.523	0.809
Spatial-Temporal	0.456	0.224	0.420
Textural	0.503	0.095	0.441
All feature	0.689	0.305	0.630

Table 6.3: Performance on the test set

Analysis	SENS	SPEC	ACC
Segmentation	0.919	0.912	0.912
Classification	1	0.4	0.700

6.3.3 Best feature subset

For both segmentation and classification the best subset of features was composed by dynamic features. The dynamic optimal feature subset, for both segmentation and classification, was composed by: basal signal, SOD, relative enhancement slope, relative enhancement that were resulted the features with major discrimination power.

6.4 Discussion

The aim of this study was to propose an approach, based on Multi Layer Perceptron classification of dynamic features, for breast lesions segmentation and classification using DCE-MRI data. In particular, we compared the performance obtainable with different types of features (dynamic, textural, spatio-temporal). Per each pixel within the breasts we extracted 230 features (98 dynamic features, 60 textural features and 72 spatio-temporal features).

Our results indicate that MLP can achieve better results in terms of sensitivity, specificity and accuracy when dynamic features were considered both for ROI segmentation and for lesion classification (accuracy of 91 % and 70 %, respectively).

These findings are in line with recent literature about classification breast lesion. As an example, Tzacheva et al.[91] reported a sensitivity of 90%, a specificity of 91 % and an accuracy of 91 % using morphological features and MLP classifier on 14 breast lesions; Zheng et al. [92]

CHAPTER 6. SEGMENTATION AND CLASSIFICATION USING MACHINE LEARNING APPROACH

reported a sensitivity of 95 % using a combination of temporal, spatial, and morphological attributes and a linear classifier on 31 subjects.

It is worth noting that most of the previous studies in the field [81, 78] used a small population: this is due to the difficulties to enroll patients with the same data acquisition protocol and the absence of a public database.

In the future, we are planning to extend our preliminary study to a greater number of patients and to considerer also morphological feature and Multiple Classification System.

Chapter 7

Lesion classification using Multiple Classification System

In this chapter we will discuss and explain the use of a Multiple Classification System for classification of breast lesions using dynamic and morphological features.

This chapter contains work adapted from:

R. Fusco, M. Sansone, A. Petrillo, C. Sansone. A Multiple Classifier System for Classification of Breast Lesions Using Dynamic and Morphological Features in DCE-MRI. Structural, Syntactic, and Statistical Pattern Recognition Lecture Notes in Computer Science Volume 7626, 2012, pp 684-692.

R. Fusco, M. Sansone, C. Sansone, A. Pepino, A. Petrillo. Classification of breast lesions using dynamic and morphological features in DCE-MRI. GNB 2012, June 26th-29th 2012, Rome, Italy.

7.1 Introduction

In the analysis of breast lesions on MRI, radiologists agree that both *morphological* and *dynamic* features are important for distinguishing benign from malignant [84, 99]. On the one hand, morphological features aim to quantify lesion margins characteristics, and are well assessed in the breast-MRI lexicon [99]: round shape and smooth margin for the benign lesions; more irregular shape for the malignant lesions. On the other hand, dynamic features, have shown a great potential in quantifying vas-

CHAPTER 7. LESION CLASSIFICATION USING MULTIPLE CLASSIFICATION SYSTEM

cularity of tumors: malignant lesions usually show early enhancement with rapid wash out, whereas benign lesions typically show a slow increase followed by persistent enhancement [99].

Many recent works have attempted to take advantage of morphological features and dynamic information in a separate manner: dynamic information has been used for segmentation of volume of interests (VOIs) [96, 97, 98], while morphological features of the VOIs have been used for lesion classification [99, 100, 92]. For example, Nie et al. [95] demonstrated that quantitative analysis of morphology and texture features of breast lesions was feasible, and these features could be selected by artificial neural network to form a classifier for differential diagnosis. Agner et al. [76] demonstrated that using a probabilistic boosting tree (PBT) classifier in conjunction with textural kinetic descriptors an accuracy of 90%, sensitivity of 95% a specificity of 82% can be yielded, while when textural kinetic attributes were combined with morphologic descriptors, an accuracy of 89%, a sensitivity of 99%, and a specificity 76% can be yielded. Tzacheva et al. [91] reported a sensitivity of 90%, a specificity of 91 % and an accuracy of 91 % using morphological features and MLP classifier on 14 breast lesions; Zheng et al. [92] reported a sensitivity of 95 % using a combination of dynamic, spatial, and morphological attributes and a linear classifier on 31 subjects.

However, a Multiple Classification System for classification of breast lesions using both dynamic and morphological features in DCE-MRI is not yet present in literature, although the idea of combining multiple classifiers is not new. For example, Keyvanfard et al. [104] proposed a multi classifier system of three classifiers that use dynamic features to classify breast lesion in DCE-MRI, but in their study morphological features were not used.

The aim of the present study is to propose a Multiple Classification System (MCS) for classification of breast lesions using both dynamic and morphological features in DCE-MRI.

The proposed MCS combines the results of two classifiers trained with dynamic and morphological features respectively. Four classifiers were examined: multilayer perceptron, support vector machine, Bayes classifier and decision tree classifier.

38 women (average age 46 years) with benign or malignant lesions histopathologically proven were enrolled. 21 lesions were malignant and 17 were benign. The lesions were subdivided in two groups: training-test (12 benign and 16 malignant) and test-set (5 benign and 5 malignant).

7.2 Methods

7.2.1 Morphological and Dynamic features

In this study was performed a training of several classifiers (MLP, DT, SVM and Bayes classifier) with 54 morphological features and 98 dynamic features.

The main categories of morphological features included areas, circularity, compactness, complexity, perimeter, radial length, smoothness, roughness, sphericity, eccentricity, volume, rectangularity, solidity, spiculation, convexity, curvature, edge [99, 100, 92]. For dynamic features the main categories included area, maximum intensity ratio, relative enhancement, relative enhancement slope, basal signal, perfusion index, sum of intensities difference (SOD), wash-in, wash-out, time to peak [96, 97, 98].

Training machine learning classifiers with large numbers of morphological features can lead to classifier overfitting, reduces the generalization capabilities of the classifiers and slows down the training process.

The number of morphological and dynamic features were reduced by a feature selection procedure to remove the unimportant and uninformative morphological features. To keep the loss of information to a minimum we tested Correlation-based Feature Selection (CFS) and Consistency feature Selection method with several search: the forward search, the backward search, the bidirectional search, the greedy search, feature ranking methods.

The dynamic features obtained by selection procedure were the same for all the classifiers: sum of intensities difference (SOD), basal signal and relative enhancement slope [96, 97, 98]).

The morphological features obtained by selection procedure were different per each classifier [99, 100]: MLP (area, smoothness, radial length, roughness); BC (area, eccentricity, compactness, perimeter); SVM (area, eccentricity, compactness, perimeter, radial length, roughness, smoothness and sphericity); DT (eccentricity).

7.2.2 VOI Classification

The proposed Multiple Classification System combines the results of two classifiers trained separately with dynamic and morphological features respectively (fig. 7.1): in particular it was considered the weighted

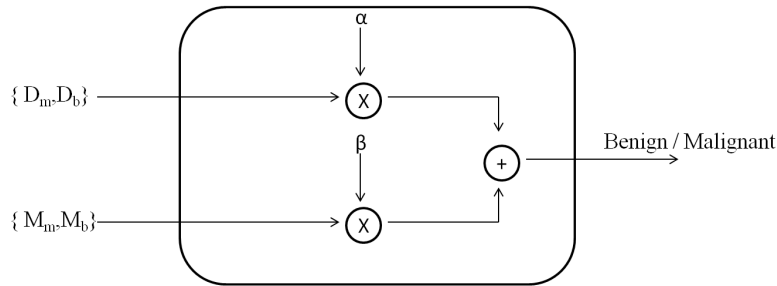


Figure 7.1: Multiple Classification System.

sum of probability of malignity and the probability of benignity of two optimal classifiers [103].

We trained four machine learning algorithms: a Multi Layer Perceptron (MLP), a support Vector Machine (SVM), a Bayesian classifier (BC) and a decision tree (DT) [93].

When using dynamic features the classifiers were set with the following parameters: MLP (learning rate = 1.0, momentum = 0.5, epoche = 300); SVM (kernel = RBF, sigma = 0.1); BC (kernel estimator = false); DT (confidence factor = 0.5, unpruned = false).

When using morphological features the classifiers were set with the following parameters: MLP (learning rate = 0.3, momentum = 0.2, epoche = 400); SVM (kernel = RBF, sigma = 0.1); BC (kernel estimator = true); DT (confidence factor = 0.1, unpruned = true).

We estimated the classifier parameters using the training data and the subset of features obtained by feature selection methods varying classifier parameters values and evaluating the accuracy.

Classifier of dynamic features

Each suspicious pixel within the VOI (either manually or automatically segmented) has been re-classified as *benign* or *malignant* on the basis of dynamic features only. The whole VOI has been classified as malignant if the number of malignant pixels n_m within the VOI was higher than that of benign pixel n_b within the same VOI.

CHAPTER 7. LESION CLASSIFICATION USING MULTIPLE CLASSIFICATION SYSTEM

The probabilities of malignant lesion (D_m) and benign lesion (D_b) were calculated as eq. 7.1:

$$\begin{aligned} D_m &= \frac{n_m}{N} \\ D_b &= \frac{n_b}{N} \end{aligned} \quad (7.1)$$

where N is the total number of pixels in the lesion.

Classifier of morphological features

Morphological features were calculated for the whole VOI and were used to classify the lesion in malignant and benign. In this case the probability of malignity and benignity were M_m and M_b respectively.

Combination scheme

The VOI was classified as malignant if $\alpha D_m + \beta M_m > \alpha D_b + \beta M_b$, where α and β were multiplicative coefficients ($\alpha + \beta = 1$) obtained maximizing the accuracy on the training-set (fig. 7.1).

7.3 Results

Table 7.1 reports the findings on training-set. Table 7.2 reports the findings on training test. The acronyms used in both tables are as follows: MC = Classifier trained with morphological feature; DC = Classifier trained with dynamic feature; VOI = VOI Segmentation (man=manual, aut=automatic).

Table 7.1: Results on training-set.

VOI	MC	DC	α	β	accuracy[%]
man	BC	BC	0.60	0.40	75
man	BC	MLP	0.60	0.40	75
aut	DT	BC	0.68	0.33	68

Table 7.2: Results on test-set.

VOI	MC	DC	α	β	accuracy[%]
man	BC	BC	0.60	0.40	70
aut	DT	BC	0.68	0.33	70

7.4 Discussion

This study had as objective to evaluate the performance of a Multiple Classification System (MCS) using dynamic and morphological features of breast lesions in Dynamic Contrast Enhanced-Magnetic Resonance Imaging (DCE-MRI).

The proposed MCS combines the results of two classifiers trained with dynamic and morphological features respectively. Four classifiers were examined: multilayer perceptron, support vector machine, Bayes classifier and decision tree classifier.

Twenty-one malignant and seventeen benign breast lesions, histologically proven, were analyzed. Volumes of Interest (VOIs) have been both manually extracted by an expert radiologists and automatically extracted via a segmentation procedure assessed in a previous study. Both dynamic and morphological features were extracted. The performance of the MCS have been compared with histological classification.

Results indicated that with manually segmented VOIs the best combination includes two Bayes classifiers (75% of training-set and 70% of test-set correctly classified with sensitivity of 100%); when using automatic segmented VOIs the best combination includes a decision tree and Bayes classifiers (68% of training-set and 70% of test-set correctly classified with sensitivity of 100%).

The findings of this study are in line with recent literature. In fact, Wedegärtner et al [102] reports a sensitivity of 85% using morphological features and a receiver operating characteristic (ROC) curve for 62 breast lesions without automatic classification method, Tzacheva et al.[91] reported a sensitivity of 90%, a specificity of 91% and an accuracy of 91% using morphological features and MLP classifier on 14 breast lesions. However, it is worth noting that Tzacheva et al. [91] study used a small number of patients. Zheng et al [92] reports a sensitivity of 95% using a combination of temporal, spatial, and morphological attributes and a linear classifier for 31 subjects.

These authors present higher accuracy in comparison of our findings but they not use several classifier to evaluate morphological and dynamic

CHAPTER 7. LESION CLASSIFICATION USING MULTIPLE CLASSIFICATION SYSTEM

discrimination power with a completely automatic multi-classifier system. Moreover a different choice of α and β coefficients could consent to obtain also a 100% of accuracy.

The main difference between our approach and previous studies lies in the combination scheme that allows to take advantage of both dynamic and morphological features of DCE-MRI examinations.

Chapter 8

General Discussion

In this work we provided a thorough discussion of the theoretical framework of quantitative and semi-quantitative analysis of DCE-MRI data, in fact the principal aim of this thesis was investigate the use of semi-quantitative and quantitative parameters for segmentation and classification of breast lesion in DCE-MRI. Although the application of the discussed models and methods is not limited to the context of DCE-MRI of the breast, we performed our investigation with that perspective in mind. In doing so, we focused on common clinical practice.

General objectives of works were:

1. describe the principal techniques to evaluate the time intensity curve in DCE-MRI with focus on kinetic model proposed in literature;
2. evaluate the influence in the choice of parameterisation for a classic bi-compartmental kinetic models
3. evaluate the performance of a method for simultaneous tracer kinetic modelling and pixel classification in suspicious and not suspicious
4. evaluate the performance of machine learning techniques training with morphological, textural and dynamic feature for segmentation and classification of breast lesion

General aim of this work were to address the problem of classification of breast lesions starting with a fully automatic segmentation of suspicious lesions of the breast. The automatism of the process was possible by analyzing the magnetic resonance images with adequate knowledge

about the patho-physiology of tumors (morphology, heterogeneity, vascularization) and using procedures of pattern recognition. For this reason were analyzed and calculated by simple morphological and textural characteristics to the more complex features of enhancement of the contrast medium of tumors, by applying kinetic compartmental models. This was possible only after studying different kinetic resolution models proposed in the literature and after studying the goodness of the estimated kinetic parameters to change settings such as acquisition time and sampling period of DCE-MRI images. The innovative aspects of this work, compared to the state of the art, they are different: the comparison between models DP and CC was not yet in the literature and it is important to identify the models to be used in specific conditions of settings and when the data of acquisition are few (low temporal resolution); analysis of the curvature in the context of DCE-MRI had not yet been made in the literature, but instead is because it clarifies the limits of the parameters on the accuracy of parameter estimation; the segmentation technique based on EM represents an evolution compared to conventional segmentation methods that are based only on the levels of gray of the image because it takes into account also the dynamic evolution of the pixels; the combined use of features of different types (morphological, textural and dynamic) and of systems of multi-classification for the segmentation and the classification of breast lesions were not yet in the literature and it is important to improve the classification of the automatic systems.

A general discussion on issues that were not addressed in the preceding chapters will be given here, including future perspectives.

8.1 Comparison of kinetic models

A wide-scale of kinetic models, into clinical practice, have been proposed by different authors.

Controversy has shown about the use of distributed (DP) versus conventional compartmental (CC) model. In fact, while DP models seem to be more realistic, CC models (in particular the Tofts and the Brix models) have been widely used in clinical investigations over the past two decades.

From our work in Chapter 3 we conclude that on DCE-MRI TWIST data ATH obtained better fits than Tofts and Brix models. As regards the reliability of the estimates it turned out that no model was capable of estimating all the parameters with reliability lower than about 10% and in some cases the reliability was very low. Instead In the analysis of DCE-

MRI FLASH data we found that Brix obtained better fit than Tofts in 77% of voxels. Also in this case the estimated parameters were comparable, however the reliability of the estimates obtained using Brix was higher than Tofts.

8.2 Influence of parameterisation in kinetic modelling estimation

An topic in kinetic analysis is the repeatability of the parameters estimates. The convergence of Least-Squares algorithms and the repeatability of the estimates is affected by the curvature of the model. An adequate choice of the parameterisation can reduce curvature thus improving parameter estimation. We describe the curvature of the model as measures of non linearity In the chapter 4 we analyzed the influence of two parameterisations on the curvature of the widespread Tofts' model and the influence of the total acquisition time and of the sampling period. We calculated both the intrinsic curvature and the parameters-effect curvature for several points in the parameters space and for several values of sampling period and total acquisition time.

The results of this study can be summarized in two points. First, for both parameterisations the parameters-effect curvature is predominant over the intrinsic curvature and the curvature of the parameterisation (K_{trans}, v_e) is lower than that of (K_{trans}, K_{ep}) (see figure ??) for a large range of parameters (the extension of this range is little affected by the sampling period). Second, when considering (K_{trans}, v_e) only, the range of parameters having below-threshold curvature becomes wider as the total acquisition time increases (although little difference is observed for total acquisition time longer than 6 min).

However, the opposite occurs when the sampling period increases.

8.3 Motion artifacts

We did not address the correction of motion artifacts in this work. However, the absence/correction of motion during the acquisition of the dynamic contrast-enhanced series is crucial for kinetic analysis. With motion, possibly many pixels will display erroneous enhancement patterns that could be mistakenly assessed as malignant/benign. Of course,

pixel-wise kinetic mapping will suffer more from motion artifacts than ROI-wise interrogation of kinetics.

8.4 Automatic simultaneous pixel classification and tracer kinetic modelling using EM approach

Segmentation of breast lesion is the first critical step in breast diagnosis, in fact the step of manual ROI placement is likely to introduce inter-observer variability in the final diagnostic outcome and it is time consuming.

The use of kinetic analysis software is not (yet) wide-spread also if with the automatic generation of kinetic maps, the radiologist may be confronted with several color-coded images, one for each model parameter and can combine the information from these different maps for radiological assessment. Probably, few radiologists have enough experience with pharmacokinetic modeling. Therefore, an intuitive and user-friendly way of providing pharmacokinetic information will be necessary to enable wide clinical use of such kinetic analysis techniques.

In the chapter 5 we have assessed, by means of simulations, the performances of an Expectation-Maximisation scheme for simultaneous pixel classification in suspicious and no suspicious and tracer kinetic modelling.

The proposed EM scheme was expected to provide average kinetic parameters because pixels having high probability to belong to the same class are used to estimate the parameters of that class, thus increasing the effective signal-to-noise ratio with respect to the standard pixel-by-pixel approach in which pixels are examined separately.

From results of this study it can be deduced that our approach can effectively increase SNR if it can be assumed that pixels belonging to the 'enhancing' region (suspicious pixel) have similar tracer kinetic parameters. When this hypothesis is satisfied, our approach can provide a good estimate of 'average' kinetic parameters. Anyway, when this hypothesis is not fully satisfied because of the intrinsic heterogeneity of tumors [67, 75] our method can still provide an overall characterization of the angiogenic activity of the whole tumour, as was suggested by our simulations.

Preliminary results on real data show that EM provides a reasonable estimate of the 'average' parameters. While the EM method is mainly

directed to give overall information, the capability to provide a probability map indicates that information about heterogeneity is not lost and can be further evaluated.

8.5 Automatic Segmentation and Classification using Machine Learning approach

As stressed in chapter 6 a number of automatic lesion segmentation approaches [?, 89] have been proposed and There is still a debate in the literature regarding the interpretation strategies and the relative importance of textural and dynamic features in the discrimination of benign from malignant lesions.

Fewer investigators have attempted to integrate spatial and temporal features [88] and fewer researcher have proposed a completely automatic method for segmentation and classification breast lesions.

We was to propose an approach, based on Multi Layer Perceptron classification of dynamic, textural and spatio-temporal features, for breast lesions segmentation and classification using DCE-MRI data.

Our results indicated that MLP can achieve better results in terms of sensitivity, specificity and accuracy when dynamic features were considered both for ROI segmentation and for lesion classification (accuracy of 91 % and 70 %, respectively).

8.6 Quantitative morphologic and textural assessment

We mentioned in the introduction of chapter 7 that DCE-MRI quantitative analysis is not necessarily restricted to dynamic analysis. The assessment of morphologic and textural features using concentration images are interesting to breast lesion classification. In fact in the chapter 7 we have evaluate the performance of a Multiple Classification System (MCS) using dynamic and morphological features of breast lesions. Results indicated that using a MCS system there is a improvement of accuracy in comparison of single classifiers reaching un accuracy major of 90%.

8.7 Assessment of treatment effects

The assessment of treatment response, especially in case anti-vascular or antiangiogenic agents are used, remains major challenge. In this study is not addressed this aspect. However, with the use of higher temporal resolution data, of an extended kinetic model, of machine learning approaches can be found clues about the mechanisms of the anti-inflammatory drug to asses early therapy response.

8.8 Future endpoints

Future endpoints including:

- extension of The EM approach to the analysis of larger regions (using a full EM multi-class approach with spatial constraints)
- integration of morphological, dynamic using semi-quantitative and quantitative feature based on kinetic model, and texture [93] features with Multiple Classification System for breast classification
- manual segmentation performed by multiple readers
- extension of analysis on a larger number of patients
- use this analysis to asses early anti-angiogenic therapy response.

Chapter 9

List of publications

9.1 Books Coauthors

R. Fusco, M. Sansone, M. Petrillo, A. Avallone, P. Delrio and A. Petrillo (2011). Dynamic Contrast Enhanced Magnetic Resonance Imaging in Rectal Cancer, Rectal Cancer - A Multidisciplinary Approach to Management, Giulio Aniello Santoro (Ed.), ISBN: 978-953-307-758-1, InTech

Fusco R., Sansone M. , Petrillo M., Avallone A., Delrio P., and Petrillo A. Dynamic Contrast Enhanced Magnetic Resonance Imaging in Rectal Cancer in Rectal Cancer; InTech. In Press

9.2 Journal publications

M. Sansone, R. Fusco, A. Petrillo, M.Petrillo, M.Bracale. An Expectation-Maximisation approach for simultaneous pixel classification and tracer kinetic modelling in Dynamic Contrast Enhanced-Magnetic Resonance Imaging. Medical and Biological Engineering and Computing, 2011 Apr;49(4): 485 - 95

P. Melillo, R. Fusco, M. Sansone, M. Bracale, e L. Pecchia, "Discrimination power of long-term heart rate variability measures for chronic heart failure detection," Medical and Biological Engineering and Computing, vol. 49, 2011, pagg. 67-74

S. Perdonà, G. Di Lorenzo, R. Autorino, C. Buonerba, M. De Sio, S.V.

Setola, R. Fusco, F.M. Ronza, M. Caraglia, M. Ferro, A. Petrillo. Combined magnetic resonance spectroscopy and dynamic contrast-enhanced imaging for prostate cancer detection. *Urol Oncol.* 2011 Sep 7

R. Fusco, M. Sansone, M. Petrillo, A. Petrillo. Influence of parameterization on tracer kinetic modeling in DCE-MRI. *Journal of Medical and Biological Engineering*, Uncorrected Proof Available online 7 Sep 2012, doi: 10.5405/jmbe.1097

R. Fusco, M. Sansone, S. Maffei, A. Petrillo. Dynamic Contrast-Enhanced MRI in Breast Cancer: A Comparison between Distributed and Compartmental Tracer Kinetic Models. *Journal of Biomedical Graphics and Computing*, vol. 2, no. 2, p. p23, Aug. 2012

R. Fusco, A. Petrillo, O. Catalano, M. Sansone, V. Granata, S. Filice, M. D'Aiuto, Q. Pankhurst, M. Douek. Procedures for non-palpable breast lesions localization: a systematic review for the radiologist. *BRCA*. Proof Available online 17 Ottobre 2012, doi: 10.1007/s12282-012-0427-1

R. Fusco, A. Petrillo, M. Petrillo, M. Sansone. Use of tracer kinetic models for selection of semi-quantitative features for DCE-MRI data classification. *IEEE Transaction on Biomedical Engineering*. Submitted the 19/10/2012

A. Petrillo, R.Fusco, S.V. Setola, F.M. Ronza, V. Granata, M. Sansone, G. Palma, R. Franco, F. Fulciniti, S. Perdonà. Multiparametric MRI for prostate cancer detection: performance in patients with PSA between 2.5 and 10 ng/ml. *Journal of Magnetic Resonance Imaging*. Submitted the 17/7/2012

9.3 Conference proceedings

M. Sansone, F. Aprile, R. Fusco, A. Petrillo, M. Petrillo, A. Siani, U. Bracale. Reference based time intensity curves quantification in DCE-MRI monitoring of rectal cancer. *Proceedings of 11th World Congress on Medical Physics and Biomedical Engineering*, September 7-12, 2009 in Munich, Germany

M. Sansone, R. Fusco, F. Aprile, A. Petrillo, M. Petrillo, A. Siani, U.

CHAPTER 9. LIST OF PUBLICATIONS

Bracale. Evaluation of different Tracer Kinetic Models in DCE-MRI of Rectal Cancer. Proceedings of 11th World Congress on Medical Physics and Biomedical Engineering, September 7-12, 2009 in Munich, German

Petrillo, M. Petrillo, M. Sansone, R. Fusco, U. Bracale, A. Siani. Dynamic contrast enhanced magnetic resonance imaging (DCE-MRI): Validation of different quantitative pharmacokinetic models in monitoring neo-adjuvant treatment in advanced rectal cancer. Proceedings of European Congress of Radiology (ECR 2010), March 4-8

R. Fusco, M. Sansone, A. Petrillo, M. Petrillo, M. Bracale. Simultaneous Pixel Classification And Compartmental Modelling Of Dce-Mri In Breast Cancer. GNB 2010 Torino, 8-10 July

A. Barbieri, M. Barretta, G. Palma, M. Gala, A. Luciano, F. Olimpia, C. Picone, A. Gallipoli D'errico, R. Fusco, A. Petrillo, R. V. Iaffaioli, C. Arra. Imaging application for preclinical cancer studies. Simposio AISAL 2010 Bologna, 4-5 November

R. Fusco, M. Sansone, M. Petrillo, D. Amato, Y. mandato, G. Fabozzi, S. V. Setola, F. Sandomenico, A. Petrillo. Simultaneous pixel classification and compartmental modelling of DCE-MRI in breast cancer. ECR 2011 Abstract Book, March 3-7 Vienna, DOI: 10.1594/ecr2011/C-0480

V. Granata, R. Fusco, M. Sansone, M. Petrillo, E. de Lutio di Castelligudone, G. Palma, S. Filice, A. Gallipoli D'Errico, A. Petrillo. Dynamic Contrast Enhanced-Magnetic Resonance Imaging (DCE-MRI) Monitoring of Locally Advanced Rectal Cancer using Time Intensity Curve Shape Characterization. ECR 2011 Abstract Book, March 3-7 Vienna, DOI: 10.1594/ecr2011/C-0740

F. M. Ronza, S. V. Setola, V. Granata, R. Fusco, S. Filice, A. Di Finizio, R. Grassi, A. Rotondo, A. Petrillo. Young radiologist learning curve in MRI/MRS prostate cancer evaluation: preliminary result. ECR 2011 Abstract Book, March 3-7 Vienna, DOI: 10.1594/ecr2011/C-0886

A. Porto, R. Fusco, M. Mattace Raso, V. Granata, G. Palma, M. D'Aiuto, R. Grassi, A. Rotondo, A. Petrillo. Breast Dynamic Contrast Enhanced-Magnetic Resonance Imaging (DCE-MRI) in women under forty: does MRI increase inappropriate mastectomy?. ECR 2012 Abstract Book, March

CHAPTER 9. LIST OF PUBLICATIONS

3-7 Vienna; DOI: 10.1594/ecr2011/C-2071

M. Petrillo, R. Fusco, M. Sansone, A. Petrillo: Standardized Index of Shape (SIS): an effective DCE-MRI semi quantitative index to assess pre-operative radio-chemo therapy (pCRT) in Locally Advanced Rectal Cancer (LARC). The European Society of Gastrointestinal and Abdominal Radiology (ESGAR 2011); May 21-24 Venezia

M. Petrillo, R. Fusco, V. Granata, P. Delrio, A. Avallone, B. Pecori, F. Tatangelo, C. Sassaroli and A. Petrillo. Standardized Intensity Ratio: robust, effective and reproducible DCE-MRI semi-quantitative index to monitor LARC before and after preoperative combined radio and chemotherapy. ESCP 6th Scientific and Annual Meeting Copenhagen, 21-24 September 2011

R. Fusco, M. Sansone, C. Sansone, and A. Petrillo Selection of suspicious ROIs in breast DCE-MRI. International Conference on Image Analysis and Processing (ICIAP 2011); Settembre 14-16 Ravenna

R. Fusco, M. Petrillo, S. Setola, M. Sansone, A. Rotondo, A. Petrillo. Standardized Index of Shape (SIS): a novel semi-quantitative DCE-MRI parameter based on Pattern Analysis (PA) able to divide Responder (R) by Not Responder (NR) after preoperative radio-chemo therapy (pCRT) in Locally Advanced Rectal Cancer (LARC). ECR 2012 Abstract Book (abs).

M. Petrillo, R. Fusco, V. Granata, O. Catalano, M. Sansone, A. Rotondo, R. Grassi, A. Petrillo. Assessment of preoperative radio-chemo therapy (pCRT): a novel numerical semi-quantitative DCE-MRI parameter compared with morphologic MRI (mMRI) and qualitative time intensity curves (tMRI). ECR 2012 Abstract Book (abs).

R. Fusco, M. Sansone, D. Amato, M. Mattaceraso, A. Petrillo. Selection of suspicious ROIs in breast DCE-MRI. ECR 2012 Abstract Book (abs)

R. Fusco, M. Sansone, C. Sansone, A. Rotondo, A. Petrillo. Segmentation and classification of breast lesions using dynamic and textural features in Dynamic Contrast Enhanced-Magnetic Resonance Imaging. Atti del CBMS 2012, June 20-22 Rome-Italy

R. Fusco, M. Sansone, C. Sansone, A. Pepino, A. Petrillo. Classification

CHAPTER 9. LIST OF PUBLICATIONS

of breast lesions using dynamic and morphological features in DCE-MRI. GNB 2012, June 26th-29th 2012, Rome, Italy

M. Petrillo, R. Fusco, V. Granata, O. Catalano, A. Rotondo. Preliminary experience in comparing Tumor Volume Change (TVC) among MRI Volumetry (MRV), DCE-MRI Volumetry (DCE-MRV) and DW-MRI Volumetry (DWIV) to evaluate response to neoadjuvant therapy (pCRT) in Locally Advanced Rectal Cancer. ESMRMB 2012, Lisbona 4-6 October

M. Petrillo, R. Fusco, V. Granata, O. Catalano, A. Rotondo. Preliminary experience: a novel DCE-MRI approach based on Functional Volumetric estimation (Standardized index of Shape, SISV) to differentiate responder by not responders after neo-adjuvant therapy in locally advanced rectal cancer (LARC) . ESMRMB 2012, Lisbona 4-6 October

R. Fusco, M. Sansone, S. Filice, A. Petrillo. A multiple classification system for classification of breast lesions using dynamic and morphological features in DCE-MRI. ESMRMB 2012, Lisbona 4-6 October

Bibliography

- [1] A. Jackson, D. L. Buckley, G. J. M. Parker et al. *Dynamic Contrast-Enhanced Magnetic Resonance Imaging in Oncology*. Springer 2005
- [2] A. Glantz *Statistica per discipline biomediche* McGraw-Hill.
- [3] K. Fukunaga *Introduction to Statistical Pattern Recognition* Elsevier 1990.
- [4] E. Hendrick *Breast MRI Fundamentals and Technical Aspects* Springer 2008.
- [5] Seber GAF and Wild CJ. *Nonlinear Regression*. , Wiley Interscience John Wiley and Sons, Hoboken New Jersey (2003)
- [6] Roberta Fusco, Mario Sansone, Mario Petrillo, Antonio Avalone, Paolo Delrio and Antonella Petrillo *Dynamic Contrast Enhanced Magnetic Resonance Imaging in Rectal Cancer, Rectal Cancer - A Multidisciplinary Approach to Management, Giulio Aniello Santoro (Ed.)*, ISBN: 978-953-307-758-1, InTech, Available from: <http://www.intechopen.com/books/rectal-cancer-a-multidisciplinary-approach-to-management/dynamic-contrast-enhanced-magnetic-resonance-imaging-in-rectal-cancer>.
- [7] Lavini C, de Jonge MC, van de Sande MGH, Tak P, Nederveen J, Maas M “Pixel-by-pixel analysis of DCE MRI curve patterns and an illustration of its application to the imaging of the musculoskeletal system.”, *Magnetic Resonance Imaging* , vol. 25, pp. 604-612, 2007.
- [8] Varini C, Degenhard A, Nattkemper TW “Visual exploratory analysis of DCE-MRI data in breast cancer by dimensional data reduction: A comparative study.”, *Biomedical Signal Processing and Control*, vol. 1, pp. 56-63, 2006.

- [9] Tuncbilek N, Karakas HM and Altaner S “Dynamic mri in indirect estimation of microvessel density, histologic grade, and prognosis in colorectal adenocarcinomas.”, *Abdom Imaging*, vol. 19, pp. 166-172, 2004.
- [10] AR Padhani “Dynamic contrast-enhanced MRI studies in human tumours”, *Br J Radiol* , vol. 72, pp. 427-431, 1999.
- [11] AR Padhani “Dynamic contrast-enhanced MRI in clinical oncology: current status and future directions”, *J Magn Reson Imaging*, vol. 16, pp. 407-422, 2002.
- [12] L. Choyke, A. J. Dwyer, M. V. Knopp “Functional Tumor Imaging With Dynamic Contrast-Enhanced Magnetic Resonance Imaging”, *Journal of Resonance Imaging*, vol. 17, pp. 509-520, 2003.
- [13] P. Tofts, BA. Berkowitz “Measurement of capillary permeability from the Gd enhancement curve: a comparison of bolus and constant infusion injection methods” *Magn Reson Imaging*, vol. 12, pp. 81-91, 1994.
- [14] P. Tofts, G. Brix, DL. Buckley, JL. Evelhoch, E. Henderson, MV. Knopp, et al. “Estimating kinetic parameters from dynamic contrast enhanced T1-w MRI of a diffusible tracer: standardized quantities and symbols”, *J Magn Reson Imaging*, vol. 10, pp. 223-232, 1999.
- [15] JU. Harrer, GJ. Parker, HA. Haroon, DL. Buckley, K. Embelton, C. Roberts, et al. “Comparative study of methods for determining vascular permeability and blood volume in human gliomas”, *J Magn Reson Imaging*, vol. 20, pp. 748-757, 2004.
- [16] DL. Buckley “Uncertainty in the analysis of tracer kinetics using dynamic contrast enhanced T1-weighted MRI”, *Magn Reson Med*, vol. 47, pp. 601-606, 2002.
- [17] D. De Lussanet, H. Backes, et al. “Dynamic Contrast-Enhanced Magnetic Resonance Imaging of Radiation Therapy-Induced Microcirculation Changes In Rectal Cancer”, *J. Radiation Oncology Biol. Phys.*, vol. 63, pp. 1309-1315, 2005.
- [18] S. Walker-Samual, M. O Lench and D. J Collins “Reference tissue quantification of DCE-MRI data without a contrast agent calibration”, *Phys. Med. Biol*, vol. 52, pp. 589-601, 2007.

- [19] L. Choyke, J. Dwyer, V. Knopp "Functional Tumor Imaging With Dynamic Contrast-Enhanced Magnetic Resonance Imaging", *JOURNAL OF MAGNETIC RESONANCE IMAGING*, vol. 17, pp. 509-520, 2003.
- [20] M. Muller-Schimpffie, G. Brix, G. Layer, P. Schlag, R. Engenhart, et al. "Recurrent Rectal Cancer: Diagnosis with Dynamic MR Imaging", *Radiology*, vol. 189, pp. 881-889, 1993.
- [21] P. Tofts "Modeling Tracer Kinetics in Dynamic Gd-DTPA MR Imaging", *JMRI*, vol. 7, pp. 91-101, 1997.
- [22] P. Tofts "Accuarate Estimation of Pharmacokinetic Contrast-Enhanced Dynamic MRI Parameters of the Prostate", *Journal of Magnetic Resonance Imaging*, vol. 13, pp. 607-614, 2001.
- [23] G. Tofts et al. "Pharmacokinetic Parameters in CNS Gd-GDTA enhanced MR imaging", *CompuAssist Tomogr*, vol. 15, pp. 621-628, 1991.
- [24] B. Larson et al. "Myocardial Perfusion Modeling Using MRI", *MRM*, vol. 35, pp. 716-726, 2001.
- [25] St. Lawrence, TY. Lee et al. "An adoabatia approximation to the tissue homogeneity model for water exchange in the brain", *J Cereb Bllod Flow Metab*, vol. 18, pp. 1365-1377, 1998.
- [26] HB.Larsson, M. Stubgaard, JL. Frederiksen, M. Jensen, O. Henriksen, OB. Paulson " Quantitation of blood-brain barrier defect by magnetic resonance imaging and gadolinium-DTPA in patients with multiple sclerosis and brain tumors", *Magn Reson Med*, vol. 16, pp. 117-131, 1990.
- [27] G.Parker, I. Baustert, S. Tanner, M. Leach " Improving image quality and T1 measurements using saturation recovery turboFLASH with an approximate K-space normalisation filter", *Magnetic Resonance Imaging*, vol. 18, pp. 157-167, 2000.
- [28] A.Parker, T. Redpath, F. Gilbert, A. Murray, R. Staff " Accuracy of T1 Measurement in Dynamic Contrast-Enhanced Breast MRI Using Two- and Three-Dimensional Variable Flip Angle Fast Low-Angle Shot", *JOURNAL OF MAGNETIC RESONANCE IMAGING*, vol. 9, pp. 163-171, 1999.

- [29] G.Parker, S. Tanner, M. Leach et al. "Probing Tumor Microvasculature by Measurement, Analysis and Display of Contrast Agent Uptake Kinetics", *JMRI*, vol. 7, pp. 564-574, 1997.
- [30] NE. Simpson, JL. Evelhoch "Deuterium NMR tissue perfusion measurements using the tracer uptake approach: I. Optimization of methods", *Magn Reson Med*, vol. 42, pp. 42-52, 1999.
- [31] E. Smith, H. Barret "Hotelling trace criterion as a figure of merit for the optimization of imaging systems", *Image Science*, vol. 3, pp. 717-725, 1986.
- [32] F. DeVries, J. Griebel, C. Kremser, W. Judmaier, T. Gneiting, A. Kreczy, D. Öfner, K. Pfeiffer, G. Brix, P. Lukas "Tumor Microcirculation Evaluated by Dynamic Magnetic Resonance Imaging Predicts Therapy Outcome for Primary Rectal Carcinoma", *Cancer Research*, vol. 61, pp. 2513-2516, 2001.
- [33] MO. Leach et al. "The assessment of antiangiogenic and antivascular therapies in early-stage clinical trials using magnetic resonance imaging: issues and recommendations", *BR J Cancer*, vol. 92, pp. 1599-1610, 2005.
- [34] L. Daniel et al. "Breast Disease: Dynamic Spiral MR Imaging", *Radiology*, vol. 209, pp. 499-509, 1998.
- [35] JPB O'Connor, A. Jackson, GJM Parker, GC Jayson "DCE-MRI biomarkers in the clinical evaluation of antiangiogenic and vascular disrupting agents", *British Journal of Cancer*, vol. 96, pp. 189-195, 2007.
- [36] R. Beets, G. Beets "Rectal Cancer: Review with Emphasis on MR Imaging", *Radiology*, vol. 232, pp. 335-346, 2004.
- [37] C. Rodel et al. "Prognostic Significance of Tumor Regression After Preoperative Chemoradiotherapy for Rectal Cancer", *JOURNAL OF CLINICAL ONCOLOGY*, vol. 34, pp. 8688-8696, 2005.
- [38] G. Atkin, N. J. Taylor, F. M. Daley, J. J. Stirling, P. Richman, R. Glynne-Jones, J. A. d'Arcy, D. J. Collins and A. R. Padhani "Dynamic contrast-enhanced magnetic resonance imaging is a poor measure of rectal cancer angiogenesis", *British Journal of Surgery*, vol. 93, pp. 992-1000, 2006.

- [39] Zwick S, Brix G, Tofts PS, Strecker R, Kopp-Schneider A, Laue H, Semmler W, Kiessling F. "Simulation-based comparison of two approaches frequently used for dynamic contrast-enhanced MRI", *Eur Radiol*, vol. 20(2), pp. 4322-42, 2010.
- [40] Sansone M, Fusco R, Petrillo M, Petrillo A, Bracale M. "An expectation maximisation approach for simultaneous pixel classification and tracer kinetic modelling in dynamic contrast enhanced-magnetic resonance imaging.", *Med Biol Eng Comput*, vol. 49(4), pp. 485-95, 2011.
- [41] Johnson JA, Wilson TA. "A model for capillary exchange.", *Am J Physiol*, vol. 210, pp. 1299-1303, 1966.
- [42] Koh TS, Cheong LH, Hou Z, Soh YC. "A physiologic model of capillary-tissue exchange for dynamic contrast-enhanced imaging of tumor microcirculation.", *IEEE Trans Biomed Eng.*, vol. 50, pp. 159-167, 2003.
- [43] Brix G, Griebel J, Kiessling F, Wenz F, Eur J. "Tracer kinetic modelling of tumour angiogenesis based on dynamic contrast-enhanced CT and MRI measurements.", *Nucl Med Mol Imaging.*, vol. 37 Suppl 1, pp. S30-51, 2010.
- [44] Bradley DP, Tessier JJ, Lacey T et al. "Examining the acute effects of cediranib (RECENTIN, AZD2171) treatment in tumor models: a dynamic contrast-enhanced MRI study using gadopentate.", *Acad Radiol.*, vol. 14, pp. 561-573, 2009.
- [45] Chou CP, Wu MT, Chang HAT et al. "Monitoring breast cancer-response to neoadjuvant systemic chemotherapy using parametric contrast-enhanced MRI: a pilot study.", *Acad Radiol.*, vol. 14, pp. 561-573, 2007.
- [46] Chun H, Clymer B, Sammet S et al. "Improvement in the reproducibility of region of interest using an auditory feedback loop: a pilot assessment using dynamic contrast-enhanced (DCE) breast MR images.", *J Magn Reson Imaging.*, vol. 27, pp. 27-33, 2008.
- [47] Giesel FL, Choyke PL, Mehndiratta A et al. "Pharmacokinetic analysis of malignant pleural mesothelioma: initial results of tumor microcirculation and its correlation to microvessel density (CD-34).", *Acad Radiol.*, vol. 15, pp. 563-570, 2008.

- [48] Weinmann HJ, Laniado M, Mutzel W. " Pharmacokinetics of GdDTPA/dimeglumine after intravenous injection into healthy volunteers. ", *Physiol Chem Phys Med NMR.*, vol. 16, pp. 167-172, 1984.
- [49] Schabel MC, Morrell GR, Oh KY, Walczak CA, Barlow RB, Neumayer LA. " Pharmacokinetic mapping for lesion classification in dynamic breast MRI. ", *J Magn Reson Imaging.* , vol. 31(6), pp. 1371-1378, 2010.
- [50] Donaldson SB, West CML, Davidson SE, Carrington BM, et al. " A Comparison of Tracer Kinetic Models for T1-Weighted Dynamic Contrast-Enhanced MRI: Application in Carcinoma of the Cervix.", *Magnetic Resonance in Medicine.* , vol. 63, pp. 691-700, 2010.
- [51] Li X, Welch EB, Chakravarthy AB, Xu L, Arlinghaus LR, Farley J, Mayer IA, Kelley MC, Meszoely IM, Means-Powell J, Abramson VG, Grau AM, Gore JC, Yankeelov TE. " Statistical comparison of dynamic contrast-enhanced MRI pharmacokinetic models in human breast cancer.", *Magnetic Resonance in Medicine.* , vol. 68, pp. 261-271, 2012.
- [52] Larson KB, Markham J, Raichle ME. " Statistical comparison of dynamic contrast-enhanced MRI pharmacokinetic models in human breast cancer. Tracer kinetic models for measuring cerebral blood flow using externally detected radiotracers.", *J Cereb Blood Flow Metab.* , vol. 7, pp. 443-463, 1987.
- [53] Chen H, Li F, Zhao X, Yuan C, Rutt B and Kerwin WS. " Extended Graphical Model for Analysis of Dynamic Contrast-Enhanced MRI.", *Magnetic Resonance in Medicine* , vol. 66, pp. 868-878, 2011.
- [54] Song T et al. " Optimal k-space sampling for dynamic contrast-enhanced MRI with an application to MR renography.", *Magnetic Resonance in Medicine* , vol. 61(5), pp. 1242-1248, 2009.
- [55] Fram EK, Herfkens RJ, Johnson GA, Glover GH, Karis JP, Shimakawa A, Perkins TG, Pelc NJ. " Rapid calculation of T1 using variable flip angle gradient refocused imaging.", *Magn Reson Imaging.*, vol. 5, pp. 201-208, 1987.
- [56] Stanisz GJ, Henkelman RM. " Gd-DTPA relaxivity depends on macromolecular content.", *Magn Reson Med.*, vol. 44(5), pp. 665-7, 2000.

- [57] Orton MR, d'Arcy JA, Walker-Samuel S, Hawkes DJ, Atkinson D, Collins DJ, and Leach MO. "Computationally efficient vascular input function models for quantitative kinetic modelling using dce-mri", *Physics in Medicine and Biology.*, vol. 53(5), pp. 1225, 2008.
- [58] Rosset A, Spadola L and Ratib O "OsiriX: An Open-Source Software for Navigating in Multidimensional DICOM Images.", *J Digit Imaging.*, vol. 17(3), pp. 205-216, 2004.
- [59] Cheng M. "Cheng M. Investigation and Optimization of Parameters Accuracy in Dynamic Contrast-Enhanced MRI. Journal of Resonance Imaging.", *Journal of Resonance Imaging.*, vol. 28, pp. 736-743, 2008.
- [60] Koh TS, Zeman V, Darko J, Lee TY, Milosevic MF, Haider M, Warde P, Yeung IW. "The inclusion of capillary distribution in the adiabatic tissue homogeneity model of blood flow.", *Phys Med Biol.*, vol. 46(5), pp. 1519-38, 2001.
- [61] Cameron CA. "An R-squared measure of goodness of fit for some common nonlinear regression models ", *Journal of Econometrics*, vol. 77, pp. 1790-2, 1997.
- [62] Akaike H. "A new look at the statistical model identification. ", *IEEE Trans Auto Control.*, vol. 19, pp. 716-723, 1974.
- [63] Muzic RF Jr, Saidel GM. "Distributed versus compartment models for PET receptor studies.", *IEEE Trans Med Imaging.*, vol. 22, pp. 11-21, 2003.
- [64] Kuhl CK and Schild HH "Dynamic Image Interpretation of MRI of the Breast.", *J Magn Reson Imaging.*, vol. 12, pp. 965-974, 2000.
- [65] Gong Y, Brady M "Texture-Based Simultaneous Registration and Segmentation of Breast DCE-MRI.", *LNCS.*, vol. 5116, pp. 174-180, 2008.
- [66] Dempster A, Laird N, Rubin D "Maximum Likelihood from Incomplete Data via the EM algorithm.", *Journal of the Royal Statistical Society*, vol. 39, pp. 1-38, 1977.
- [67] Jackson A, O'Connor JPB, Parker GJM and Jayson GC "Imaging Tumor Vascular Heterogeneity and Angiogenesis using Dynamic

- Contrast-Enhanced Magnetic Resonance Imaging.”, *Clin Cancer Res*, vol. 13(12), pp. 3449-3459, 2007.
- [68] Leach MO, Brindle KM, Evelhoch JL et al. “ Assessment of antiangiogenic and antivascular therapeutics using MRI: recommendations for appropriate methodology for clinical trials.”, *The British Journal of Radiology*, vol. 13(12), pp. 3449-3459, 2007.
- [69] Schmid VJ, Witcher B, Padhani AR, Taylor NJ and Yang GZ “ Bayesian Methods for Pharmacokinetic Models in Dynamic Contrast-Enhanced Magnetic Resonance Imaging. ”, *IEEE Trans Med Imaging*, vol. 25(12), pp. 1627-1636, 2006.
- [70] Kelm BM, Menze BH, Nix O, Zechmann CM and Hamprecht FA “ Estimating Kinetic Parameter Maps From Dynamic Contrast-Enhanced MRI Using Spatial Prior Knowledge.”, *IEEE Trans Med Imaging* vol. 10(28), pp. 1627-1636, 2009.
- [71] Xiaohua C, Brady M, Lok-Chuen J, Moore N “ Simultaneous Segmentation and Registration of Contrast-Enhanced Breast MRI.”, *LNCS* vol. 3565, pp. 126-137, 2008.
- [72] Yankeelova TE, Lucia J, Lepagea M, Lib R, Debuskd L, Lind PC, Pricea R, Gorea JC “ Quantitative pharmacokinetic analysis of DCE-MRI data without an arterial input function: a reference region model.”, *Magnetic Resonance in Medicine* vol. 23, pp. 519-529, 2005.
- [73] Yang C, Karczmar GS, Medved M, Stadler WM “ Estimating the Arterial Input Function Using Two Reference Tissues in Dynamic Contrast Enhanced MRI Studies: Fundamental Concepts and Simulations.”, *Magnetic Resonance in Medicine*, vol. 52, pp. 1110-1117, 2004.
- [74] Ahearn TS, Staff RT, Redpath TW, Semple SIK “ The use of the Levenberg Marquardt curve-fitting algorithm in pharmacokinetic modelling of DCE MRI data.”, *Phys Med Biol* vol. 50, pp. 85-92, 2005.
- [75] Su MY, Cheung YC, Fruehauf JP, Yu H, Nalcioglu O, Mechetner E, Kyshtoobayeva A, Chen SC, Hsueh S, McLaren CE, Wan YL “ Correlation of Dynamic Contrast Enhancement MRI Parameters With Microvessel Density and VEGF for Assessment of Angiogenesis in Breast Cancer.”, *J Magn Reson Imaging*, vol. 18, pp. 467-477, 2003.

- [76] Chen et al. "Automatic identification and classification of characteristic kinetic.", *Med Phys.*, vol. 33(8), pp. 2878-2887, 2006.
- [77] Chen et al. "A fuzzy c-means (fcm) based approach for computerized segmentation of breast lesions in dynamic contrast enhanced mr images.", *Acad Radiol.*, vol. 13(1), pp. 63-72, 2006.
- [78] Cui et al. "Malignant lesion segmentation in contrast-enhanced breast mr images based on the marker-controlled watershed.", *Med. Phys.*, vol. 36, pp. 34359, 2009.
- [79] Fusco et al. "Selection of suspicious rois in breast dce mri.", *Lecture Notes in Computer Science*, vol. 6978, pp. 48-57, 2011.
- [80] Gibbs et al. "Textural analysis of contrast-enhanced mr images of the breast.", *Magn Reson Med*, vol. 50(1), pp. 92-98, 2003.
- [81] Hill et al. "Edge intensity normalization as a bias field correction during balloon snake segmentation of breast mri.", *Proc IEEE Eng Med Biol Soc*, pp. 3040-3043, 2008.
- [82] Lee et al. "Textural analysis of lesion perfusion volumes in dynamic contrast enhanced breast mri.", *2008 5th IEEE International Symposium on Biomedical Imaging From Nano to Macro*,
- [83] Lehman et al. "Mri evaluation of the contralateral breast in women with recently diagnosed breast cancer.", *The New England Journal of Medicine*, vol. 356, pp. 1295-1303, 2007.
- [84] Liney et al. "Breast lesion analysis of shape technique: semiautomated vs. manual morphological description.", *Journal of Magnetic Resonance Imaging*, vol. 23, pp. 493-498, 2006.
- [85] Mayerhoefer et al. "Are signal intensity and homogeneity useful parameters for distinguishing between benign and malignant soft tissue masses on mr images? objective evaluation by means of texture analysis.", *Magn Reson Imaging*, vol. 9(26), pp. 1316-1322, 2008.
- [86] Meinel et al. "Breast mri lesion classification: improved performance of human readers with a backpropagation neural network computer-aided diagnosis (cad) system.", *J Magn Reson Imaging*, vol. 25(1), pp. 89-95, 2007.

- [87] Olsen et al. " Screening for breast cancer with mammography", *Cochrane Database of Systematic Reviews*, pp. CD001877, 2001.
- [88] Schnall et al. " Diagnostic architectural and dynamic features at breast mr imaging: Multicenter study.", *Radiology*, vol. 238, pp. 42-53, 2006.
- [89] Szabo et al. " Dynamic mr imaging of the breast: Analysis of kinetic and morphologic diagnostic criteria", *Acta. Radiol.*, vol. 44, pp. 379-386, 2003.
- [90] Tanner et al. " Does registration improve the performance of a computer aided diagnosis system for dynamic contrast-enhanced mr mammography?", *2006 5th IEEE International Symposium on Biomedical Imaging From Nano to Macro*,
- [91] Tzacheva et al. " Breast cancer detection in gadolinium enhanced mr images by static region descriptors and neural networks.", *J Magn Reson Imaging*, vol. 17(3), pp. 337-42, 2003.
- [92] Zheng et al. " Step: spatiotemporal enhancement pattern for mr based breast tumor diagnosis.", *Med Phys.*, vol. 36(7), pp. 3192-3204, 2009.
- [93] Juntu et al. " Machine learning study of several classifiers trained with texture analysis features to differentiate benign from malignant soft-tissue tumors in t1 mri images.", *J Magn Reson Imaging*, vol. 31(3), pp. 680-689, 2010.
- [94] Mayerhoefer et al. " Are signal intensity and homogeneity useful parameters for distinguishing between benign and malignant soft tissue masses on mr images? objective evaluation by means of texture analysis.", *Magn Reson Imaging*, vol. 9(26), pp. 1316-1322, 2008.
- [95] K. Nie et al. " Quantitative analysis of lesion morphology and texture features for diagnostic prediction in breast MRI.", *Acad Radiol.*, vol. 15(12), pp. 1513-25, 2008.
- [96] A.Degenhard et al. " UK MRI Breast Screening Study. Comparison between radiological and artificial neural network diagnosis in clinical screening.", *Physiol Meas*, vol. 23(4), pp. 727-39, 2002.

- [97] P. Gibbs et al. "Textural analysis of contrast-enhanced MR images of the breast.", *Magn Reson Med.*, vol. 50(1), pp. 92-8, 2003.
- [98] T. Schlossbauer et al. "Classification of small contrast enhancing breast lesions in dynamic magnetic resonance imaging using a combination of morphological criteria and dynamic analysis based on unsupervised vector-quantization.", *Invest Radiol.*, vol. 43(1), pp. 56-64, 2008.
- [99] D. M. Ikeda et al. "Development, standardization, and testing of a lexicon for reporting contrast-enhanced breast magnetic resonance imaging. Journal of Magnetic Resonance Imaging.", *Invest Radiol.*, vol. 13, pp. 889-895, 2001.
- [100] C.E. McLaren et al. "Prediction of malignant breast lesions from MRI features: a comparison of artificial neural network and logistic regression techniques.", *Acad Radiol.*, vol. 16(7), pp. 842-51, 2009.
- [101] S.C. Agner , at al. "Textural kinetics: a novel dynamic contrast-enhanced (DCE)-MRI feature for breast lesion classification. ", *J Digit Imaging.*, vol. 24(3), pp. 446-63, 2011.
- [102] U. Wedegärtner et al. "Differentiation between benign and malignant findings on MR-mammography: usefulness of morphological criteria.", *Eur Radiol.*, vol. 11(9), pp. 1645-50, 2001.
- [103] M. De Santo et al. "Automatic Classification of Clustered Microcalcifications by a Multiple Expert System.", *Pattern Recognition.*, vol. 26, pp. 1467-1477, 2003.
- [104] F. Keyvanfard et al. "Specificity enhancement in classification of breast MRI lesion based on multi-classifier.", *Neural Computing and Applications.*, DOI: 10.1007/s00521-012-0937-y 2012.
- [105] Bates, D.M. and Watts, D.G. "Relative Curvature Measures of Non-linearity.", *J. Roy. Statistical Society. Series B Methodological*, vol. , pp. 1-25, 1980.
- [106] Galbraith, S.M. and Lodge, M.A. and Taylor, N.J. and Rustin, G.J.S. and Bentzen, S. and Stirling, J.J. and Padhani, A.R. "Reproducibility of dynamic contrast-enhanced MRI in human muscle and tumours: comparison of quantitative and semi-quantitative analysis", *NMR Biomed.*, vol. 15(2), pp. 132-142, 2002.

- [107] Schabel et al. " Pharmacokinetic mapping for lesion classification in dynamic breast MRI", *J Magn Reson Imaging*, vol. 31(6), pp. 1371-1378, 2010.
- [108] M Heisen and X Fan and J Buurman and N A W van Riel and G S Karczmar and B M ter Haar Romeny " The use of a reference tissue arterial input function with low-temporal-resolution DCE-MRI data", *Phys Med Biol*, vol. 55(16), pp. 4871-4883, 2010.
- [109] Matthew R Orton and James A d'Arcy and Simon Walker-Samuel and David J Hawkes and David Atkinson and David J Collins and Martin O Leach " Computationally efficient vascular input function models for quantitative kinetic modelling using DCE-MRI", *Phys Med Biol*, vol. 53(5), pp. 1225, 2008.
- [110] Dale, B.M. and Jesberger, J.A. and Lewin, J.S. and Hillenbrand, C.M. and Duerk, J.L. " Determining and Optimizing the Precision of Quantitative Measurements of Perfusion from Dynamic Contrast Enhanced MRI", *J Magn Reson Imaging*, vol. 18(5), pp. 575-584, 2003.
- [111] Henderson, E. and Rutt, B.K. and Lee,T.Y. " Temporal sampling requirements for the tracer kinetics modeling of breast disease", *Magn Reson Imaging*, vol. 26(2), pp. 1057-1073, 1998.
- [112] Richard G.P. Lopata and Walter H. Backes and Paul P.J. van den Bosch and Natal A.W. van Riel " On the identifiability of pharmacokinetic parameters in dynamic contrast-enhanced imaging.", *Magn Reson Imaging*, vol. 58, pp. 425-429, 2007.
- [113] Ilana C. Benjaminsen and Kjetil G. Brurberg and Else-Beate M. Ruud and Einar K. Rofstad " Assessment of extravascular extracellular space fraction in human melanoma xenografts by DCE-MRI and kinetic modeling.", *Magn Reson Imaging.*, vol. 26(2), pp. 160-70, 2008.
- [114] Fusco R, Sansone M, Maffei S, Petrillo.A. " Dynamic Contrast-Enhanced MRI in Breast Cancer: A Comparison between Distributed and Compartmental Tracer Kinetic Models.", *Journal of Biomedical Graphics and Computing, Journal of Biomedical Graphics and Computing.*, vol. 2(2), pp. 12-23, 2012.

- [115] Fusco R, Sansone M, Petrillo M, Antonella Petrillo. “ Influence of parameterization on tracer kinetic modeling in DCE-MRI.”, *Journal of Medical and Biological Engineering.*, Uncorrected Proof Available online 7 Sep 2012, doi: 10.5405/jmbe.1097.